Stockholm University
Department of Astronomy

LICENTIATE THESIS

Neutrino treatments and the impact on core-collapse supernova simulations

Author:
Aurore Betranhandy

Department of Astronomy,
The Oskar Klein Centre,
Stockholm University,
AlbaNova,
106 91 Stockholm,
Sweden

Supervisor:
Evan O'Connor

Co-Supervisor:
Stephan Rosswog

Month 03, 2021

Abstract

In this Licentiate I discuss the results obtained in our latest study (Betranhandy & O'Connor, 2020) that focuses on the impact of the treatment of neutrino pair processes on core-collapse supernova (CCSN) simulations as well as provide an introduction to the underlying physics. I will begin this thesis by recapping stellar evolution and the path leading to CCSNe. I will then talk about some of the key physics phenomena of stellar evolution that also play a role in CCSNe. Different kinds of supernovae ending the life of massive stars will then be described. We will briefly summarize CCSN physics and go through the state-of-the-art simulation results. As observations are as important as simulations, we will review some of the knowledge surrounding supernovae gathered through this channel.

Once we will have the necessary elements of understanding concerning CCSN simulations, we will focus on neutrino physics, including neutrino transport and neutrino interactions, and how it can be incorporated into simulations. This will be an introduction to our latest results in the included paper where we show the impact of neutrino interactions and transports physics in state-of-the-art, spherically symmetric, simulations of two modern core-collapse progenitors. Our major conclusion is that important properties of the explosion, like the explosion energy, can be sensitive to the transport method.

Abstrakt

I den här licentiatavhandlingen diskuterar jag resultaten från vår senaste studie (Betranhandy & O'Connor, 2020) som fokuserar på den inverkan behandlingen av processer hos neutrinopar har på simuleringar av kärnkollapssupernovor (CCSN) och ger en introduktion till den underliggande fysiken. Jag kommer att börja den här avhandlingen med att sammanfatta stjärnutveckling och vägen som leder till CCSN. Jag kommer sedan prata om några av de viktiga fysiska fenomen hos stjärnutveckling som också spelar en roll för CCSN. Olika sorters supernovor som avslutar livet hos massiva stjärnor beskrivs sedan. Vi kommer kortfattat summera CCSN-fysik och gå igenom de allra senaste simuleringarnas resultat. Eftersom observationer är lika viktiga som simuleringar kommer vi gå igenom en del av den kunskap kring supernovor som samlats genom denna kanal.

När vi väl har alla de nödvändiga grunderna för förståelse av CCSN-simuleringar kommer vi fokusera på neutrinofysik, samt neutrinotransport och neutrinointeraktioner, och hur de kan införlivas till simuleringar. Detta kommer att vara en introduktion till våra senaste resultat i den inkluderade artikeln där vi visar med toppmoderna simuleringar den inverkan neutrinointeraktioner och transportfysik har på två moderna sfäriskt symmetriska kärnkollapsföregångare. Vår huvudsakliga slutsats är att viktiga egenskaper hos explosionen, exempelvis explosionsenergin, kan vara känslig för transportmetoden.

Included paper

- Impact of neutrino pair-production rates in core-collapse supernovae, Phys. Rev. D 102, 123015, 2020, A. Betranhandy and E. P. O'Connor

My contribution

Nucleon-nucleon bremsstrahlung rate kernels (OPE from Hannestad & Raffelt (1998) and T-matrix from Guo & Martínez-Pinedo (2019)) were implemented in NuLib by the lead author. Simplified versions of pair-processes were already implemented in NuLib as well as the full kernel for electron-positron annihilation.

Nucleon-nucleon bremsstrahlung kernels were included in GR1D by the lead author. All simulations presented in the paper were performed by the lead author using GR1D and NuLib.

All the analysis development, figure generation, and a significant fraction of the writing of the manuscript was done by the lead author.

Contents

List of Figures

All non referenced figures have been created by the author (namely 1.1,1.3,2.4,2.1,2.6,2.7,2.9,2.10,3.1)

1

Introduction

Supernovae are some of the most fascinating cosmic objects. These explosions have been known for thousands of years (Green & Stephenson, 2003). Their name comes from Novae which means new, as the explosions appeared as new stars. The adjective "Super" comes from observations as some of these events had a luminosity significantly higher than traditional novae (Baade & Zwicky, 1934). While technically accurate from an observational point of view, we now know that this description and classification encompasses a wide range of different cosmic explosions (Da Silva, 1993). For example, one subtype of supernovae are Type Ia supernovae. These are thermonuclear supernovae, e.g. runaway thermonuclear explosions of white dwarfs. The remaining observational types of supernovae mainly represent core-collapse supernovae, which are the focus of this Licentiate thesis. As these phenomena are representing the end of the life of massive stars, we will now briefly describe the different stages of stellar evolution up to this point.

1.1   Overview of stellar evolution

At our starting point, we do not have any star. When a cloud of gas and dust, reaches the so-called Jeans mass limit, any kind of perturbations will trigger a collapse. Depending on the proto-star masses created through the collapse, different evolutionary paths appear (Kippenhahn et al., 2012; Maoz, 2017). Two main paths are represented in Fig. 1.1.
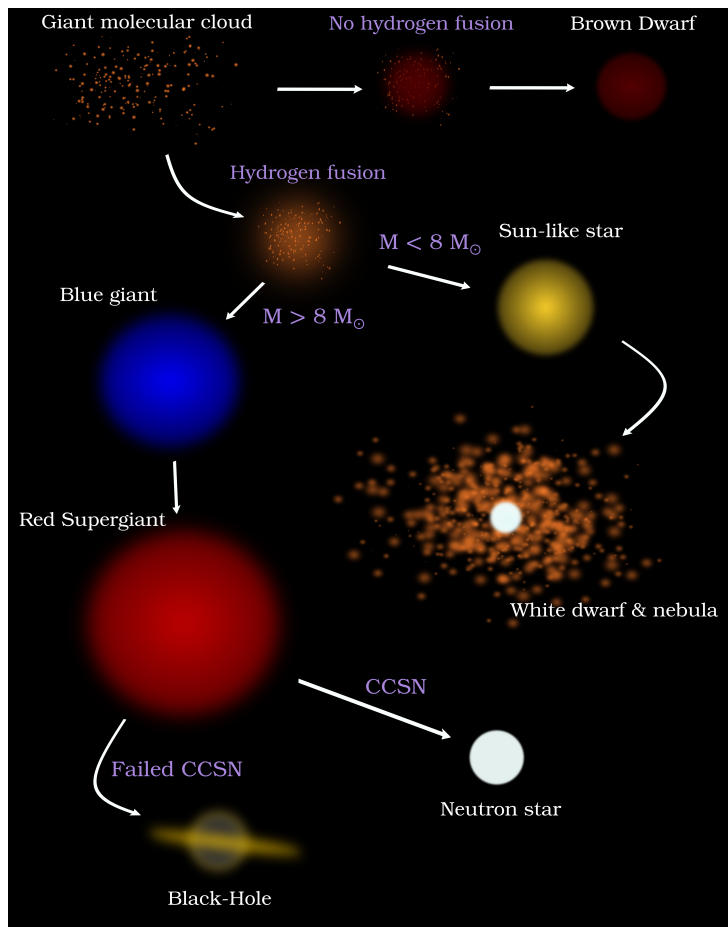
Figure 1.1: Diagram of stellar evolution channels originating from stellar formation in giant molecular clouds to various compact objects.

For the first path, upper part of Fig. 1.1, the resulting objects do not undergo hydrogen fusion and therefore a non (or sub) stellar object is formed. These objects have masses between 13 and 80 Jupiter masses (Burrows et al., 1997; Basri, 2000), resulting in a pressure in the core that is not sufficient to trigger hydrogen fusion. While these objects are interesting in the study of planet formation, we will not focus on them in the following as they do not relate to the subject of this thesis.
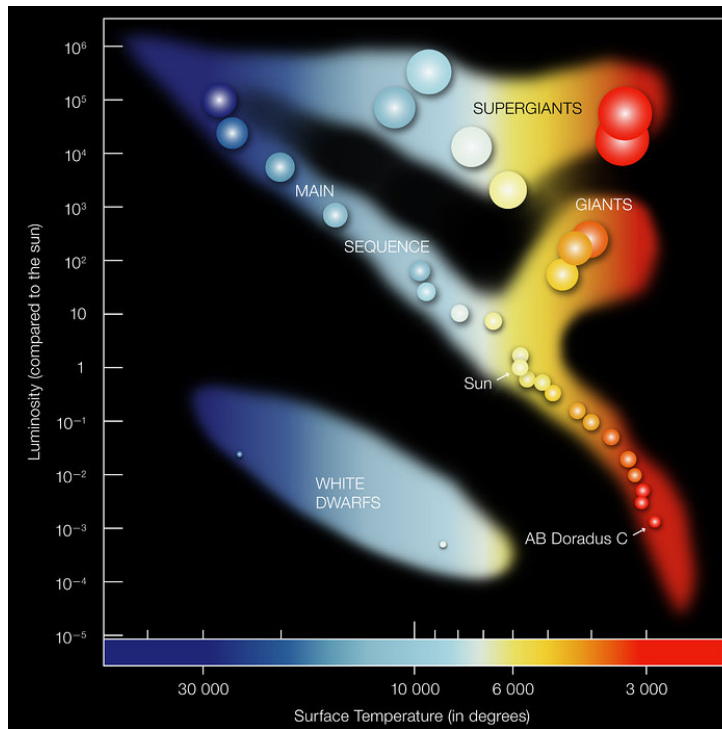
Figure 1.2: Hertzsprung-Russel diagram.
From ESO Australia (https://www.eso.org/public/images/eso0728c/)

The remaining evolution of these stars can be very briefly described as the following. The second path is defined by the ability of the proto-star to undergo hydrogen fusion. At this point, the star enters the main sequence branch on the Hertzsprung-Russel (HR) diagram shown in Fig. 1.2. As they evolve, stars will increase their radii and luminosities until leaving the main sequence branch (Kippenhahn et al., 2012; Maoz, 2017). The subsequent evolution will be separated in two channels depending on the star mass. In the case of solar-like stars with masses $M_* \lesssim 8\ M_\odot$, the star will stay on the main sequence for more than 50 million years, and significantly longer for lowest mass stars ($\sim$ 10 billion years for the sun). Once the reservoir of hydrogen is exhausted, the core contracts due to the lack of radiative pressure counteracting gravity. It will then leave the main sequence, entering the red giant branch. Once on the red giant branch, for stars with $M_* \gtrsim 0.8\ M_\odot$, fusion will eventually start again in the core, which will successively fuse elements up to oxygen and neon. At this point fusion stops as the density and temperature are not sufficient to trigger fusion. The core will then contract, increasing the density until the electron degeneracy pressure becomes relevant and halts the collapse. This degeneracy pressure arises due to electrons being fermions and therefore subject to the Pauli

exclusion principle (Heilbron, 1983). At that point, the remnant will be a first type of compact object, a white dwarf. The shells which were surrounding the core beforehand are slowly ejected by winds, creating a planetary nebula.

For stars with masses M_* 8 $M_\odot$ (Smartt, 2009), the core will exhaust its reservoir of hydrogen in the first tens of millions of years. Once all the hydrogen in core has been consumed, helium fusion in core will begin while hydrogen fusion will continue in a shell outside of the core. This will continue up to the creation of iron, at which point the fusion stop due to the iron nuclei being the most tightly bound. The core structure at this point can be idealized as seen Fig. 1.3.
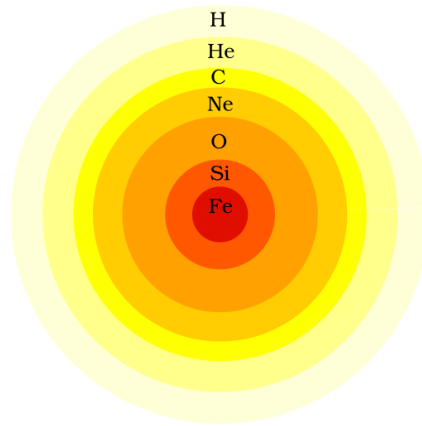
Figure 1.3: Idealized onion structure at the end of massive stars evolution.

Once fusion stops, energy generation stops and so does the radiative pressure coming from the core. This configuration can stay stable for a long time due to shell fusion, electron degeneracy, pressure and residual heat, but will ultimately fail to counterbalance gravity as the mass of the core grows, leading to a collapse of the star once the core surpasses the effective Chandrasekhar mass (Woosley et al., 2002). The core soon reaches nuclear density where nuclei disintegrate and neutrons and protons interact with each other (Bethe, 1990). Due to the strong force, the collapse stops. This channel is the one leading to CCSN supernovae and will be our main interest in this thesis.The collapse is halted in a sudden manner. This information propagates through the iron core and the still infalling matter. As the sound speed varies through the infalling matter, the information propagation speed will rapidly exceed the sound speed. This place is called sonic point and is when the shock forms. In many cases, this shock will end up disrupting the whole star and create the final CCSN. We will study this process in more detail in chapter 2.2.

In the case of failed supernovae, nothing is sufficient to indefinitely halt the collapse. The ac-

cretion of mass is too high and the core is too dense. This eventually leads to a gravitational field that is too strong to be balanced by any available pressure. This dramatic collapse will then lead to a black hole (O'Connor, 2017). While failed supernovae are thought to be more frequent for high mass stars (M_* 40 $M_\odot$), this channel is also possible in the case of less massive stars (Fernández et al., 2018).

These different possible scenarios explain the highly complex nature of stellar evolution. While this whole field is fascinating to study, we will now focus on one of the possible ends, core-collapse supernovae.

1.2   Why supernovae?

Now that we can place supernovae in the long story of stellar evolution, we can go a bit more in detail on the benefits of these explosions. Core-collapse supernovae have the role of ejecting the evolved stellar material into interstellar space (Thielemann, 2018). This ejected material helps in the creation of nebulae that will, later on, become new stars. These new stars will have a higher metallicity, which will impact their mass and evolution (Kippenhahn et al., 2012; Maoz, 2017). This is why core-collapse supernovae are cornerstones of nucleosynthesis.

On top of helping to distribute new elements through the interstellar medium, CCSNe are also the birth places of neutron stars and black-holes in the case of failed CCSNe. The neutron stars may go on to form neutron star-neutron star mergers. These are thought to be a main source of heavy elements nucleosynthesis (Thielemann et al., 2017), and therefore the physics of neutron star creation is also of importance in the bigger picture. Neutron stars also present conditions of matter impossible to reproduce on earth (Lattimer, 2012). Mergers and CCSNe then become essential laboratories for the physics of extreme matter.

CCSN physics is important to understand due to all the reasons stated above. In order to grasp this physics, researchers have been trying to simulate CCSNe for more than 50 years. The first computational models were created by Colgate & White (1966). A lot has been accomplished through the years and we are now able to consistently produce explosions in 3D simulaltions (Burrows et al., 2019; Mezzacappa et al., 2020; Kuroda et al., 2020; Glas et al., 2019b). However, as we are dealing with physics at the extremes, supernova models require some approximations.It is therefore therefore important to test different physics approximation while trying to attain the maximum precision possible with our available computational resources. These limited resources force us to approximate some physics and one of the goals of this Licentiate is to assess the importance of some of these approximations on the final ex-

plosion. This Licentiate, will try to give an insight into the supernova process and the physics involved. This should allow us to explain why CCSNe are so hard to model and the importance of some of my favourite particles, the neutrinos.

The next sections will discuss the different physics involved in core-collapse supernova progenitors as well as in the actual explosions.

2

Physics from stellar birth to stellar death

In order to give the reader a feeling of CCSNe complexity and why barely interacting particles such as neutrinos are important, this section will describe some of the physics involved. While fascinating, the precise details of most physics will not be covered here as this is not the scope of this Licentiate. This section will go through some of the different physics involved loosely following stellar evolution from main sequence to the explosion and beyond. However, most of the physical effects presented in the following stay true and relevant through all the phases.

2.1   Evolution up to core-collapse

This section will begin with a discussion of some of the physics involved in the stellar evolution through the main sequence. As the star is formed, it could be described as a giant ball of helium and hydrogen (Kippenhahn et al., 2012). The main question, especially in the case of massive stars, is "How do we come from this kind of simple structure to a complex mix of heavy elements ready to collapse?" as illustrated in Fig. 2.1. Which will be given an insight on through this chapter. This chapter will talk about the physics associated with photons, how they are created, and their role in the transport of energy. It will also discuss two other important areas, hydrodynamics and magnetic fields. These areas have predominant role not only in the main sequence evolution but also in the late stages, during the explosion.

An accurate understanding of stellar evolution is is important because CCSN simulations are heavily dependent on the progenitor. The evolution history of the progenitor as well as its structure, element distribution, and temperature is, therefore, crucial in CCSN simulations (Woosley et al., 2002).
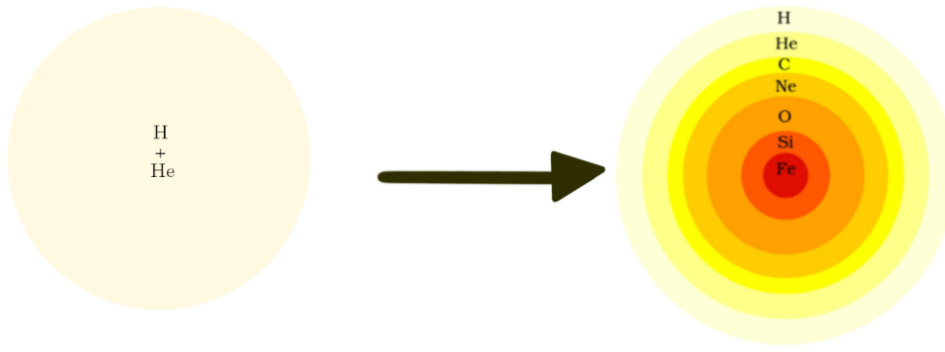
Figure 2.1: How to come from a giant ball of Hydrogen and Helium to an onion shell structure composed of increasingly heavier elements ?

An example of the differences that can arise between progenitors is represented Fig. 2.2. The mass of the star will determine the extent of the convective and radiative zones and therefore the structure, element mixing, and burning in the star. These zones will be determined by the temperature and composition gradients as well as by the energy production, but we will go more in-depth about this physics later on. Impacts of these differences on CCSNe has been raised by studies. For example, by showing the importance of progenitor turbulence on the final explosion (Kazeroni & Abdikamalov, 2019; Abdikamalov & Foglizzo, 2019; Müller et al., 2017; Müller & Janka, 2015).

2.1.1 Photons

Photons are essential for the transport of energy in the star. This radiative transport also creates a pressure which is one source for counteracting the collapse, allowing the star to exist. For these reasons, understanding the production and transport of these photons is a key piece to understand stellar evolution, the production of elements, and the distribution in the star.
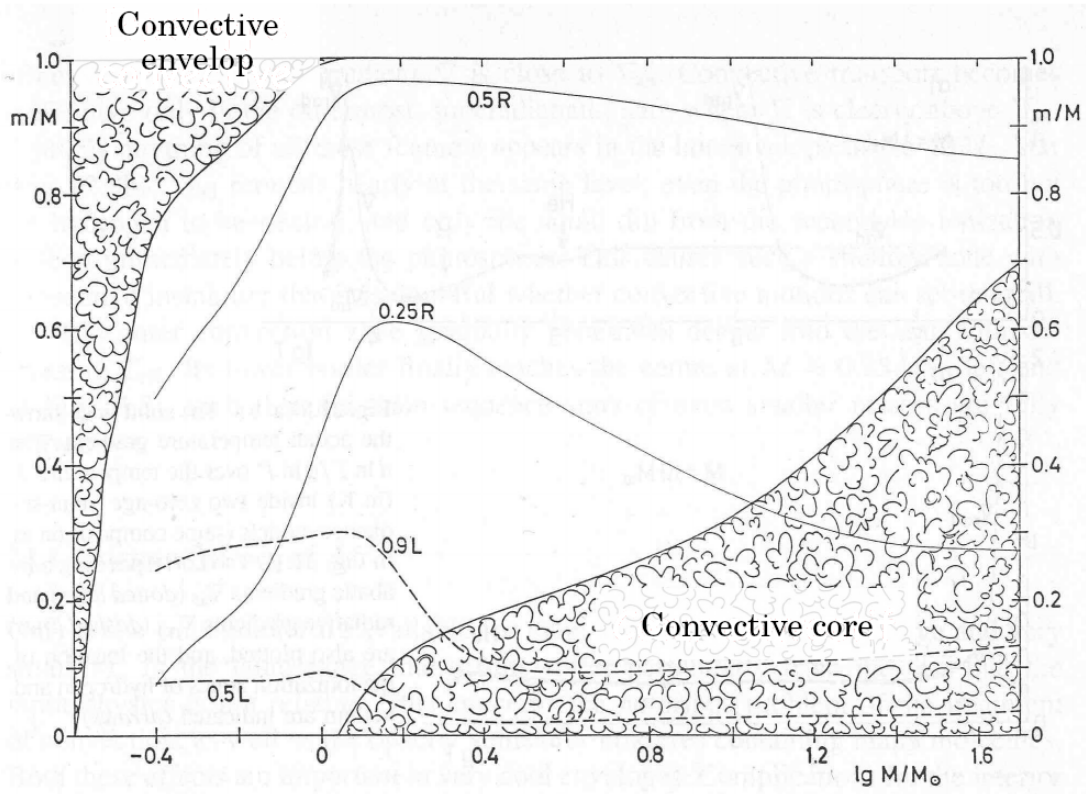
Figure 2.2: Convective zones by fraction of enclosed mass depending on the ZAMS mass of the star. The dashed lines represent the mass coordinate of 0.5L and 0.9L where L represents the total luminosity. The solid line represent the mass coordinate of 0.25R and 0.5R where R represents the total radius. From Kippenhahn et al. (2012)

2.1.1.1 Fusion

A star's life begins with the start of hydrogen fusion. Fusion will produce helium and release energy in the form of photons in the process. Once all the hydrogen has been consumed in the core, the fusion momentously stops, triggering a first core contraction. This increases the density and the temperature up to the fusion point of helium if the star is massive enough. While helium is burning in the core, hydrogen continues to burn in the outer shells.

This fusion-contraction-fusion process will continue to "climb up the element ladder" with the help of different fusion reactions, starting with proton-proton chain, carbon-nitrogen-oxygen cycle, and the triple-α process.

An interesting feature of this continuous process happens in lower mass stars. Sometimes, as one of the contraction phases occur, fusion does not start before degeneracy pressure can stabilize the star in the core. One of the characteristics of degenerate media is their inability to expand with temperature. As the volume can not increase to balance the temperature increase, the fusion process gets more energetic, increasing again the temperature. The whole process is called thermal runaway nuclear fusion. This phase is called X-flash through stellar evolution, X being the element undergoing fusion. This kind of runaway fusion is usually brief and soon the degeneracy breaks, allowing the core to expand again and the star continuing its classical evolution. The same process is proposed to be behind the creation of thermonuclear supernovae, where a white dwarf starts burning elements in a degenerate medium.One of the proposal for this is when the white dwarf accretes mass and overcomes the Chandrasekar mass (Maoz, 2017). It will then begin to collapse until the oxygen-neon core starts degenerate fusion. This runaway explosive burning will end up disrupting the whole star.

However, we are mainly interested in CCSNe progenitors, massive stars that end up with an iron core. As iron is the most stable element, it cannot undergo fusion. Leading to a disappearance of the main reservoir of energy, causing the radiative pressure to not be able to counteract gravity anymore. As mentioned before, this is when electron degeneracy pressure takes over, at least for a short while. Eventually, the iron core mass will be too high and the gravity will become to strong for the electron degeneracy pressure to stabilize the core against the collapse. The onset of core collapse is the beginning of the CCSNe process.

2.1.1.2 Transport

Radiative pressure is crucial for the stability of a star. As photons are created and transported through the matter, their interactions with said matter transfer a considerable amount of mo-

mentum to the medium and stabilize the star against gravity. These interactions will depend on the photon energy as well as the medium density and temperature, and can take two main forms. Photons absorption and emission through atom ionization and excitation, which will change the medium ionization, or elastic (Thompson) and inelastic (Compton) scattering.

In many cases, due to the high energy generation rate from fusion, radiative transport cannot diffuse photons in an efficient manner. Hydrodynamics will then take the lead on energy transport through convection. We will now talk about hydrodynamics and how convection triggers depending on the medium conditions.

2.1.2   Hydrodynamics

The second branch of physics discussed here is hydrodynamics, the physics of fluid movements. This is a vast and complex field, which is why the discussion will be constrained to some features interesting for stellar evolution and the CCSN dynamics. Hydrodynamic instabilities such as convection are fundamental to understand the global picture of stellar evolution, and more importantly here, the CCSNe evolution.

The first hydrodynamic process we will mention is convection. One of the main ways of transporting energy in a star through stellar evolution is based on this principle. The second type of processes we will mention are two of the main interface instabilities. They will break large scale structures, influence the magnetic field, transport energy between different scales, and later in stellar evolution, shape the explosion dynamics.

2.1.2.1   Convection

Convection helps the transport of energy by moving matter around, especially the hot medium close to the core. The formation of convection depends on a few parameters such as temperature, density, and global rotation. Eq. 2.1 represents the global Brunt-Väisälä frequency or buoyancy frequency (Pesnell, 1986) as N_T and N_μ added with the Rayleigh frequency N_Ω (Maeder, 2009; Spruit et al., 1983). If this N^2 is negative, it means an imaginary frequency for a fluid particle in a rotating medium being perturbed. An imaginary frequency means that a particle will not oscillate around its initial position but will definitely move out of equilibrium. This is when convection is triggered.

$$N^2 = N_T^2 + N_\mu^2 + N_\Omega^2 sin\theta \tag{2.1}$$

$$N_T^2 = \frac{g}{H_p}\delta(\nabla_{ad} - \nabla_T) \tag{2.2}$$

$$N_\mu^2 = \frac{g}{H_p}(\phi\nabla_\mu) \tag{2.3}$$

$$N_\omega^2 = \frac{1}{\omega}\frac{d(\Omega^2\omega^4)}{d\omega} \tag{2.4}$$

Eq. 2.1 shows different kind of factors, ν and $\kappa_{T/\mu}$ representing the fluid viscosity and thermal or chemical diffusivity respectively, g the gravity and H_p the pressure scale height (associated with mixing length theory), $\delta = -\left(\frac{\partial ln\rho}{\partial lnT}\right)$ the density stratification with respect to temperature for constant pressure and chemical composition and $\phi = \left(\frac{\partial ln\rho}{\partial ln\mu}\right)$ the density stratification with respect to chemical composition for constant temperature and pressure. Then we have the different variables $\nabla_T = \frac{dlnT}{dlnP}$, $\nabla_{ad} = \left(\frac{dlnT}{dlnP}\right)_{ad} = \frac{P\delta}{C_P\rho T}$ and $\nabla_\mu = \frac{dln\mu}{dlnP}$ representing the different gradients, temperature, adiabatic and chemical, respectively. The adiabatic gradient is the limit for which radiative transport will not be able to convey enough energy and convection will trigger in an adiabatic medium, it depends on pressure and density at constant entropy. For the oscillatory frequency associated with rotation N_Ω^2, ω represents the distance from the rotational axis, Ω the rotation and θ the angle from the rotational axis.

The different gradients and types of convection associated with each will now be briefly presented. The top panel of Fig. 2.3 represents the different types convection associated with the different gradients presented in Eq. 2.3 and Eq. 2.2 (e.g the Brunt-Väisälä frequency) in the case of a non rotating medium and was created by Rosenblum et al. (2011). The temperature gradient increases to the left and the three different rows represent each a kind of chemical gradient. The first row has a constant chemical composition, the middle row represents a medium unstable to convection due to the chemical composition gradient (negative chemical buoyancy frequency) and the bottom row represents a medium where the chemical composition stabilizes the system (positive chemical buoyancy frequency). The Schwarzschild criterion is represented by the limit $\nabla_T = \nabla_{ad}$, here the dotted line. To the left $\nabla_T > \nabla_{ad}$ (nominally unstable via the Schwarzschild criterion) while to the right $\nabla_T < \nabla_{ad}$ (stable accordingly to the Schwarzschild criterion). We will now link the global buoyancy frequency to this figure by going through every type of buoyancy frequency and explaining how it helps or not triggering some type of convection.

On the top row, the only possible source of instability is the temperature as the chemical gradient is zero and therefore the associated buoyancy frequency. Therefore, if we follow Eq. 2.2,

which represents the temperature buoyancy frequency, and knowing that δ is negative due to the temperature stratification in stars, we can see that this frequency is negative when the temperature gradient is superior to the adiabatic gradient as per the Schwarzschild criterion. This leads to overturning convection.

In the middle row, the chemical gradient tends to destabilize the medium, making convection easier to trigger. As seen in Eq. 2.3, the chemical buoyancy frequency does not contain a limiting gradient as for the temperature one, it simply depends on the different scales and the chemical stratification. The dashed line represents the Ledoux criterion, represented by $\nabla_T < \nabla_{ad} + \frac{\phi}{\delta}\nabla_\mu$ in the case of a stable system. Ledoux criterion is the limit for which overturning convection triggers in a medium influenced by chemical composition. As the temperature gradient evolves in the inverse way of the temperature, the medium becomes unstable to chemical composition but stable to temperature, leading to fingering convection triggering before the more global overturning convection.

In the bottom row, the chemical gradient tends to stabilize the medium, making convection harder to trigger. It creates conditions in which the medium can be stable even if the Schwarzschild criterion is satisfied. Overturning convection will then need a higher temperature gradient to trigger in order to fight the stabilizing chemical gradient. This leads to double-diffusive convection in the meantime.

Now, there is still a third criterion that has not been mentioned yet. It is global rotation and how it affects the triggering of convection. This is of importance during stellar evolution as most stars have a non-zero rotation, but also more specifically in the CCSN dynamics through the neutrino driven convection in a rotating system. The bottom panel of Fig. 2.3 shows the impact of the rotational frequency. As we can see following the rotational frequency axis, rotation tends to inhibit convection and globally stabilize the system. In a system without rotation or with a negative rotational frequency N_Ω^2, instabilities and convection will trigger for smaller temperature and chemical gradients. Adding rotation can also lead to different kinds of instabilities before the triggering of convection. Some of these instabilities and their importance will be discussed in the next section.

2.1.2.2   Instabilities

Instabilities can take a lot of different forms and globally tend to disrupt large scale structures. Convection is also a hydrodynamic instability, however, here we focus on other instabilities such as the Rayleigh-Taylor and the Kelvin-Helmholtz instabilities (Maeder, 2009). The choice of these two specific ones is linked not only to their predominance in fluid physics but also to their common appearance in CCSN simulations.
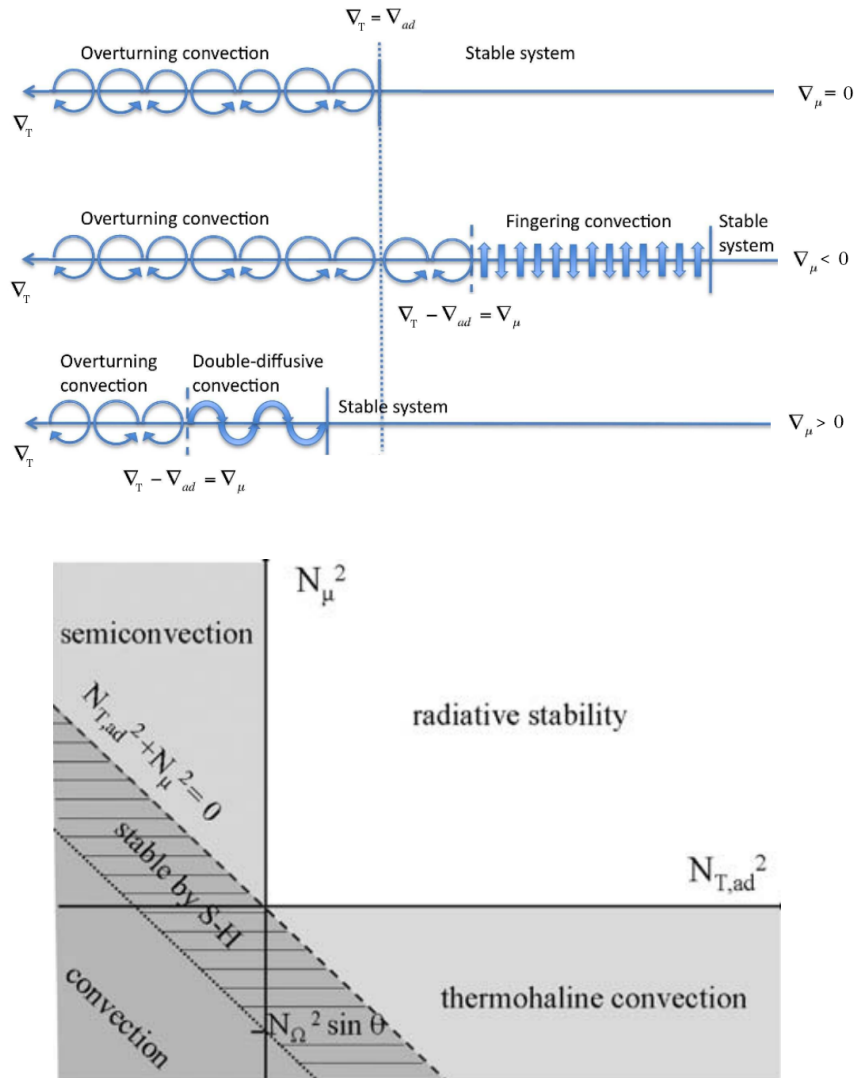
Figure 2.3: Top: Brunt-Väisälä frequencies and their impact on convection from Kippenhahn et al. (2012). Bottom: Different type of convections depending on the Brunt-Väisälä frequency from Maeder (2009)

.

Kelvin-Helmholtz instability is an instability creating wave-like structures. It will appear when two flows have different velocities while being connected. A small disturbance at the surface will grow exponentially, triggering an instability. In the same way, observed in ocean waves, the tail of the instability will turn into a vortex, increasing the global vorticity. This will not only tend to make interfaces of structures like inflows and outflows non-linear, but will also have an impact when considering magnetic fields.
A Rayleigh-Taylor instability represents the inversion of two parts of a stratified flow with each a different density. This inversion is linked to an unstable configuration where the less dense part is under a denser one. While this would contribute to convection in some cases, in this instability, the flow inversion is unstoppable and irreversible. While this inversion occurs, the medium can become highly chaotic, causing fluid elements to communicate with others while they would usually not. This has an importance in the frame of energy transfer and, as the Kelvin-Helmholtz instability, will also impact the magnetic field.

These instabilities will also play a role in the actual CCSN through the neutrino-driven mechanism which we will described in Sec. 2.2. In this mechanism, large scale hydrodynamic effects such as neutrino-driven convection and the standing accretion shock instability (SASI) and small scale hydrodynamic effects such as turbulence will play a role in conveying energy to the shock. As an example, the SASI might be disrupted by turbulence (Fogli et al., 2009).

2.1.3   Magnetic fields

As a star is composed of ionized hot gas, magnetic fields can not only exist but also influence the stellar evolution and its final explosion. In order to highlight this, we will first briefly discuss magneto-hydrodynamics (MHD) and its role in stellar evolution and CCSNe.

Plasma and magnetic fields interactions can be simplified to the two limiting cases: either the fluid drags the magnetic fluid with it (frozen-in flux situation) or the magnetic field dominates the fluid kinetics. This depends mainly on the magnetic field strength and the fluid density and velocity. This is why MHD, the physics of magnetized plasma as an ideal fluid, is a combination of the Navier-Stokes equations and the Maxwell-Faraday ones. MHD allows us to link magnetic and electric fields evolution to the usual hydrodynamic treatment. As for pure hydrodynamics, MHD has a different set of specific instabilities and can be impacted by global rotation.
Magnetic fields tend to adopt global structures in the form of dipole or sometimes higher order polarity. In Fig. 2.4 we show a diagram of a dipolar stellar magnetic field structure before collapse. The black lines represent the magnetic field lines, here in a poloidal configuration. While a magnetic field can have a more complex configuration, the dipolar structure is the one found most commonly.
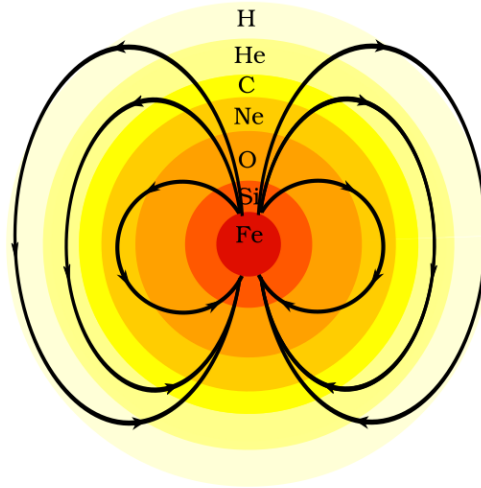
Figure 2.4: Diagram of the magnetic field in the progenitor

Some of the global MHD effects as well as some of the instabilities will now be discussed in order to explain how a magnetic field can grow enough to get out of the frozen-in flux phase and therefore impact the dynamics.

2.1.3.1 α-Ω effect

In Fig. 2.5, we show a diagram of one of the main global mechanisms, the $\alpha - \Omega$ effect (Schmitt, 1987). This effect is linked to the stellar rotation and is separated into the Ω effect and the α effect. We will describe these two parts and go on to describe the impact on the magnetic field. Imagining the star as a rotating dipole with a purely poloidal field, we will first encounter the Ω-effect. The field being frozen-in flux, the shear flow created by differential rotation will bend the poloidal field lines. This will continue until the appearance of an almost pure toroidal field. Once the toroidal field is installed, the α-effect will be triggered. The convection cells rising from the interior of the star have a tendency to rotate perpendicularly to the direction of the field. As for the Ω-effect, the field lines will follow the fluid and create magnetic loops which will end up reconnecting with each other, creating a poloidal field. The shape of the magnetic loops before reconnection gives its name to the process. As reconnection and field line twisting are part of this process, it will help to maintain and increase the magnetic field through a dynamo effect. This dynamo effect becomes important when we try to gauge a progenitor magnetic field
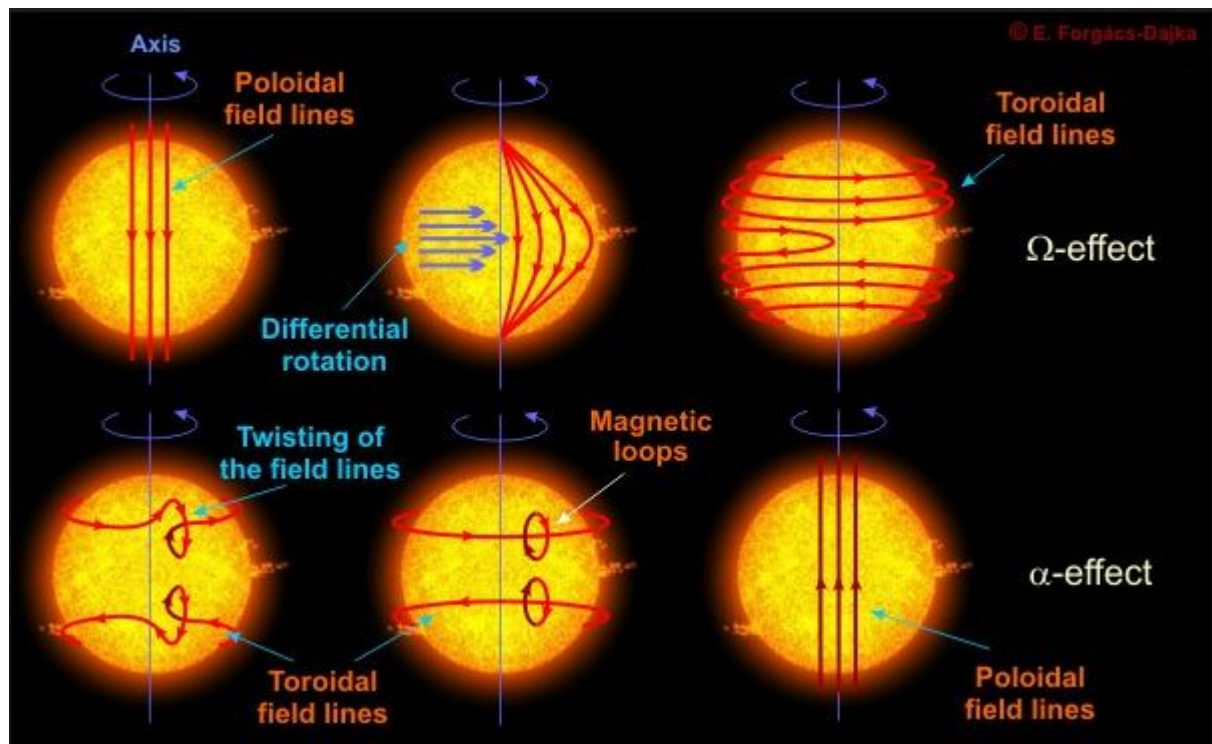
Figure 2.5: Diagram of alpha and omega effects. Artist : E.F. Dajka
(https://www.crediblehulk.org/wp-content/uploads/2017/01/alpha-and-omega.jpg)

strength. It is also an observable effect as it is thought to generate some stellar flares at the surface of the star.

2.1.3.2 MHD instabilities

MHD instabilities are different from purely hydrodynamic ones because of the magnetic field lines acting like springs between two fluid elements. In the previously mentioned Kelvin-Helmholtz instability, for example, a magnetic field parallel to the shear flows will have a tendency to counteract the instability development. It will also impact the development of convection, either helping it or stopping it depending on the magnetic field direction compared to the fluid. Now a discussion will be made about pure MHD instabilities and how they can impact the magnetic field.

Magneto-rotational instability (MRI) (Balbus & Hawley, 1998; Akiyama et al., 2003) is a kind of instability that develops in a rotating magnetized plasma. In the case of Keplerian rotation, two particles at the same distance from the center will rotate at the same speed. They will also be connected by a magnetic field line. Now if one of the particles was displaced either toward the center or outward, the Keplerian rotational speed of the two particles are different. But the magnetic field line will act like a spring, trying to force the particles to adopt the same velocity. For the outward, slower moving particle, this will cause it to accelerate forward which by momentum conservation will push the particle further away. The inverse will happen for the inward particle. The spring effect of the magnetic field line in this case creates an instability that would not have happened in a non-magnetized medium. As the MRI distorts the field lines, it will increase the global magnetic field, being a source of dynamo. This is important in the case of MHD-driven CCSNe for which the magnetic field needs to increase by several orders of magnitude when compared to stellar typical values (LeBlanc & Wilson, 1970).

In the case of MHD-driven CCSNe, another important magnetic effect occurs in the jet formation. The magnetic field at the pole will reconnect, creating a toroidal field moving outward, which help to transport matter as well as stabilizing the jets. However, as this field is toroidal, it will be prone to kink instabilities which might disrupt the jets if the magnetic field gets too strong (Obergaulinger et al., 2014; Kuroda et al., 2020; Mösta et al., 2014).

2.2 Core collapse and the supernova process

Now that we presented some of the physics involved in the evolution, we will talk about the actual collapse and subsequent supernova process. In order illustrate the outline, we use Fig. 2.6

which is an illustration of the following steps. Our star began with initial formation, continued through fusion of successively heavier elements, to end up with an iron core and an inability to resist gravity. We will now talk about the collapse process in different types of supernovae resulting from this. There are two main families of supernovae coming from progenitors with $M_* > 8M_\odot$, the pair-instability supernovae, for super-massive stars, and the CCSNe for stars with helium core masses up to ~64 $M_\odot$ (Woosley, 2017). This last family can be divided into three different kinds, failed CCSNe, MHD-driven CCSNe, and neutrino-driven CCSNe. We will now go more in detail about the collapse process and the different kinds of resulting explosions (or lack of). Following this overview of supernovae from massive stars, we will briefly review the state-of-the-art for several key physical components in CCSNe.
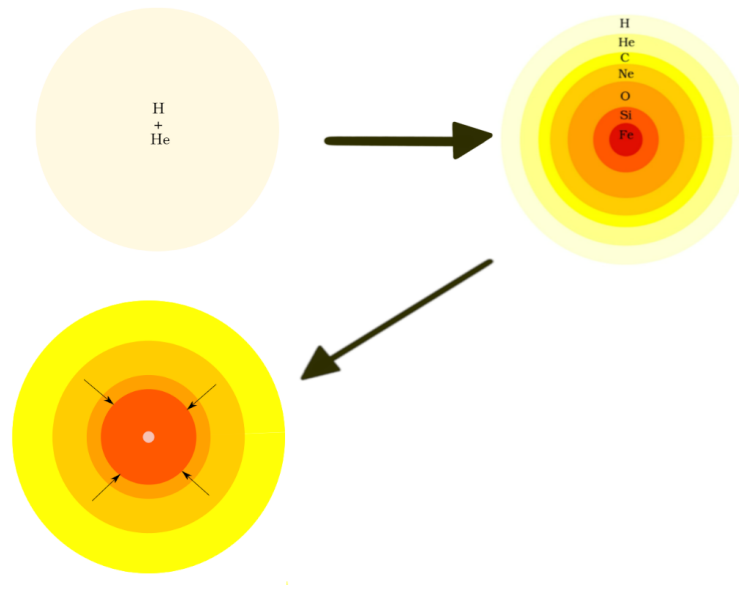
Figure 2.6: Diagram of stellar evolution up to the collapse of the core. The top left corner indicates the initial state of the star core when entering the main sequence. The top right corners follows with a representation of the star at the final stage. This is when the onion shell structure is visible with increasingly heavy element toward the core. The bottom left corner represents the onset of collapse (represented by the black arrows), once the gravity overcomes the pressure.

2.2.1 Overview of supernovae from massive stars

After discussing some of the physics involved in stellar evolution, it is time to explain how massive stars do end their lives. As mentioned above, supernova is a term encompassing a variety of fairly different events. This subsection will go more in detail about the non-thermonuclear su-

pernovae, e.g. the actual deaths of massive stars. Even if most massive stars die when the fusion stops and the core collapses, there is one category that does not go through this process called pair-instability supernovae. We will first talk about this category and go through CCSN categories beginning with failed supernovae, continuing with MHD driven supernovae, and ending up with neutrino driven supernovae.

2.2.1.1   Pair Instability Supernovae

Pair instability supernovae (PISN) are the outcome of the evolution of supermassive stars (helium core mass > 64 $M_\odot$). While the star goes through the last stages of its life, the density and temperature become high enough to trigger electron-positron pair production via photon pair production. This leads to a reduction of the radiative pressure (Fraley, 1968) in some parts of the star. The star will then start to collapse while it is still burning oxygen in the core. Increasing the density leads to an increase of oxygen burning and photon pair production, continuously reducing the radiative pressure and ultimately leading to a runaway explosion which will completely disrupt the star. This description is a simplification of the actual physics of this scenario and a lot of parameters actually influence the final outcome (Fryer et al., 2001; Bond et al., 1984).

In order to constrain the importance of different factors on the final explosion (rotation, metallicity), a few evolution codes have been created (Fryer et al., 2001; Woosley et al., 2002; Kasen et al., 2011; Stringfellow & Woosley, 1983; Ober et al., 1983; Woosley & Weaver, 1986; Umeda & Nomoto, 2002). They complement observations of this kind of supernova, as direct observations are rare. Indeed, supermassive progenitors cannot be created in our local universe due to a too high metallicity. The metallicity of giant molecular cloud is directly linked to the maximum mass of the stars it can create. A giant molecular cloud with a high metallicity will tend to collapse and split in parcels not massive enough to create supermassive stars due to the molecular density. This creates a low probability for PISN observations even if their high luminosities would classify them as superluminous (Kasen et al., 2011; Gal-Yam, 2012). This is why we need models. Fortunately, simulations of PISN are easier than ones of CCSNe as the explosion does not rely much on multi-D effects (Woosley, 2017) and can therefore be studied in 1D.

However, another consequence of the pair-instability process is to expel matter before the final collapse through pulsational pair instability (PPI). While these pulsational pair-instabilities do not destroy the star, they will affect the final explosion by enhancing the mass loss. PPI leads to a loss from ~ tenth of a solar mass for stars around 30 $M_\odot$ to tens of solar masses for stars with helium core as massive as 60 $M_\odot$ (see Woosley (2017) Table.1 for more precision). This can be observed through luminosity bursts associated with these ejections. PPI need to be included throughout the stellar evolution process and is, due to the timescales, more complex to simulate (Powell et al., 2021). Even if the complexity is high, the problem has still been studied exten-

sively (Woosley et al., 2002).

The reason behind the great interest in PISN is due to the many attempts to find an explanation for the aforementioned superluminous supernovae, as we are having a hard time explaining them with conventional supernova mechanisms. However, a study from Woosley (2017) came to the conclusion that pure thermonuclear processes can hardly explain the most extreme cases of superluminous supernovae. This is why we need to find other mechanisms. Other possible mechanisms for superluminous supernovae can include CCSNe, which we will now talk about.

2.2.1.2   Core-Collapse Supernovae

Now, we will focus on actual core-collapse supernovae. As mentioned in Chap. 1, when a star more massive than ~8 $M_\odot$ comes to the end of its life, fusion stops in the core, and collapse begins. This section will discuss about this collapse process as well as the different possible outcomes.

As silicon burns in a shell and the iron ashes add to the core, the density increases until the electron degeneracy pressure is overcome. At this point, density in the core is around ~10^9g cm^{-3}, and the collapse begins. The density will continue to dramatically increase until it reaches a level of ~10^{12}g cm^{-3}, the point at which the neutrinos become trapped. Neutrino trapping will ensure no loss of energy nor leptonic number, conserving the core global entropy and forcing the collapse to continue adiabatically. This will allow for a "smooth" collapse until obtaining a homogeneous medium of nucleon supported by the residual strong force. It will finally cause the equation-of-state (EOS) to stiffen, halting the collapse and forming the proto neutron star (PNS) in the core. Information about this halt will propagate through the infalling matter upon reaching a place where it becomes supersonic. This is when the supernova shock is created. This shock will then propagate out, dissociating nuclei and fighting against the ram pressure of infalling matter. It will cause a net loss of energy for the shock which will end up stalling at a radius between 100 and 200 km. We present a schematic view of this phase in Fig. 2.7, where the last panel represents the stalled shock.

How this shock is revived is one of the main questions of this Licentiate (and supernova theory in general). Our most up-to-date modern theory of CCSNe suggests it can follow three different paths: it can fail (failed CCSNe), be helped by the magnetic field (MHD-driven CCSNe), or by neutrinos (neutrino-driven CCSNe). We will now explore these three scenarios and later focus on the physics involved in the last one.
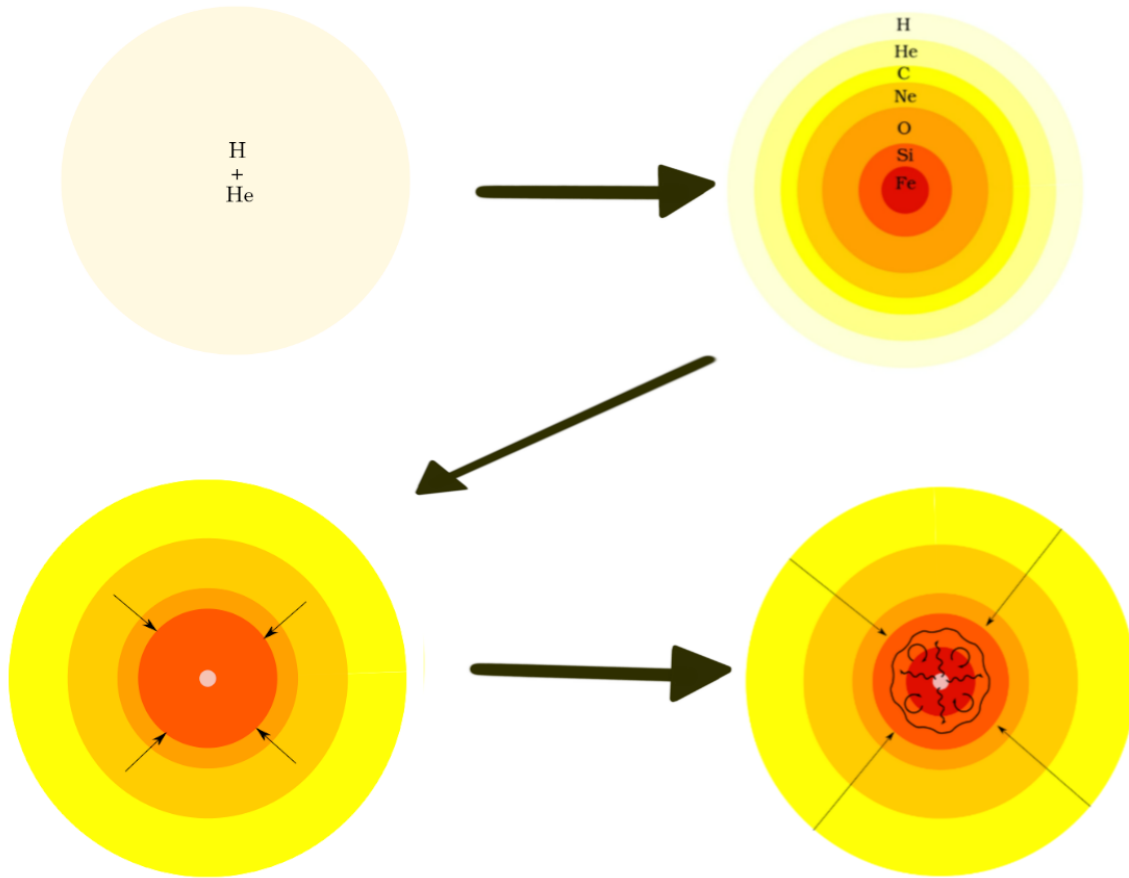
Figure 2.7: Diagram of stellar evolution and the steps leading to the shock revival phase. The top left corner indicates the initial state of the star core when entering the main sequence. The top right corners follows with a representation of the core at the final stage. This is when the onion shell structure is visible with increasingly heavy element toward the core. The bottom left corner represent the onset of collapse (represented by the black arrows), once the gravity overcome the pressure. The bottom right corner indicates the phase of shock revival. Once the shock has been launched, the dissociation of infalling matter and ram pressure will cause it to stall between 100km and 200km from the core. In order to produce the final explosion, this shock (indicated by the wavy black circle) needs to be revived by both hydrodynamical processes (indicated by the spirals) and heating by neutrinos diffusing from the PNS (indicated by the wavy arrows).

1. Failed Supernovae

Because reviving the stalled shock is far from being straightforward, a frequent outcome of early simulations was a failed supernova. The matter falling onto the core increases the density enough to overcome the nuclear force, collapsing the PNS into a stellar-mass black hole. Now, as we do manage to obtain explosions through simulations, failed supernovae are now more physical and can be used to explain observationally faint supernovae (Lovegrove et al., 2017). They also obviously explain the existence of stellar-mass black holes.

One of the many potential factors in the explodability of a star is its compactness. The term was defined 2011 by O'Connor & Ott (2011) and is essentially a representation of the stellar mass distribution defined by $\xi_M = \frac{M/M_*}{R(M)/(1000km)}$. For two stars, the one with the lower compactness has the mass coordinate M located at a larger radius. A common value of M is 2.5 $M_\odot$, representing the typical baryonic mass for black hole formation. This compactness is potentially linked to the ability of the star to explode, as a star with high compactness may be more likely to form a black hole before the shock revival (Ertl et al., 2016; Pejcha & Thompson, 2012).

Once the black hole has been created, the shock will be accreted as well as most of the remaining star. However, if some of the infalling material has a high enough angular momentum, it will be able to form an accretion disk surrounding the newly formed black hole. It may then give birth to a collapsar (Woosey 1993), objects often associated with long gamma-ray bursts (GRBs) even if their creation seems to remain unlikely (O'Connor, 2017; Dessart et al., 2012). An accretion disk forming later, from the very outer layers of the star may create long-lasting gamma-ray transients (Obergaulinger & Aloy, 2020).

Another way of obtaining electromagnetic signals from failed supernovae would be a core neutrino emission high enough to eject some parts of the outer layers without reviving the shock (Lovegrove & Woosley, 2013; Lovegrove et al., 2017).

Of course, electromagnetic counterparts are not the only messenger of a failed supernova. The rotation and densities involved are favorable for the emission of gravitational waves and neutrinos. Even if they could only be detected with a galactic supernova, numerous studies have been performed on the potential signal observed (Kharusi et al., 2020; Abdikamalov et al., 2020; Andresen et al., 2020; Kotake & Kuroda, 2017; Powell & Müller, 2018; Jones & Singleton, 2019; Müller et al., 2017).

2. MHD-driven Supernovae

MHD-driven supernovae are proposed to produce hypernovae and give birth to a magnetar (Obergaulinger & Aloy, 2020; Mösta et al., 2020, 2015; Obergaulinger et al., 2014, 2018). These environments have some of the strongest magnetic fields, around 10^{14-16} G. Such high magnetic fields result not only from the processes described Sec. 2.1.3 but also from the con-

traction of the core during collapse. Once the magnetic field in the PNS is strong enough, a jet structure will form along the rotation axis created first by the poloidal field and then sustained by toroidal fields along the jet. This toroidal field is created by an $\alpha - \Omega$ effect. These jets will form in the first milliseconds after bounce, sometimes even before the shock stalls. Expulsion of matter will then mainly occur along the poles, forming a strongly dipolar ejecta. Such ejecta will not undergo the same nucleosynthesis as the more classical supernovae due to having much faster expansion timescales. This is due to the jets taping directly into the magnetic energy of the core. From an observational point of view, we can obtain a long gamma-ray burst in some cases (Obergaulinger & Aloy, 2020) and the creation of hypernovae through this mechanism is an ongoing field of study (Kuroda et al., 2020). The remnant being strongly magnetized, the remnant will most often be a magnetar.

3. Neutrino-driven Supernovae

The neutrino-driven mechanism is the canonical method and a robust way for reviving the shock. As per their names, this category of supernovae will be revived through neutrinos interactions. Neutrinos will transport the energy from the cooling PNS to the shock, heating the post-shock medium and increasing the thermal pressure behind the shock. This method was theorized by Colgate & White (1966) as well as Bethe & Wilson (1985). While commonly accepted, it took years to be able to produce a 3D explosion based on this method. However in the last 5 years, tremendous progresses have been made and the community now manages to obtain regular explosions in 3D simulations including state-of-the-art neutrino transport, gravity treatment and magnetic fields (Vartanyan et al., 2018, 2019; Nagakura et al., 2019a; Murphy et al., 2019; Müller, 2016; Müller et al., 2018a,b; Glas et al., 2019b; Burrows et al., 2019; Radice et al., 2018; Powell & Müller, 2018; O'Connor & Couch, 2018; Cabezón et al., 2018).
The neutrino-driven mechanism will now briefly be described. Details on the physics involved will be discussed in Sec. 3. While the shock is stalled, the PNS is cooling via a continuous emission of neutrinos created mainly through electron and positron capture on protons and neutrons. The energy released by the PNS cooling will then be transferred to the post-shock matter, heating it and creating a thermal pressure behind the shock. Neutrinos are the main carrier of a gigantic reservoir of energy ($\sim 10^{53}$ erg). Even if only ~1% of them would be to interact with the matter behind the shock and deposit energy, we would obtain the classical value of $\sim 10^{51}$ergs (≈ 1 Bethe) for supernova explosions. It happens that the heating efficiency is close to 10% but its short duration also weights into the amount of transferred energy.

Figure 2.8 is a simulation snapshot describing the neutrino heating process in the core. We can see the shock as the outer boundary, the gain region in red with the neutrino driven convection appearing, the cooling part in blue and, the PNS in the center. The gain region is where
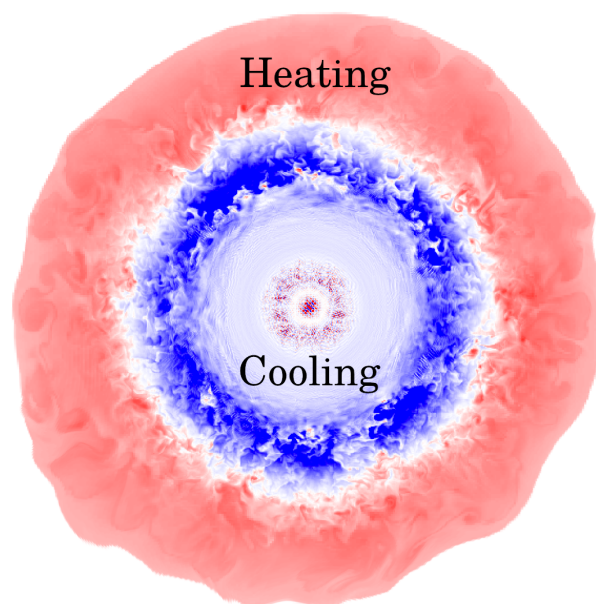
Figure 2.8: Snapshot from a simulation created for O'Connor & Couch (2018). The outer boundary represents the shock, the blue represented the parts where matter is loosing energy through neutrino loss and the red represents matter gaining energy through neutrino heating. The latter is commonly called the gain region. The infalling matter is not represented here.

the medium is dense and cold enough for the neutrinos to deposit more energy than the medium is radiating. This transferred energy is however not large enough to revive the shock by itself, which is why we rarely have explosions in 1D CCSN simulations.

Some hydrodynamic features not available in 1D simulations are necessary to aid in reviving the shock. While the shock is stalling, two hydrodynamic processes change the size of the gain region and help transport energy. First, as the matter gets heated, convection is triggered, increasing the energy transport from the PNS to the gain region. Second, the shock itself may acquire a global sloshing motion named the SASI (standing accretion shock instability). The SASI can take different forms from purely circular motion to vortex-like behaviour (Foglizzo et al., 2015; Kazeroni & Abdikamalov, 2019; Guilet et al., 2010). We will explore SASI, the neutrino emission, and the impact of the equation of state in the next subsection.

2.2.2 Equation of state

Neutron stars and proto-neutron stars feature states of matter impossible to reproduce on Earth. Therefore, they are fantastic laboratories for understanding nuclear physics through observations and simulations. However, this also makes them extremely difficult to model correctly. We need to extrapolate from known physics to infer the behavior of matter under such conditions.

The role of an equation of state (EOS) is to parametrize these extrapolations in order to predict condensed matter behaviour in our simulations. Even small changes in the EOS can change the supernova evolution (Schneider et al., 2019) at similar levels as the changes produced by neutrino transport and neutrino interactions. A lot of studies have been performed in the past decade to constrain the evolution dependence on EOS parameters (Schneider et al., 2019, 2020; Yasin et al., 2018; Steiner et al., 2013; Hempel et al., 2012). For example, it was shown in Schneider et al. (2020) that computing the gravitational mass of the PNS with constant entropy from the EOS may allow us to predict the time of black hole formation, as well as the black hole initial mass. This is helpful in gauging the necessary time for a simulation (Schneider et al., 2020), which becomes necessary in the case of 3D simulations. EOS also play a role in the emission of gravitational waves and neutrinos as they will determine the radius and mass of the PNS, therefore impacting the production of these messengers.

2.2.3 Gravity

As the star collapses, the density increases and so does the depth of the gravitational potential. Since the final outcome of CCSNe are compact objects (neutron star or black hole), it is evident

that an accurate treatment of gravity is necessary. Treatments of gravity in CCSNe vary depending on the simulation size and needs.

While a general-relativistic treatment of gravity would be the most accurate method, it can readily become computationally expensive. This computational cost is what makes it tricky to use in multidimensional simulations. In this case, we tend to use a modified version of Newtonian gravity, using an adapted gravitational potential. It approximates the effects of general relativity by using an effective relativistic gravitational potential ϕ_{eff} which mimics the deeper potential well of the GR case (Rampp & Janka, 2002). The underlying theory is to reproduce the solution of the TOV (Tolman-Oppenheimer-Volkoff) equations for hydrostatic equilibrium. We then replace the gravitational effective potential by the one satisfying these equations.

Unfortunately, this simple change cause some discrepancies. It especially tends to overestimate the relativistic effects (Liebendoerfer et al., 2005), leading to an increase of the infall velocity. In order to overcome this problem, several solutions have been considered. The most commonly used is called "case A" from Marek et al. (2006) and is easy to implement in most of Newtonian simulations. This method has been proven to give satisfactory results when compared to fully relativistic codes (Pan et al., 2018; Walk et al., 2019; O'Connor & Couch, 2018; Schneider et al., 2020) for supernova simulations. It however tends to underestimate black hole formation time in the case of failed supernovae.

Another importance of gravity in CCSN simulations appears when we try to predict the emission of gravitational waves (GW). GW are the fourth messenger giving us information about collapse physics in CCSNe after photons, cosmic rays and neutrinos. And the only one not being altered by the infalling matter or the circumstellar medium (neutrino oscillations due to outer shells modify the neutrino signal and matter is optically thick for photons). In the lucky event of a galactic supernova, detection of GW would be possible with the current technology, however, this would necessitate a very energetic CCSN.

For GW detection, we need to predict the waveform signal in order to extract information and correlate it with an actual event (Abdikamalov et al., 2020). As these signals are extremely sensitive to the explosion physics, we need 3D supernovae models with general relativity, good neutrino transport, and potentially, MHD. Unfortunately, a large number of these simulations are still not available through our current computational resources. This is important for disentangling the stochastic from the systematic effects but also in the scope of creating a matching algorithm for GW detectability. Some of the best candidates for GW detection are MHD-driven supernovae, usually involving rapid rotation, which strongly impacts the final GW waveform. A few recent papers present such types of MHD-driven CCSNe and their results on some rapidly rotating progenitors (Kuroda et al., 2020; Kuroda, 2020; Kotake et al., 2018).

2.2.4 Standing Accretion Shock Instability

The Standing Accretion Shock Instability (SASI) is the instability occurring in the shock while it is stalled (Blondin et al., 2003). While stalled, the shock can acquire a global motion which can either be oscillatory (m=0) (observed in 2D simulations) or spiral (m=±1,±2) (observed in 3D simulations) (Blondin & Mezzacappa, 2007; Hanke et al., 2013). This motion is a pure hydrodynamic instability that finds its source in an unstable advective-acoustic cycle between the PNS and the shock.

While the PNS is cooling, convection triggers the emission of acoustic waves. These waves propagate to the gain region behind the shock and trigger entropy and vorticity perturbations. These perturbations are advected with the fluid onto the PNS. When the flow reaches the neutrinosphere, it decelerates due to the neutrinos emission creating an outward pressure. This deceleration creates an adiabatic compression, increasing the temperature gradient as well as the perturbations. This denser, hotter zone reaching the PNS causes the emission of acoustic waves which in turn will travel to the shock. The new perturbations created have an amplitude greater than the initial ones. The growth rate is associated with the inverse of advection time. This is why the SASI growth is non-linear. It will however saturate when the shock oscillations are large enough to create their own disruption through Kelvin-Helmholtz and Rayleigh-Taylor instabilities (Guilet et al., 2010).

The SASI helps the revival of the shock by adding a turbulent pressure to the thermal pressure pushing the shock out, increasing the size of the gain region (Endeve et al., 2012).

The angular motion associated with the SASI is linked to the exponential growth of its oscillations, which, when reaching saturation, produce a rotation (Blondin & Mezzacappa, 2007; Kazeroni et al., 2016). This rotation can impact the spin of the final neutron star through the conservation of global angular momentum as well as the final neutron star's kick (Scheck et al., 2006).

SASI oscillations, on top of producing the aforementioned effects, also increase the local shock radius, increasing the gain region and the local energy deposition. These asymmetries will have an impact on the final explosion topography. Also, the spiral modes increase the advection onto the PNS by increasing accretion in specific locations when it reaches the PNS surface, which could be a reason for the appearance of lepton number emission, self-sustained asymmetry (LESA) (Walk et al., 2018; Glas et al., 2019b).

2.2.5 Neutrino physics

When the PNS forms, soon after the bounce, the matter is a hyper dense, hot mix of nucleons mainly composed of neutrons (Janka, 2017). In the final stages of collapse, up until bounce, neutrinos are trapped and therefore not able to cool the PNS effectively but nonetheless, they

play an important role in the evolution. Before bounce, the dominant cross-sections of neutrinos is proportional to approximately the square of their energy, resulting in high energy neutrinos being trapped. However, the downscattering on the residual free electrons allow some neutrinos to escape the core and change the equilibrium electron fraction. Once bounce happens, matter accreted onto the PNS soon after will rapidly dissociate and undergo electron capture which will lead to a neutrino burst once the shock becomes optically thin to neutrinos.

After that, neutrinos diffuse out of the core and also are emitted by electron and positron capture in the outer layer of the PNS. This will help in the PNS cooling and fix the evolution towards the future neutron star radius and mass by modifying its internal energy, reducing the thermal pressure. The temperature and radius evolution are therefore closely linked to the neutrino interactions and transport. The cooling rate also obviously influences the neutrino-driven explosion and shock revival. Neutrinos emitted while the PNS cools may transfer energy to the matter behind the shock. While technically true, the actual transfer is more complex and we will now try to briefly explain it. Neutrinos decouple from the matter at a place called neutrinosphere. The location of said neutrinosphere will also determine the average energy of the emitted neutrinos. The deeper the neutrinosphere is, the hotter the medium emitting neutrinos is and therefore the more energetic, on average, the emitted neutrinos will be.

These neutrinos will travel out to the gain region. The name of this region comes from the fact that its boundary is determined by the point at which the matter will gain more energy from neutrino interactions than it will emit (see Fig.2.8). This gain region is mainly made of free nucleons and alpha particles coming from the nuclei dissociation happening through the shock. Most of the neutrino interactions happening will be charged-current weak interactions due to the electron neutrinos and anti-neutrinos. Some energy of these neutrinos will be transferred to the fluid either through inelastic scattering or absorption. This energy deposition increases the matter temperature, increasing the thermal pressure behind the shock.

Some of the parameters modifying the energy deposition will be the size of the gain region (influenced by the SASI and turbulence), the neutrino luminosity (linked to the PNS, size, cooling rate, and accretion rate), and the heating efficiency itself (impacted by the weak interactions and their definitions).

2.2.6 Simulations

While CCSN physics is complex and therefore hard to model, advancements in computer science as well as relentless efforts from different groups in the last 50 years have given us a variety of simulation codes capable of modelling some of the most important processes in CCSNe. In the last three years, many groups have managed to obtain explosions in 3D in a quasi systematic manner (Kuroda, 2020; Kuroda et al., 2020; Nagakura et al., 2019c; Vartanyan et al., 2019; Glas

et al., 2019b; Burrows & Vartanyan, 2020; Burrows et al., 2019; Powell & Müller, 2018; Müller et al., 2018a; Vartanyan et al., 2018; Cabezón et al., 2018; Müller, 2016; Stockinger et al., 2020; Melson et al., 2015; Obergaulinger & Aloy, 2020; Melson et al., 2020; Reichert et al., 2020; Bollig et al., 2020). These explosions can either be neutrino-driven or MHD-driven, depending on the scope of the study.

However, a lot of open questions are still standing about CCSNe physics. For reference, we refer to four recent reviews: Mezzacappa et al. (2020) which describe the current state of neutrino transport and neutrino interactions in our simulations, Burrows & Vartanyan (2020) which gives an overview of the current understanding of CCSNe physics and emissions, Müller & Varma (2020) which describes the role of magnetic fields in neutrino-driven CCSNe simulations and Müller (2019) presenting the current stance on neutrino signal emitted from CCSNe and their help in understanding the underlying physics.

While it appears that we can now produce systematic explosions in 3D, it does not mean that we have understood everything about the underlying physics. Some of the pending questions are about the nucleosynthesis and the difficulties to reproduce observed values. For example, Sawada & Suwa (2020) explored the possibility for neutrino winds to create the observed 0.07 $M_\odot$ of Ni^{56} inferred from observations of SN1987A. They conclude on an increase in the Ni^{56} mass from the neutrino winds but still fail to reach the expected values.

Another question is about the variability of explosion energy while evolving a same progenitor. Stockinger et al. (2020) explored in detail the explosion of several low mass progenitors when compared with ECSNe and classical CCSNe. When using a widely studied progenitor of 9.6 $M_\odot$, they found explosion energies varying from 50% to 120% when compared with previous studies. While some differences could be linked to the neutrino transport, 120% difference between results from Vertex-Prometheus and Coconut-FMT (Müller, 2019), one using M1 transport and the other a fast multigroup method. Other differences observed when comparing results from Vertex-Prometheus and Fornax (Burrows et al., 2019; Radice et al., 2017) cannot come from the neutrino transport and are still not fully understood by the authors. We also studied this progenitor in our latest study (Betranhandy & O'Connor, 2020), with a resulting explosion energy varying depending on the neutrino pair processes treatment in 1D explosions. We performed these simulations using GR1D and a M1 scheme, varying only the pair processes transport and formalism. This shows how sensitive this progenitor can be to various parameters such as the neutrino physics but also potentially the resolution, gravity treatment, and number of dimensions.

Focusing just on neutrinos, a diversity of questions have been raised in the last 5 years.

The provenance of LESA and its impact on CCSN evolution is still unclear and will need further studies (Glas et al., 2018; Nagakura et al., 2019b; Fujimoto & Nagakura, 2019). Another neutrino related question is the topic of neutrino oscillations. Their probability of occurence in the CCSN context as well as their understanding and especially the way of including them in our simulations is a field of constant researches and has not yet been concluded on (Wolfenstein, 1978; Tamborra et al., 2017; Glas et al., 2019a; Padilla-Gay et al., 2020; Martin et al., 2019; Zaizen et al., 2019; Capozzi et al., 2018, 2017; Saez et al., 2018b,a; Duan et al., 2010; Fogli et al., 2009).
The accurate microphysics linked to neutrino interactions is also an open field of research. The interaction of neutrinos with heavy leptons, for example, muons, are still rarely included in simulations (Bollig et al., 2017, 2020; Guo et al., 2020) as well as the microphysics in super dense environment, where the state-of-the-art interactions can not be tested experimentally and therefore purely theoretical (Fischer et al., 2020; Betranhandy & O'Connor, 2020; Guo & Martínez-Pinedo, 2019; Kato et al., 2020; Müller, 2019). Neutrino interactions can also be modified by external factors such as magnetic fields (Duan & Qian, 2004, 2005; Lai & Qian, 1998), the potential impact being investigated in studies only recently (Kuroda, 2020).

MHD-driven CCSNe and the impact of magnetic fields on neutrino driven supernovae is also still an ongoing field of research. In order to produce a MHD-driven supernovae, initial magnetic fields must be increased to a threshold difficult to motivate based on stellar evolution (Takahashi & Langer, 2020). We usually impose an ad-hoc magnetic field to the progenitor (Obergaulinger et al., 2014; Mösta et al., 2014; Kotake et al., 2004; Kuroda et al., 2020; Obergaulinger et al., 2018; Obergaulinger & Aloy, 2020). Nevertheless stellar evolution models are pushing toward an understanding of the late stages magnetic fields (Takahashi & Langer, 2020). On top of the question of magnetic field strength, lies the question of its topography (Bugli et al., 2019), its effect on neutrino-driven supernovae (Matsumoto et al., 2020; Müller & Varma, 2020) and the following impact on nucleosynthesis (Reichert et al., 2020).

To conclude, while a lot has been done on understanding CCSN physics, it is still an open field and will be until we manage to accurately predict explosions, black hole formation, and reproduce observable results.

2.3   Late stages of supernovae - Supernova remnants

We will now mention the "late" stages of CCSNe and some of the reasons why an accurate physics treatment is so important. Supernovae are one of the main astrophysical sites for nucleosynthesis, creating and dispersing new elements and impacting the metallicity of their global surroundings. Supernovae are thought as being one of the main sites of heavy element creation,
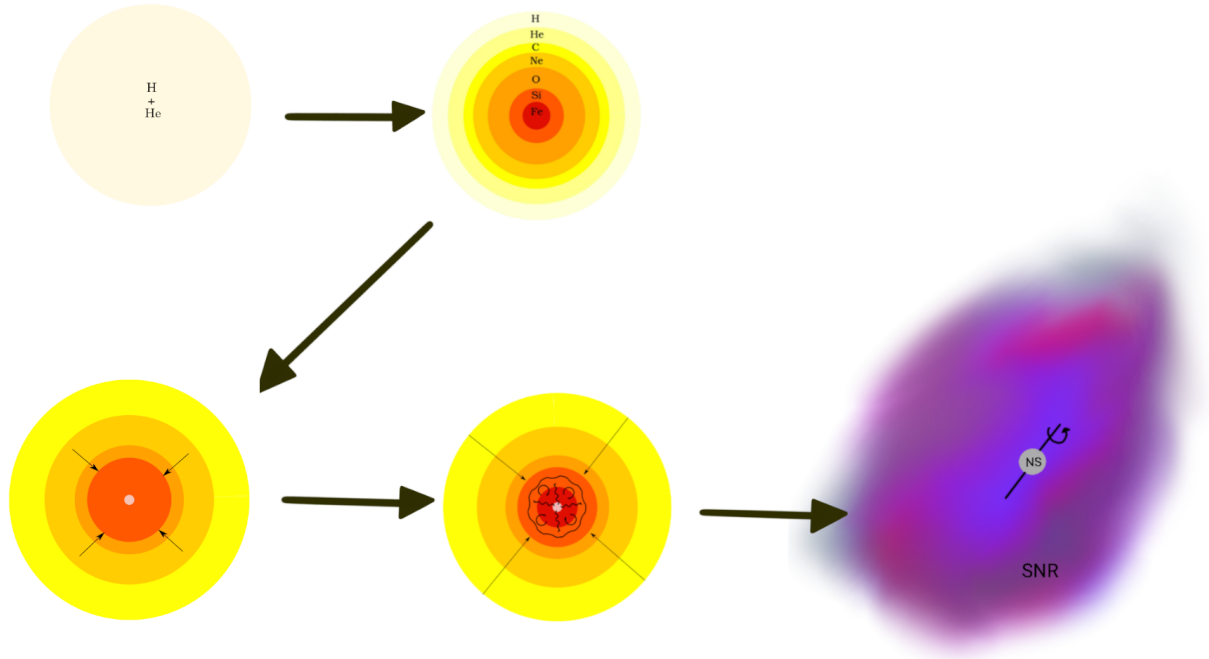
Figure 2.9: Diagrom of CCSN processes leading to the final stage of SNR and pulsar.

in the short time-frame after big bang when neutron star mergers could not exist (Davies et al., 1994). In Fig. 2.9, we present a schematic view of all the phases of stellar evolution, ending up with the supernova remnant and neutron star.

2.3.1 Nucleosynthesis and late stages emission

What we consider "late" stages in simulations is what starts happening a few minutes to hours after the actual collapse when the shock has been revived and is going through the outer shells and reaches the surface, the so-called 'shock breakout phase'. At this point, the supernova luminosity is mainly related to the energy of the shock and the structure of the star. The luminosity will now also be linked to the thermal emission of the shock heated star and the decay of ^{56}Ni, created through nuclear static equilibrium (NSE) while the shock goes through the matter, into ^{56}Co and then ^{56}Fe. The explosive conditions in the core also produce other iron-group elements. In the case of MHD-driven supernovae, this could be a favorable place for neutron capture processes, allowing very heavy elements such as uranium to be produced (Thielemann, 2018).

These late stages of CCSNe are the main ones studied observationally. We do not have access to the earlier stages through photon emission due to the optically thick matter between us and the collapse. However, these late observations help us decipher how our codes perform when modelling the explosion. One main prediction from our codes are the explosion energies, which generally define different categories such as faint supernovae (perhaps failed; Fryer et al. 2009), hypernovae (perhaps MHD-driven; Obergaulinger & Aloy 2020), or classical supernovae (perhaps neutrino-driven). It is one of the reasons why it is important for modellers to be aware of the observational side of our field.

Fortunately, while the probability of a galactic supernovae is low, extragalactic supernovae happen often. For example, the Zwicky Transient Facility (ZTF) detects ∼800 core-collapse supernovae per year through this photon emission (Bruch et al., 2020). These large surveys gather more statistics on the supernova population and help us improve our theories.

The name "late" stage emission might be a bit misleading as seen from outside but as we mainly focus on the collapse of the core and shock revival that happen in a few seconds at most, lightcurves from supernovae evolving through days and months are quite late for our timescale. The observational side of supernova science is empirical and therefore supernovae are classified depending on their observational features such as the existence or not of some spectral lines. The main observational categories can be seen in Fig. 2.10

Most Type II supernovae are thought to be neutrino-driven CCSNe, however, Type Ib/c BL peculiar supernovae are more often associated with MHD-driven supernovae due to their high luminosities, large velocities, and association with GRBs. Unfortunately, this classification does not give much information on the central engine and explosion process. Most of the observational features are linked either to the shock interaction with the circumstellar medium which itself depends on the stellar life history and, as massive stars are often found in binaries, the life evolution of its companion.

However, some specific supernovae, such as SN1987A, have been extremely useful to give us boundaries on the explosion energy and the nucleosynthesis thanks to its proximity to us. It helps us to calibrate some more parametrized codes such as the Hot-Bubble code (Scheck et al., 2006; Ugliano et al., 2012) and to use them to create statistical samples used in global studies such as the diffuse supernovae background (Kresse et al., 2020).

2.3.2 Supernova remnants and Pulsars

Supernovae are not only visible during their explosions, their impact on the interstellar medium (ISM) can be seen for thousands of years after in structures called supernova remnants (SNRs). SNRs are interesting to probe the interaction of the shock with the ISM and therefore the ISM structure. This is a useful guide through stellar evolution especially in the case of binaries. As
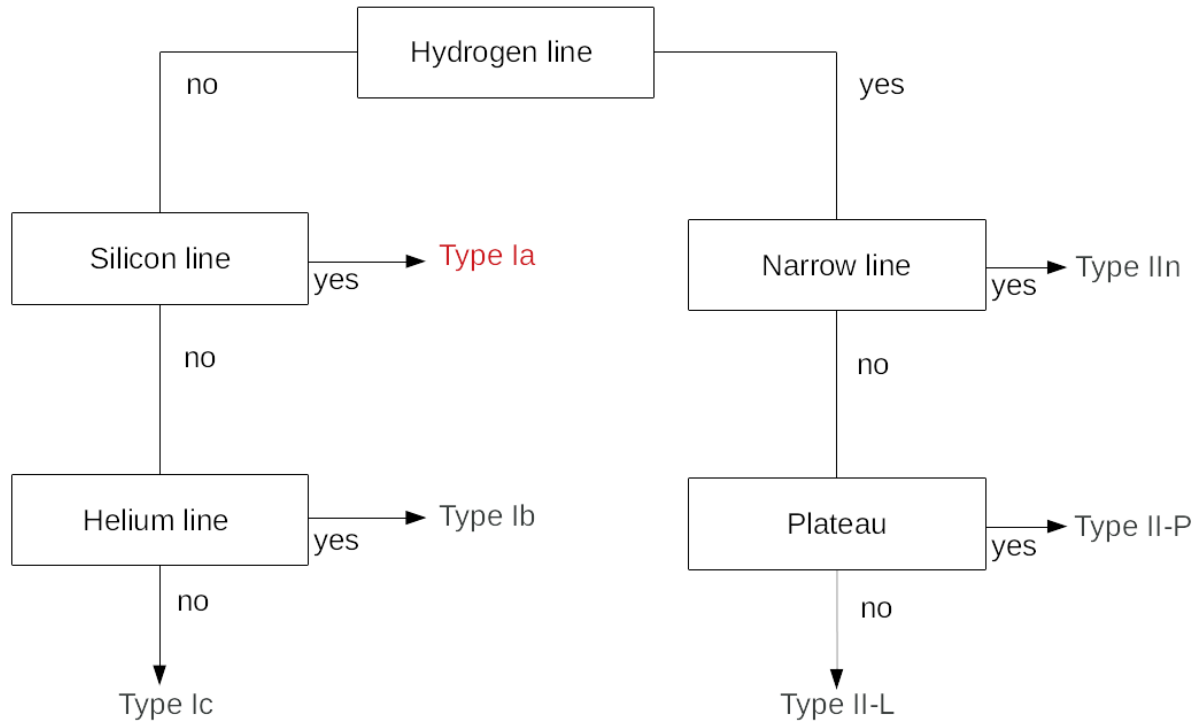
Figure 2.10: Flow chart of the main observational types of supernovae. All types apart from Type Ia are linked to CCSNe. Type Ia being thermonuclear supernovae.

Figure 2.11: Composite image of the center of the Crab nebula containing the crab pulsar. Composition from optical data from Hubble and X-ray data from Chandra. Ref optical: NASA/HST/ASU/J. Hester et al. ref X-Ray: NASA/CXC/ASU/J. Hester et al. (`https://www.nasa.gov/multimedia/imagegallery/image_feature_618.html`)

SNRs evolve slowly once formed, they give us indications on the precursor stellar explosions. On top of that SNRs are often sources of highly energetic electromagnetic emissions (x-rays and gamma-rays), both through the shocked medium emission and the internal pulsar. Pulsars when detected in SNR give us precious information on the initial neutron star kick and therefore help constrain the explosion energy as well as its possible morphology.

A well-studied object is the crab pulsar and the associated SNR coming from SN 1054 as seen in Fig. 2.11. We know the distance of this pulsar as well as its proper motion (Kaplan et al., 2008). That gives us precious information about the asymmetry in the initial explosion as well as on the potential kick velocity we would need to attain to create such a pulsar (Stockinger et al., 2020). On top of that, the global structure of the SNR as seen Fig. 2.12 helps us infer the explosion morphology.
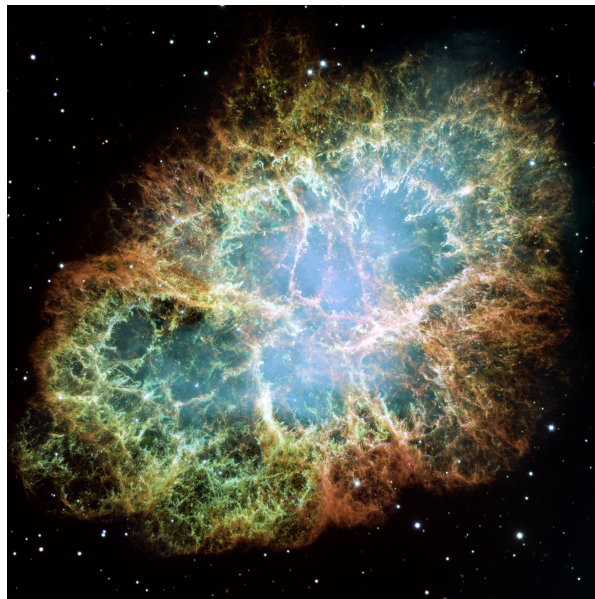
Figure 2.12: Mosaic image of the Crab SNR from Hubble. ref: NASA, ESA, J. Hester and A. Loll (Arizona State University)

3

Neutrino physics

As neutrinos are critical in CCSNe physics, their incorporation into our simulations must be handled carefully. This incorporation will depend on two main considerations: the way we model neutrino transport and how we treat their interactions with matter. Different studies have shown that both of these must be treated accurately, for a recent review, see Mezzacappa et al. (2020). For the transport, the optimal way would be to treat neutrinos transport using the Boltzmann equation. This would be computationally expensive and we need to find ways to work around this problem. We will go more in details about this in Section 3.1.

The second part, interactions with matter, is also complicated not only due to its cost but also due to some missing pieces in our knowledge of said interactions. Neutrinos are hard to study in Earth laboratories and even this would not automatically give us all the necessary information as the CCSNe medium involves temperatures and densities impossible to reproduce on Earth. Section 3.2 will be a discussion on these interactions and the different ways to treat them in simulations.

3.1   Neutrino transport

Treating each neutrino separately would be impossible, we therefore need to treat them in a similar way to photons. This is done through the Boltzmann equation which describes exactly the behavior of neutrinos through matter. The difficulty is that solving a 7D equation at each timestep and in every grid cell of a simulation is computationally prohibitive. We try to work around this problem by using approximate schemes, which we will describe in the following subsections.

But first, we need to understand how the neutrino distribution evolves. In order to do that,

we will have a look at the Boltzmann equation as it can be used not only to describe photon radiation, it can also be used to describe quite accurately neutrino behaviour in the limit of massless neutrinos.

$$\frac{df}{dt} = \sum \vec{F}$$

$$\frac{\partial f}{\partial t} + \frac{\partial f}{\partial \vec{x}}\frac{d\vec{x}}{dt} + \frac{\partial f}{\partial \vec{p}}\frac{d\vec{p}}{dt} = \sum \vec{F} \tag{3.1}$$

$$p^\alpha \left(\frac{\partial f}{\partial x^\alpha}\right) + \dot{p}^\alpha \left(\frac{\partial f}{\partial p^\alpha}\right) = c\left(\frac{\partial f}{\partial l}\right)_{coll} \tag{3.2}$$

Eq. 3.1 represents a simplified version of the Boltzmann equation for particles. $\vec{p}$ being the momentum and $\vec{F}$ the external forces acting on the particle distribution. Using a covariant generalization (Mihalas & Mihalas, 1984) and a line element defined by $p^\alpha = c\frac{dx^\alpha}{dl}$ instead of the proper time, we obtain Eq.3.2 describing the photon Boltzmann equation. Considering a three dimensional space, treating the full Boltzmann equation in our simulations would result in one dimension for the time, three for the position and three for the momentum. On top of the obvious complexity of computing many derivatives, computing the full source terms for all these dimensions, due to their complexity, dependences and the presence of integrals, is something if not infeasible, quite difficult and resource consuming. These are the reasons why we almost never solve the full Boltzmann equation.

Instead, we use ways of describing neutrino transport which are most effective on a computational level. Neutrino transport schemes can be classified in three main families. The first one considers only two states for the neutrinos, trapped or free streaming, and is named a "leakage scheme". Neutrino leakage is by far the most computationally inexpensive scheme but is also quite rudimentary, even with the consideration of different energies for the neutrino and usually gives flawed results in the case of CCSNe (Pan et al., 2018).
The second method is to treat neutrinos in the same way we would treat a fluid. This is when we come to the moment schemes. Created by Lindquist (1966), revisited by Thorne (1981), it allows us to treat both photons and neutrinos. In our paper Betranhandy & O'Connor (2020), we mainly use the most recent method coming from Shibata et al. (2011). Different sub-types of this scheme are the flux-limited diffusion and the 2-moment schemes. The latter being divided into two different categories, one using an analytic closure and one a variable Eddington tensor. The third family is a treatment of the full Boltzmann equation which, even if extremely expensive, has been used in several simulations (Sumiyoshi et al., 2014; Sumiyoshi & Yamada, 2012). We will begin with a brief description of the leakage scheme before focusing on the

moment schemes. We will then mention studies using a full Boltzmann treatment and how they help us constrain the limitations of other schemes.

3.1.1   Leakage schemes

Leakage schemes can be described as an interpolation between the neutrino free streaming and neutrino trapped regimes. An estimate of the neutrino emission in the free streaming limit (X^{loc}) is based on the local emissivity of the matter, whereas an estimate of the neutrino emission in the optically thick regime (X^{diff}) is based on a diffusion approximation. In practice, we take an interpolation of these two rates given in Eq. 3.3.

$$X^{eff} = X^{loc} \left(1 + \frac{X^{loc}}{X^{diff}} \right)^{-1} \tag{3.3}$$

Leakage schemes provide an estimate for both the number emission and the energy emission via this interpolation, both of these quantities represented in Eq. 3.3 via X. In order to determine X^{diff} quantities, it is necessary to know the mean optical depth for the neutrinos, which is a non-local quantity. Furthermore, both X^{diff} and X^{loc} depend on properties of the neutrinos like the neutrino degeneracy (η), which is a priori unknown. η is therefore interpolated between the free streaming region (where $\eta = 0$) and the trapped region. Unfortunately, this interpolation necessitates the mean optical depth value, which leads us to the following: in order to calculate both quantities, we need an iterative scheme beginning from an assumed initial value and continuing until convergence is reached. Nevertheless, as the neutrino quantities are usually not computed every time-step, this leakage scheme ends up being quite cheap when coming to computational performances (O'Connor & Ott, 2010; Ruffert et al., 1995; Rosswog & Liebendoerfer, 2003; Sekiguchi, 2010). However, this scheme finds its limitation in an inability to precisely determine the neutrino emission and properly model neutrino scattering which is an important factor in CCSN evolution.

3.1.2   Moment schemes

While leakage schemes are computationally cheap, they are not really an actual transport since neutrinos are not per se transported around the domain. A more realistic way of transporting neutrinos can be to use similar kinds of transport schemes to the ones used for photons (Lindquist, 1966). This category is the one encompassing moment schemes, which are divided into two main families.
The flux-limited diffusion, evolving only the zeroth moment and considering the first moment as a function of the zeroth, and the 2-moment schemes, evolving the two first moments and

approximating the higher moments by either an analytic closure (M1) or a variable Eddington tensor method. The underlying theory behind moment schemes is to first consider the radiation intensity and search for a way of reducing its dimensions.

The radiation intensity $I(\vec{x}, t, \mu, \nu, \phi) = 4\pi\nu^3\ f(\vec{x}, t, \mu, \nu, \phi)$ depends on the spatial dimensions $\vec{x}$, the time t, the angles of propagation μ and ϕ and the neutrino energy ν through the neutrino distribution f. One of the dimensions we can possibly remove here is the angle of propagation by expanding the intensity in moments independent of the angles. These moments are described in Eq. 3.4 with $d\Omega$ the angle integrand and l^α a 4-vector orthogonal to the fluid velocity used to simplify the notation. The greek indexes represent the time and 3 space-coordinates while the latin indexes represent only the spatial coordinates.

$$J = 4\pi\nu^3 \int f d\Omega$$

$$H^\alpha = 4\pi\nu^3 \int f l^\alpha d\Omega$$

$$K^{\alpha\beta} = 4\pi\nu^3 \int f l^\alpha l^\beta d\Omega$$

$$(3.4)$$

J is the zeroth moment and can be intuitively understood as the neutrino energy density. H^α is the first moment and can be understood as the neutrino flux while $K^{\alpha\beta}$ is the second moment and is the neutrino pressure tensor. Looking at it from a hydrodynamics perspective, we have access to different methods to solve this system of equations. Using the conservation equations for neutrinos, we can create a similar system to the one used in the hydrodynamics part of the code. From that, moment schemes can be divided into two sub-types, one being a flux-limited diffusion and the other a M1 scheme which itself can be based on either an analytic closure or an evolving Eddington factor for closing the system of equations.

3.1.2.1   Flux limited diffusion

Flux limited diffusion is a moment scheme introduced by LeBlanc & Wilson (1970) which uses the zeroth and first angular moments of the radiation intensity. In order to approximate the flux in both the diffusion and the free streaming regime, the flux is calculated as a limited diffusion equation.

$$F = \frac{c\lambda}{3} X \frac{dE}{dr} \qquad (3.5)$$

This will take a form presented in Eq. 3.5 with λ being the mean free path and X the flux-limiter. This limiter can be of different shapes and is chosen depending on the type of calculations needed. X is used to forbid simulations from creating a flux that could deplete the local distribution or transport the neutrinos on the grid at a speed larger than the speed of light. Several studies utilize this method in state of the art codes (Bruenn, 1985; Janka, 1992; Fryer, 2006; Burrows et al., 2006; Swesty & Myra, 2009; Yakunin et al., 2010; Zhang et al., 2013; Rahman et al., 2019; Bruenn et al., 2018).

3.1.2.2   2-moment

2-moment schemes are based on the idea of treating photons and neutrinos as a fluid and solving the equations in a similar way as fluid hydrodynamics. Which allows us to consider neutrinos as a distribution. 2-moment schemes evolve the zeroth and first angular moments of the neutrino distribution while prescribing higher moments to close the equations system (O'Connor, 2015; Obergaulinger et al., 2014).

Coming from the moment tensor $M^{\alpha\beta}$ Eq. 3.6, we can use its evolution equation Eq. 3.8 to derive the evolution equations for J and H^α.

$$M^{\alpha\beta} = Ju^\alpha u^\beta + H^\alpha u^\beta + K^{\alpha\beta} \tag{3.6}$$

$$M^{\alpha\beta} = En^\alpha n^\beta + F^\alpha n^\beta + P^{\alpha\beta} \tag{3.7}$$

$$\partial_\beta M^{\alpha\beta} - \frac{\partial}{\partial\nu}(\nu M^{\alpha\beta\gamma}\partial_\gamma u_\beta) = S^\alpha \tag{3.8}$$

We can either resolve this system in the rest frame of the fluid (using $J, H^\alpha, K^{\alpha\beta}$) or in the laboratory frame (using $E, F^\alpha, P^{\alpha\beta}$). In these equations, u^α represents the 4-velocity in the laboratory frame and n^α the 4-velocity in the fluid frame. In the following, we chose to focus on the laboratory frame. In this frame, the three first angular moments are E, F^α and $P^{\alpha\beta}$ (neutrino energy, momentum, and pressure as seen from the laboratory frame). We then take the evolution equation of the moment tensor $M^{\alpha\beta}$ (Eq. 3.6) to derive the evolution equations of the two first moments.

Using the formalism from Shibata et al. (2011), we obtain equation Eq. 3.9 (considering a flat space for simplicity which gives $\gamma = \det(\gamma_{ij}) = 1$ with γ_{ij} the spatial metric). In this equation, α represents the lapse, β the shift, n^α the 4-velocity, ϕ the gravitational potential, Σ the shear force tensor, a the acceleration, and S^α the source term.

$$\partial_t(E) + \partial_j(\alpha F^j - \beta^j E) + \frac{\partial}{\partial \nu}(\nu \alpha n_\alpha((F^\gamma n^\alpha + P^{\alpha\gamma})a_\gamma + P^{\beta\gamma}n^\alpha\Sigma_{\beta\gamma})) = \alpha(P^{ij}K_{ij} - F^j\delta_j\frac{\phi}{c^2} - S^\alpha n_\alpha)$$
(3.9)

$$\partial_t(E) + \partial_j(\alpha F^j - \beta^j E) + \frac{\partial}{\partial \nu}(\nu n_\alpha(R^\alpha + O^\alpha)) = \alpha(G + C)$$
(3.10)

$R^\alpha = (F^\gamma n^\alpha + P^{\alpha\gamma})a_\gamma$: impact of gravitational redshift

$O^\alpha = P^{\beta\gamma}n^\alpha\Sigma_{\beta\gamma}$: impact from observer motion

$G = P^{ij}K_{ij} - F^j\partial_j\frac{\phi}{c^2}$: source term from geometric interactions

$C = -S^\alpha n_\alpha$: source term from matter interactions

Using the simplification described above, we can reduce Eq. 3.9 to Eq. 3.10 for the energy density evolution. In the same way, we find Eq. 3.11 for the flux evolution with β the shift factor.

$$\partial_t F_i + \partial_j(\alpha P_i^j - \beta^j F_i) - \partial_\nu(\nu \alpha \gamma_{i\alpha}(R^\alpha + O^\alpha)) = -E\partial_i\alpha + F_k\partial_i\beta^k + \frac{\alpha}{2}P^{jk}\delta_i\gamma_{jk} + \alpha S^\alpha\gamma_{i\alpha} \quad (3.11)$$

As we can see, knowing that the source terms depend on the first three angular moments, we have 2 equations for (in 1D) at least 3 unknown variables. Which leads to an un-solvable system of equations. Fortunately, this system can be closed by so-called closure relations defining the second and higher moments. We will now talk about the two different forms of closure used in the literature.

3.1.2.3 Analytic closure

Analytic closures are based on local physics to extrapolate a 2nd moment based on the two first ones. For example, Shibata et al. (2011) propose three different kinds of analytic closures based on the optically thick, optically thin, and a grey zone interpolated between these regimes. They also state the criteria allowing to select between the different closures based on the characteristic speed to determine which closure would give physical results (i.e: no faster than light). One of the most common closures and the one used in GR1D was formulated by Minerbo (1978) and is based on a local maximization of entropy. Several other analytical closures and their resulting effects on simulations are defined in Pons et al. (2000); Obergaulinger et al. (2014); Kuroda et al. (2012); Just et al. (2015); Murchikova et al. (2017)

3.1.2.4 Variable Eddington tensor

The variable Eddington tensor formalism is a type of closure used in 2-moment schemes. It closes the system of equations through an estimation of higher moments based on the zeroth moment as well as the full neutrino distribution acquired via some other means (e.g. a simplified Boltzmann solution) as seen Eq. 3.12 and Eq. 3.13. In contrast with the previous method, the higher order moments are approximated through the full neutrino distribution instead of an analytical closure. This allows for a closed system of equations (Rampp & Janka, 2002; Buras et al., 2006).

$$K^{ij} = k^{ij}J \;\; ; \;\; k^{ij} = \frac{\int l^i l^j f d\Omega}{\int f d\Omega} \approx \frac{\tilde{K}}{\tilde{J}} \tag{3.12}$$

$$L^{ijk} = l^{ijk}J \;\; ; \;\; l^{ijk} = \frac{\int l^i l^j l^k f d\Omega}{\int f d\Omega} \approx \frac{\tilde{L}}{\tilde{J}} \tag{3.13}$$

$$\tag{3.14}$$

3.1.3 Boltzmann scheme

The full Boltzmann equation is sometimes used in simulation codes. While slow, it allows for highly accurate transport which helps us to test other transport schemes. It has been used in several simulation codes throughout the years.
For 1D codes, this method has first been used in 1993 and is still used today (Mezzacappa & Bruenn, 1993c,a,b,c; Yamada, 1997; Liebendorfer et al., 2004; Sumiyoshi et al., 2005). In 2D, the codes using this scheme are already less numerous as the computational cost does not increase only through a higher number of zones but also via an increasing number of dimensions in the equation itself (Livne et al., 2004; Brandt et al., 2011). In 3D, only one code makes use of the full Boltzmann treatment, following these papers: (Sumiyoshi & Yamada, 2012; Sumiyoshi et al., 2014).

All these schemes have advantages as well as limitations. Either their computational costs

make them hard to use, or their limitations cost us some of the important physical aspects. For example, while fast, the interpolation involved in leakage schemes makes them inapt in the calculation of neutrino scattering and absorption. This makes their usage less reliable and therefore rare. Moment schemes have the real advantage of accurately treating a lot of the physics but become expensive when going to higher dimensions. The problem is similar for the full Boltzmann treatment.

One of the methods to reduce the computational cost can be to locally assume spherical symmetry, reducing the number of dimensions. This is called ray-by-ray transport as we do assume spherical symmetry along rays. While not being able to compute non-radial movements (even if some variants consider non-radial movement along one dimension), this method as been proven quite accurate when compared with fully multidimensional transport and is well tested (Glas et al., 2018; Just et al., 2018; Glas et al., 2019b; Andresen et al., 2020).

3.2   Neutrino interactions

Transporting neutrinos is a first step but all of these schemes still depend on neutrino interactions with matter. Neutrinos and anti-neutrinos are found in three different families, electron (anti-)neutrinos $\nu_e(\bar{\nu}_e)$, muon (anti-)neutrinos $\nu_\mu(\bar{\nu}_\mu)$ and tau (anti-)neutrinos $\nu_\tau(\bar{\nu}_\tau)$. The latter two do not carry an electron lepton number as they are linked with the muon and tau leptons. These leptons are most of the time not tracked in simulation codes as they are far heavier than electrons and therefore interact less (Bollig et al., 2017). Therefore we often join all four of these neutrinos together into a ν_x species. Neutrino interactions, while being on the weak side of the different forces, are of two types: charged current and neutral current weak interactions. The formers are the most prominent in CCSNe physics as they govern all the emission and absorption via $\beta^\pm$-decay and $\beta^\pm$-capture. Neutral weak interactions are less crucial for the energy deposition in the post-shock matter but dominate the production and diffusion of the heavy lepton neutrinos (ν_μ, ν_τ), and their antiparticles ($\bar{\nu}_\mu, \bar{\nu}_\tau$), in our simulations, which will affect the global neutrino luminosity as well as the PNS mass and radius.

Neutrino interactions also fall under four different categories: absorption, emission, scattering, and pair-processes. While emission and absorption are of obvious interest, scattering, is crucial for trapping of neutrinos in the core through the collapse in the case of elastic scattering as well as for the neutrino energy redistribution when we want to properly model the PNS cooling in the case of inelastic scattering.

Interaction	Reference
Emission & Absorption	
$v_e + n \rightleftarrows p + e^-$	Bruenn (1985); Horowitz (2002)
$\bar{v}_e + p \rightleftarrows n + e^+$	Bruenn (1985); Horowitz (2002)
$e^- + A(Z, N) \rightleftarrows A(Z-1, N) + v_e$	Bruenn (1985)
Isoenergetic Scattering	
$v_i + n \rightleftarrows v_i + n$	Bruenn (1985); Horowitz (2002)
$v_i + p \rightleftarrows v_i + p$	Bruenn (1985); Horowitz (2002)
$v_i + A \rightleftarrows v_i + A$	Bruenn (1985); Horowitz (1997)
Inelastic Scattering	
$v_i + e^- \rightleftarrows v_i' + e^{-\prime}$	Bruenn (1985)
Pair Processes	
$e^+ + e^- \rightleftarrows v + \bar{v}$	Bruenn (1985), Burrows et al. (2006), O'Connor (2015)
$N + N \rightleftarrows N + N + v + \bar{v}$	Burrows et al. (2006), Hannestad & Raffelt (1998), Guo & Martínez-Pinedo (2019)

Table 3.1: List of neutrino interactions from NuLib used in this work.

3.2.1 Charged vs neutral current interactions

These interactions differ in their vertex bosons, W for charged-current interactions, and Z for neutral current interactions. The reason for a different vertex boson is mainly linked to the kind of particles interacting and if the lepton number needs, or not, to be conserved.
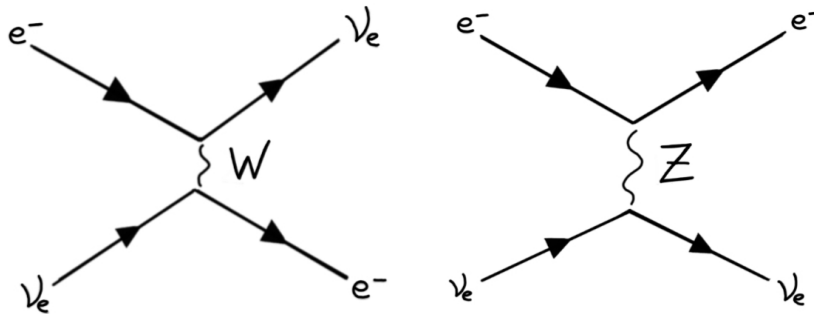

Figure 3.1: Feynmann diagrams of inelastic electron-neutrino scattering

As a simple example, we will use Fig. 3.1 which represents two of the Feynmann diagrams for the inelastic scattering of electron neutrinos on electrons. As seen on the left, in this case, the interaction requires the destruction and creation of particles through a change of species. Which indeed requires a charged W boson, and will therefore be a charged current interaction. However, as seen on the right, the second interaction implies a simple exchange of information without any change in species. This intrinsically conserves the lepton number, making it unnecessary for the vertex boson to be charged. We, therefore, have a case of neutral current interaction through a neutral Z boson.

Because of the mass difference between the Z and W bosons, charged current interactions are more probable to happen than neutral current interactions. Hence the fact that we often neglect the neutral current interactions for the electron (anti-)neutrinos in the case of scattering. We also note that the axial and vector current are different (mainly through the constants) for both types of interactions, creating different interaction kernels.

Now, absorption and emission always involve a particle transformation and are intrinsically charged current interactions. Inversely, elastic scattering on nucleons does not involve a charged interaction channel. For pair processes, as they create or destroy a pair of neutrinos, they do not inherently involve a charged current interaction. In this case, electron type neutrino pair production via electron-positron annihilation is the only interaction involving a charged current channel.

We however note that a full treatment of neutrino interactions would imply an evolution of the six species, considering heavy lepton charged interactions as well and evolving τ and μ as well as their anti-particles. We usually avoid treating heavy lepton neutrinos separately and combine them and their anti-neutrinos into a single specie: ν_x. While greatly reducing the computational cost, this could cause some discrepancies. This has lately been studied (Bollig et al., 2017, 2020) and results would highlight the importance of a systematic treatment of all six neutrino and anti-neutrino species.

3.2.2 Interactions and their implementations

In order to find the matter source term for moment schemes described in Section. 3.1, we need to implement and determine all its components for each computational cell, at each time step. For this, we separate the matter source terms into four different categories: emission/absorption, elastic scattering, inelastic scattering, and pair processes which are described in Eq. 3.15 for both the zeroth and first moment in spherical symmetry in the metric and notation of GR1D.

$$S_t = \alpha^2[S^t_{e/a} + S^t_{ES} + S^t_{IES} + S^t_{pair}]$$
$$S_r = \alpha X^2[S^r_{e/a} + S^r_{ES} + S^r_{IES} + S^r_{pair}] \tag{3.15}$$

Source terms are computed from the collision integral following Eq. 3.16, B being the collision integral, u^α the medium 4-velocity and l^α a normal vector to the 4-velocity.

$$S^\alpha = \nu^3 \int B(u^\alpha + l^\alpha)d\Omega \tag{3.16}$$

The collision integral defines the ability or not for all these interactions to happen. The collision integrals are taken from Shibata et al. (2011) and will be defined and explained in the following sections.

3.2.2.1 Emission-Absorption

We will first talk about charged-current interactions. These interactions, are mainly emission and absorption interactions. This describes the first set of interactions listed Tab. 3.1, the β-process being the first one. This was the interaction prompting the theorizing of neutrinos in 1930 by Pauli (Heilbron, 1983). This interaction, as formulated at the time, needed an additional particle in order to conserve momentum, energy, spin, and lepton number.
All the absorption and emission processes are linked with nucleons or nuclei and electrons/positrons. This means that these interactions depend heavily on the medium temperature, density, and composition.

The collision integral for this interaction is defined Eq. 3.17 with, j being the emissivity, λ the absorption mean free path, and f the neutrino distribution.

$$B = j(1 - f) - \frac{f}{\lambda} \tag{3.17}$$

We can immediately see how this collision integral behaves. $(1-f)$ represents the possibility for a new neutrino to be created in the case of a neutrino-degenerate medium. When f is close to 1, emissivity is suppressed due to all Fermi levels for the neutrino being occupied. In the same way, if f is close to 0, absorption will be almost zero as we do not have any neutrinos to absorb. This collision integral is the only one not depending on the energy or angle integrals over other neutrinos as the interaction only involves a neutrino that has a specific energy and direction of propagation.

3.2.2.2   Elastic Scattering

Iso-energetic scatterings (or elastic scattering : ES) are interactions which do not change the neutrino energy, only its direction of propagation. These interactions play a major role through the collapse as they dominate the opacity inside the PNS.

We define their collision integral Eq. 3.18 with R^{iso} the scattering interaction kernel, ν the neutrino energy. An additional term $\delta(\nu - \nu')$ forces neutrino energy conservation, therefore the difference between f and f' lays purely in the propagation angle

$$B = \nu^2 \int [f'(1-f) - f(1-f')]R^{iso}d\Omega'\delta(\nu - \nu') \qquad (3.18)$$
$$= \nu^2 \int (f' - f)R^{iso}d\Omega'\delta(\nu - \nu')$$

R^{iso} is defined differently for the scattering on neutron, proton, and nuclei. As it implies no change in energy, we do not have to integrate over all the energies. However, as the scattering changes the propagation angle, we need to consider all the available directions of propagation $d\Omega$.

3.2.2.3   Inelastic Scattering

Inelastic scattering (IES) changes the neutrino energy as well as its propagation direction. It is the main interaction allowing neutrinos to downscatter in energy to escape the core after neutrino trapping. This interaction has a high computational cost linked to the necessity of coupling all the neutrino energy bins together. These types of interactions need to be handled with great care, their fast rates making them prone to instabilities if treated through an explicit scheme. This is why we chose to use an implicit scheme even if it comes with some added computational costs.

We define the collision integral Eq. 3.19 with $R^{in/out}$ defining the inelastic kernels and f' and f having different energies and angles.

$$B = \int \nu'^2[f'(1-f)R^{in} - f(1-f')R^{out}]d\Omega'd\nu' \qquad (3.19)$$

The neutrino distribution factors indicate that inelastic scattering for one energy bin will take out energy from the pool defined by f and place it into f' and inversely for the incoming energy. For example, if f tends to 0, it will block this energy bin from losing a neutrino. However, if f tends to 1, this energy bin will not be able to incorporate a new neutrino.

3.2.2.4 Pair processes

Pair processes are named this way as they create or annihilate neutrinos in pairs. As these interactions involve either leptons (electron-positron annihilation) or nucleons (nucleon-nucleon bremsstrahlung), they depend on the medium temperature, density, and composition. As for the inelastic scattering, all the different energy bins need to be coupled together. These interactions are particularly interesting because they are the main way of creating heavy lepton neutrinos. They dominate the cooling of the PNS and therefore impact its radius and temperature evolution as well as the neutrino emission and therefore the shock revival.

The collision integral is defined in Eq. 3.20 and we use this to explicitly derive and show the source term for the 2-moments schemes (Shibata et al., 2011). We show this to find the actual source term needed in our simulations but also to highlight the different factors entering the source term.

As we can see, the source term depends on the first three moments of the neutrino distribution and the neutrino energy. The kernels $\phi_{0/1}$ showed in this equation are the zeroth and first moment of the Legendre expansion of the rate through the angle μ.

$$B = \int v'^2 dv' d\Omega' [(1 - f)(1 - \bar{f})R^{pro} - f\bar{f}R^{ann}] \tag{3.20}$$

$$
\begin{aligned}
S^\alpha = \int \frac{dv'}{v'} [& -((J - 4\pi v^3)u^\alpha + H^\alpha)(4\pi v'^3 - \bar{J})\phi_0^{pro} \\
& - \frac{\bar{H}^\alpha}{3}[(4\pi v^3 - J)\phi_1^{pro} + J\phi_1^{ann}] \\
& + (h_{\gamma\sigma}H^\gamma \bar{H}^\sigma u^\alpha + \tilde{L}_\beta^\alpha \bar{H}^\beta)[\phi_1^{pro} - \phi_1^{ann}] \\
& - (Ju^\alpha + H^\alpha)\bar{J}\phi_0^{ann}]
\end{aligned}
$$

Eq. 3.20 represents the complete interaction with the first three moments for the neutrino as well as its anti-neutrino (quantities marked with ‾). However, for the sake of computational efficiency, we sometimes resort to a simplified version of this interaction.
This simplified interaction is based on an average of the interaction kernel in order to transform our interaction rates into an effective emissivity. This emissivity is turned into an opacity following Kirchhoff's law $\kappa=\eta$/BB with BB representing the black body spectrum, κ the opacity and η the emissivity. This emissivity is then used in the emission/absorption relation Eq. 3.17. While being computationally cheap when compared to the complete method, this simplification,

among other issues, does not take neutrino degeneracy into account. This becomes problematic in the case of hyper-dense medium such as the PNS where heavy leptons are produced.

4

Work

Neutrino interactions and transport have been shown to have a strong impact on CCSNe simulations. For a recent and complete review concerning the different neutrino transport methods, see Mezzacappa et al. (2020).

This work was motivated by the expensive nature of neutrino transport in simulations. In order to reduce the cost, and hence be able to explore the explosion physics at a faster pace, we need to implement some approximations. Even if they reduce the computational cost, these approximations must be tested and, when possible, improved in order to gauge the impact on the final explosion physics and correct for any systematic bias.

A lot has been done in the past years considering interactions, approximations and their implementations into our code. The following studies : Nagakura et al. (2018); Saez et al. (2018a); Martínez-Pinedo et al. (2017); Bartl et al. (2016); Fischer (2016); Burrows et al. (2006); Duan & Qian (2005); Schwenk et al. (2004); Raffelt (2001); Arras & Lai (1999); Hannestad & Raffelt (1998); Liebendoerfer et al. (2005); Bruenn (1985); Horowitz (2002); Guo et al. (2020); Guo & Martínez-Pinedo (2019) concern various neutrino interactions and their formalism. Following these studies and in order to test the impact of some of these interactions and approximations, namely neutrino pair-processes, we decided to implement a never-before-tested formalism for the nucleon-nucleon bremsstrahlung as well as varying the transport implementation and underlying physics model of pair-processes in our simulations (Betranhandy & O'Connor, 2020).

4.1 Paper

For this work, we used the 1D, general relativistic, simulation code GR1D (O'Connor & Ott, 2010) as well as the neutrino interaction library NuLib (O'Connor, 2015). These two codes and

the versions used in the publication are publicly available here: https://github.com/evanoconnor/GR1D and https://github.com/evanoconnor/NuLib

We also used two different supernova progenitors, a low mass zero-metallicity $9.6M_\odot$ progenitor and a thoroughly studied $20M_\odot$ progenitor (O'Connor et al., 2018). We then implemented two new reaction rates in the NuLib framework for the nucleon-nucleon bremsstrahlung interaction. These theoretical rates stem from two different formalisms, namely the One-Pion-Exchange (OPE) formalism coming from Hannestad & Raffelt (1998) and the T-matrix formalism, based on theory tuned with experimental data, coming from Guo & Martínez-Pinedo (2019). The latter has never been used in core-collapse simulations.

Through the study, we tested the impact of these different formalisms, as well as the impact of the collision integral on the pair-processes rates, as explained in Sec. 3.2.2.4.

What we have found is a clear impact of the collision integral for pair-processes on the evolution of our progenitors. Simulations performed with the full collision integral show higher heavy lepton neutrino luminosities in the early phase when compared to the simplified version. This difference is mainly visible for the electron-positron annihilation interaction.

The nucleon-nucleon bremsstrahlung underlying theory has shown little impact on the non-exploding $20M_\odot$ progenitor evolution. However, the use of the T-matrix formalism does systematically increase the ν_x mean energy by ~5% at late times. This has an impact on the evolution of the exploding $9.6M_\odot$ progenitor. We suspect this increase in the mean energy to be linked to a neutrinosphere placed deeper in the PNS where the medium is hotter due to the lower neutrino interaction rate with the T-matrix formalism.

4.2   Looking forward

While these neutrino interactions and their treatment have an impact on our exploding progenitor, further multi-dimensional studies would be needed to determine the impact of this physics on the explosion mechanism when combined with the stochastic effects linked to turbulence. Another outcome of the study was the disparity between the two transport methods (full and approximate). While studying the impact of pair interactions implementations in the transport, we found out that one of the main issues with the approximation was related to the assumption of a black body for the associated neutrino. Changing the neutrino distribution from the equilibrium one to the real one should therefore allow us to improve the approximation accuracy while maintaining a low computational cost.

Bibliography

Abdikamalov, E. & Foglizzo, T. 2019, arXiv:1907.06966 [astro-ph, physics:physics], arXiv: 1907.06966

Abdikamalov, E., Pagliaroli, G., & Radice, D. 2020, arXiv:2010.04356 [astro-ph, physics:gr-qc], arXiv: 2010.04356

Akiyama, S., Wheeler, J. C., Meier, D. L., & Lichtenstadt, I. 2003, The Astrophysical Journal, 584, 954

Andresen, H., Glas, R., & Janka, H.-T. 2020, arXiv:2011.10499 [astro-ph], arXiv: 2011.10499

Arras, P. & Lai, D. 1999, Phys. Rev. D, 60, 043001, arXiv: astro-ph/9811371

Baade, W. & Zwicky, F. 1934, Proceedings of the National Academy of Science, 20, 254

Balbus, S. A. & Hawley, J. F. 1998, Reviews of Modern Physics, 70, 1

Bartl, A., Bollig, R., Janka, H.-T., & Schwenk, A. 2016, Physical Review D, 94, arXiv: 1608.05037

Basri, G. 2000, Annual Review of Astronomy and Astrophysics, 38, 485, _eprint: https://doi.org/10.1146/annurev.astro.38.1.485

Bethe, H. A. 1990, Rev. Mod. Phys., 62, 801, publisher: American Physical Society

Bethe, H. A. & Wilson, J. R. 1985, The Astrophysical Journal, 295, 14

Betranhandy, A. & O'Connor, E. 2020, arXiv:2010.02261 [astro-ph], arXiv: 2010.02261

Blondin, J. M. & Mezzacappa, A. 2007, Nature, 445, 58

Blondin, J. M., Mezzacappa, A., & DeMarino, C. 2003, ApJ, 584, 971, publisher: IOP Publishing

Bollig, R., Janka, H.-T., Lohs, A., et al. 2017, Phys. Rev. Lett., 119, 242702, publisher: American Physical Society

Bollig, R., Yadav, N., Kresse, D., et al. 2020, arXiv e-prints, 2010, arXiv:2010.10506

Bond, J. R., Arnett, W. D., & Carr, B. J. 1984, The Astrophysical Journal, 280, 825

Brandt, T. D., Burrows, A., Ott, C. D., & Livne, E. 2011, ApJ, 728, 8, publisher: American Astronomical Society

Bruch, R. J., Gal-Yam, A., Schulze, S., et al. 2020, arXiv:2008.09986 [astro-ph], arXiv: 2008.09986

Bruenn, S. W. 1985, The Astrophysical Journal Supplement Series, 58, 771

Bruenn, S. W., Blondin, J. M., Hix, W. R., et al. 2018, arXiv:1809.05608 [astro-ph], arXiv: 1809.05608

Bugli, M., Guilet, J., Obergaulinger, M., Cerdá-Durán, P., & Aloy, M. 2019, arXiv:1909.02824 [astro-ph], arXiv: 1909.02824

Buras, R., Rampp, M., Janka, H.-T., & Kifonidis, K. 2006, Astronomy & Astrophysics, 447, 1049, arXiv: astro-ph/0507135

Burrows, A., Marley, M., Hubbard, W. B., et al. 1997, The Astrophysical Journal, 491, 856

Burrows, A., Radice, D., & Vartanyan, D. 2019, arXiv:1902.00547 [astro-ph], arXiv: 1902.00547

Burrows, A., Reddy, S., & Thompson, T. A. 2006, Nuclear Physics A, 777, 356, arXiv: astro-ph/0404432

Burrows, A. & Vartanyan, D. 2020, arXiv e-prints, 2009, arXiv:2009.14157

Cabezón, R. M., Pan, K.-C., Liebendörfer, M., et al. 2018, arXiv:1806.09184 [astro-ph], arXiv: 1806.09184

Capozzi, F., Dasgupta, B., Lisi, E., Marrone, A., & Mirizzi, A. 2017, Phys. Rev. D, 96, 043016, arXiv: 1706.03360

Capozzi, F., Dasgupta, B., Mirizzi, A., Sen, M., & Sigl, G. 2018, arXiv:1808.06618 [astro-ph, physics:hep-ph], arXiv: 1808.06618

Colgate, S. A. & White, R. H. 1966, ApJ. . ., 143, 56

Da Silva, L. A. L. 1993, Astrophys Space Sci, 202, 215

Davies, M. B., Benz, W., Piran, T., & Thielemann, F. K. 1994, arXiv:astro-ph/9401032, arXiv: astro-ph/9401032

Dessart, L., Hillier, D. J., Li, C., & Woosley, S. 2012, Monthly Notices of the Royal Astronomical Society, 424, 2139, _eprint: https://onlinelibrary.wiley.com/doi/pdf/10.1111/j.1365-2966.2012.21374.x

Duan, H., Fuller, G. M., & Qian, Y.-Z. 2010, Annual Review of Nuclear and Particle Science, 60, 569, arXiv: 1001.2799

Duan, H. & Qian, Y.-Z. 2004, Physical Review D, 69, arXiv: astro-ph/0401634

Duan, H. & Qian, Y.-Z. 2005, Open Issues in Core Collapse Supernova Theory, 306, arXiv: astro-ph/0506129

Endeve, E., Cardall, C. Y., Budiardja, R. D., et al. 2012, The Astrophysical Journal, 751, 26

Ertl, T., Janka, H.-T., Woosley, S. E., Sukhbold, T., & Ugliano, M. 2016, ApJ, 818, 124, arXiv: 1503.07522

Fernández, R., Quataert, E., Kashiyama, K., & Coughlin, E. R. 2018, Monthly Notices of the Royal Astronomical Society, 476, 2366

Fischer, T. 2016, Astronomy & Astrophysics, 593, A103

Fischer, T., Typel, S., Röpke, G., Bastian, N.-U. F., & Martínez-Pinedo, G. 2020, arXiv:2008.13608 [astro-ph, physics:nucl-th], arXiv: 2008.13608

Fogli, G., Lisi, E., Marrone, A., & Tamborra, I. 2009, Journal of Cosmology and Astroparticle Physics, 2009, 030

Foglizzo, T., Kazeroni, R., Guilet, J., et al. 2015, Publ. Astron. Soc. Aust., 32, e009, arXiv: 1501.01334

Fraley, G. S. 1968, Astrophysics and Space Science, 2, 96

Fryer, C. L. 2006, Computational Methods in Transport, 1

Fryer, C. L., Brown, P. J., Bufano, F., et al. 2009, ApJ, 707, 193, publisher: American Astronomical Society

Fryer, C. L., Woosley, S. E., & Heger, A. 2001, The Astrophysical Journal, 550, 372

Fujimoto, S.-i. & Nagakura, H. 2019, arXiv:1906.09553 [astro-ph], arXiv: 1906.09553

Gal-Yam, A. 2012, 279, 253, conference Name: Death of Massive Stars: Supernovae and Gamma-Ray Bursts Place: eprint: arXiv:1206.2157

Glas, R., Janka, H.-T., Capozzi, F., et al. 2019a, arXiv:1912.00274 [astro-ph, physics:hep-ph], arXiv: 1912.00274

Glas, R., Janka, H.-T., Melson, T., Stockinger, G., & Just, O. 2018, arXiv:1809.10150 [astro-ph, physics:hep-ph], arXiv: 1809.10150

Glas, R., Just, O., Janka, H.-T., & Obergaulinger, M. 2019b, ApJ, 873, 45, arXiv: 1809.10146

Green, D. A. & Stephenson, F. R. 2003

Guilet, J., Sato, J., & Foglizzo, T. 2010, ApJ, 713, 1350, arXiv: 0910.3953

Guo, G. & Martínez-Pinedo, G. 2019, arXiv:1905.13634 [astro-ph, physics:hep-ph, physics:nucl-th], arXiv: 1905.13634

Guo, G., Martínez-Pinedo, G., Lohs, A., & Fischer, T. 2020, arXiv:2006.12051 [astro-ph, physics:hep-ph], arXiv: 2006.12051

Hanke, F., Mueller, B., Wongwathanarat, A., Marek, A., & Janka, H.-T. 2013, The Astrophysical Journal, 770, 66, arXiv: 1303.6269

Hannestad, S. & Raffelt, G. 1998, The Astrophysical Journal, 507, 339, arXiv: astro-ph/9711132

Heilbron, J. L. 1983, Historical Studies in the Physical Sciences, 13, 261, publisher: University of California Press

Hempel, M., Fischer, T., Schaffner-Bielich, J., & Liebendörfer, M. 2012, ApJ, 748, 70, publisher: IOP Publishing

Horowitz, C. J. 1997, Physical Review D, 55, 4577, arXiv: astro-ph/9603138

Horowitz, C. J. 2002, Physical Review D, 65, arXiv: astro-ph/0109209

Janka, H.-T. 1992, Astronomy and Astrophysics, 256, 452

Janka, H.-T. 2017, in Handbook of Supernovae, ed. A. W. Alsabti & P. Murdin (Cham: Springer International Publishing), 1095–1150

Jones, P. & Singleton, D. 2019, arXiv e-prints, arXiv:1907.08312

Just, O., Bollig, R., Janka, H.-T., et al. 2018, Monthly Notices of the Royal Astronomical Society, 481, 4786

Just, O., Obergaulinger, M., & Janka, H.-T. 2015, Mon. Not. R. Astron. Soc., 453, 3387, arXiv: 1501.02999

Kaplan, D. L., Chatterjee, S., Gaensler, B. M., & Anderson, J. 2008, ApJ, 677, 1201, publisher: IOP Publishing

Kasen, D., Woosley, S. E., & Heger, A. 2011, ApJ, 734, 102, publisher: American Astronomical Society

Kato, C., Nagakura, H., Hori, Y., & Yamada, S. 2020, arXiv:2001.11148 [astro-ph], arXiv: 2001.11148

Kazeroni, R. & Abdikamalov, E. 2019, arXiv, arXiv:1911.08819

Kazeroni, R., Guilet, J., & Foglizzo, T. 2016, Mon Not R Astron Soc, 456, 126, publisher: Oxford Academic

Kharusi, S. A., BenZvi, S. Y., Bobowski, J. S., et al. 2020, arXiv:2011.00035 [astro-ph, physics:hep-ex], arXiv: 2011.00035

Kippenhahn, R., Weigert, A., & Weiss, A. 2012, Stellar Structure and Evolution, 2nd edn., Astronomy and Astrophysics Library (Berlin Heidelberg: Springer-Verlag)

Kotake, K. & Kuroda, T. 2017, in Handbook of Supernovae, ed. A. W. Alsabti & P. Murdin (Cham: Springer International Publishing), 1671–1698

Kotake, K., Sawai, H., Yamada, S., & Sato, K. 2004, The Astrophysical Journal, 608, 391

Kotake, K., Takiwaki, T., Fischer, T., Nakamura, K., & Martínez-Pinedo, G. 2018, The Astrophysical Journal, 853, 170, arXiv: 1801.02703

Kresse, D., Ertl, T., & Janka, H.-T. 2020, arXiv e-prints, 2010, arXiv:2010.04728

Kuroda, T. 2020, arXiv e-prints, 2009, arXiv:2009.07733

Kuroda, T., Arcones, A., Takiwaki, T., & Kotake, K. 2020, arXiv e-prints, 2003, arXiv:2003.02004

Kuroda, T., Kotake, K., & Takiwaki, T. 2012, ApJ, 755, 11, publisher: American Astronomical Society

Lai, D. & Qian, Y.-Z. 1998, ApJ, 505, 844, arXiv: astro-ph/9802345

Lattimer, J. M. 2012, Annual Review of Nuclear and Particle Science, 62, 485, _eprint: https://doi.org/10.1146/annurev-nucl-102711-095018

LeBlanc, J. M. & Wilson, J. R. 1970, The Astrophysical Journal, 161, 541

Liebendoerfer, M., Rampp, M., Janka, H.-T., & Mezzacappa, A. 2005, The Astrophysical Journal, 620, 840, arXiv: astro-ph/0310662

Liebendorfer, M., Messer, O. E. B., Mezzacappa, A., et al. 2004, ApJS, 150, 263, publisher: American Astronomical Society

Lindquist, R. W. 1966, Annals of Physics, 37, 487

Livne, E., Burrows, A., Walder, R., Lichtenstadt, I., & Thompson, T. A. 2004, ApJ, 609, 277, publisher: American Astronomical Society

Lovegrove, E. & Woosley, S. E. 2013, The Astrophysical Journal, 769, 109

Lovegrove, E., Woosley, S. E., & Zhang, W. 2017, ApJ, 845, 103, publisher: American Astronomical Society

Maeder, A. 2009, Physics, Formation and Evolution of Rotating Stars, Astronomy and Astrophysics Library (Berlin Heidelberg: Springer-Verlag)

Maoz, D. 2017, Contemporary Physics, 58, 193, publisher: Taylor & Francis _eprint: https://doi.org/10.1080/00107514.2017.1290694

Marek, A., Dimmelmeier, H., Janka, H.-T., Müller, E., & Buras, R. 2006, Astronomy & Astrophysics, 445, 273

Martin, J. D., Carlson, J., & Duan, H. 2019, arXiv, arXiv:1911.09772

Martínez-Pinedo, G., Fischer, T., Langanke, K., et al. 2017, in Handbook of Supernovae, ed. A. W. Alsabti & P. Murdin (Cham: Springer International Publishing), 1805–1841

Matsumoto, J., Takiwaki, T., Kotake, K., Asahina, Y., & Takahashi, H. R. 2020, arXiv:2008.08984 [astro-ph], arXiv: 2008.08984

Melson, T., Janka, H.-T., & Marek, A. 2015, ApJ, 801, L24, arXiv: 1501.01961

Melson, T., Kresse, D., & Janka, H.-T. 2020, ApJ, 891, 27, arXiv: 1904.01699

Mezzacappa, A. & Bruenn, S. W. 1993a, The Astrophysical Journal, 405, 669

Mezzacappa, A. & Bruenn, S. W. 1993b, The Astrophysical Journal, 410, 740

Mezzacappa, A. & Bruenn, S. W. 1993c, The Astrophysical Journal, 405, 637

Mezzacappa, A., Endeve, E., Messer, O. E. B., & Bruenn, S. W. 2020, arXiv:2010.09013 [astro-ph, physics:gr-qc], arXiv: 2010.09013

Mihalas, D. & Mihalas, B. W. 1984, New York, Oxford University Press, 1984, 731 p.

Minerbo, G. N. 1978, Journal of Quantitative Spectroscopy and Radiative Transfer, 20, 541

Murchikova, L., Abdikamalov, E., & Urbatsch, T. 2017

Murphy, J. W., Mabanta, Q., & Dolence, J. C. 2019, arXiv:1904.09444 [astro-ph], arXiv: 1904.09444

Mösta, P., Ott, C. D., Radice, D., et al. 2015, Nature, 528, 376

Mösta, P., Radice, D., Haas, R., Schnetter, E., & Bernuzzi, S. 2020, arXiv e-prints, 2003, arXiv:2003.06043

Mösta, P., Richers, S., Ott, C. D., et al. 2014, ApJ, 785, L29, arXiv: 1403.1230

Müller, B. 2016, Publications of the Astronomical Society of Australia, 33

Müller, B. 2019, arXiv:1904.11067 [astro-ph, physics:hep-ex, physics:hep-ph], arXiv: 1904.11067

Müller, B., Gay, D., Heger, A., Tauris, T., & Sim, S. A. 2018a, Monthly Notices of the Royal Astronomical Society, 479, 3675, arXiv: 1803.03388

Müller, B. & Janka, H.-T. 2015, Monthly Notices of the Royal Astronomical Society, 448, 2141, arXiv: 1409.4783

Müller, B., Melson, T., Heger, A., & Janka, H.-T. 2017, Monthly Notices of the Royal Astronomical Society, 472, 491, arXiv: 1705.00620

Müller, B., Tauris, T. M., Heger, A., et al. 2018b, arXiv:1811.05483 [astro-ph], arXiv: 1811.05483

Müller, B. & Varma, V. 2020, arXiv e-prints, 2007, arXiv:2007.04775

Nagakura, H., Burrows, A., Radice, D., & Vartanyan, D. 2019a, Monthly Notices of the Royal Astronomical Society, 490, 4622

Nagakura, H., Furusawa, S., Togashi, H., et al. 2018, arXiv:1812.09811 [astro-ph, physics:nucl-th], arXiv: 1812.09811

Nagakura, H., Sumiyoshi, K., & Yamada, S. 2019b, arXiv:1907.04863 [astro-ph, physics:gr-qc], arXiv: 1907.04863

Nagakura, H., Sumiyoshi, K., & Yamada, S. 2019c, arXiv:1906.10143 [astro-ph], arXiv: 1906.10143

Ober, W. W., El Eid, M. F., & Fricke, K. J. 1983, Astronomy and Astrophysics, 119, 61

Obergaulinger, M. & Aloy, M. 2020, Monthly Notices of the Royal Astronomical Society, 492, 4613

Obergaulinger, M., Janka, H.-T., & Aloy, M. A. 2014, Mon Not R Astron Soc, 445, 3169

Obergaulinger, M., Just, O., & Aloy, M. 2018, Journal of Physics G: Nuclear and Particle Physics, 45, 084001, arXiv: 1806.00393

O'Connor, E. 2015, ApJS, 219, 24, arXiv: 1411.7058

O'Connor, E. 2017, in Handbook of Supernovae, ed. A. W. Alsabti & P. Murdin (Cham: Springer International Publishing), 1555–1572

O'Connor, E., Bollig, R., Burrows, A., et al. 2018, arXiv:1806.04175 [astro-ph], arXiv: 1806.04175

O'Connor, E. & Couch, S. 2018, arXiv:1807.07579 [astro-ph], arXiv: 1807.07579

O'Connor, E. & Ott, C. D. 2010, Class. Quantum Grav., 27, 114103, arXiv: 0912.2393

O'Connor, E. & Ott, C. D. 2011, ApJ, 730, 70, arXiv: 1010.5550

Padilla-Gay, I., Shalgar, S., & Tamborra, I. 2020, arXiv e-prints, 2009, arXiv:2009.01843

Pan, K.-C., Mattes, C., O'Connor, E. P., et al. 2018, arXiv:1806.10030 [astro-ph], arXiv: 1806.10030

Pejcha, O. & Thompson, T. A. 2012, The Astrophysical Journal, Volume 746

Pesnell, W. D. 1986, The Astrophysical Journal, 301, 204

Pons, J. A., Ibáñez, J. M., & Miralles, J. A. 2000, Mon Not R Astron Soc, 317, 550, publisher: Oxford Academic

Powell, J. & Müller, B. 2018, arXiv:1812.05738 [astro-ph], arXiv: 1812.05738

Powell, J., Müller, B., & Heger, A. 2021, arXiv:2101.06889 [astro-ph], arXiv: 2101.06889

Radice, D., Burrows, A., Vartanyan, D., Skinner, M. A., & Dolence, J. C. 2017, ApJ, 850, 43, arXiv: 1702.03927

Radice, D., Morozova, V., Burrows, A., Vartanyan, D., & Nagakura, H. 2018, arXiv:1812.07703 [astro-ph, physics:gr-qc], arXiv: 1812.07703

Raffelt, G. G. 2001, ApJ, 561, 890, arXiv: astro-ph/0105250

Rahman, N., Just, O., & Janka, H.-T. 2019, arXiv:1901.10523 [astro-ph, physics:gr-qc], arXiv: 1901.10523

Rampp, M. & Janka, H.-T. 2002, Astronomy & Astrophysics, 396, 361, arXiv: astro-ph/0203101

Reichert, M., Obergaulinger, M., Eichler, M., Aloy, M.-, & Arcones, A. 2020, arXiv:2010.02227 [astro-ph], arXiv: 2010.02227

Rosenblum, E., Garaud, P., Traxler, A., & Stellmach, S. 2011, The Astrophysical Journal, 731, 66

Rosswog, S. & Liebendoerfer, M. 2003, Monthly Notices of the Royal Astronomical Society, 342, 673, arXiv: astro-ph/0302301

Ruffert, M., Janka, H.-T., & Schaefer, G. 1995, arXiv:astro-ph/9509006, arXiv: astro-ph/9509006

Saez, M. M., Civitarese, O., & Mosquera, M. E. 2018a, International Journal of Modern Physics D, 1850116, arXiv: 1808.03249

Saez, M. M., Mosquera, M. E., & Civitarese, O. 2018b, Boletín de la Asociación Argentina de Astronomía, 60, 3

Sawada, R. & Suwa, Y. 2020, arXiv:2010.05615 [astro-ph], arXiv: 2010.05615

Scheck, L., Kifonidis, K., Janka, H.-T., & Müller, E. 2006, A&A, 457, 963

Schmitt, D. 1987, Astronomy and Astrophysics, 174, 281

Schneider, A. S., O'Connor, E., Granqvist, E., Betranhandy, A., & Couch, S. M. 2020, arXiv:2001.10434 [astro-ph, physics:nucl-th], arXiv: 2001.10434

Schneider, A. S., Roberts, L. F., Ott, C. D., & O'connor, E. 2019, arXiv:1906.02009 [astro-ph, physics:nucl-th], arXiv: 1906.02009

Schwenk, A., Jaikumar, P., & Gale, C. 2004, Physics Letters B, 584, 241, arXiv: nucl-th/0309072

Sekiguchi, Y. 2010, Class. Quantum Grav., 27, 114107, publisher: IOP Publishing

Shibata, M., Kiuchi, K., Sekiguchi, Y.-i., & Suwa, Y. 2011, Progress of Theoretical Physics, 125, 1255, arXiv: 1104.3937

Smartt, S. J. 2009, Annu. Rev. Astron. Astrophys., 47, 63, arXiv: 0908.0700

Spruit, H. C., Knobloch, E., & Roxburgh, I. W. 1983, Nature, 304, 520, number: 5926 Publisher: Nature Publishing Group

Steiner, A. W., Hempel, M., & Fischer, T. 2013, The Astrophysical Journal, 774, 17

Stockinger, G., Janka, H.-T., Kresse, D., et al. 2020, arXiv:2005.02420 [astro-ph], arXiv: 2005.02420

Stringfellow, G. S. & Woosley, S. E. 1983, 15, 955, conference Name: Bulletin of the American Astronomical Society

Sumiyoshi, K., Takiwaki, T., Matsufuru, H., & Yamada, S. 2014, ApJS, 216, 5, publisher: American Astronomical Society

Sumiyoshi, K. & Yamada, S. 2012, ApJS, 199, 17, publisher: American Astronomical Society

Sumiyoshi, K., Yamada, S., Suzuki, H., et al. 2005, ApJ, 629, 922, publisher: American Astronomical Society

Swesty, F. D. & Myra, E. S. 2009, ApJS, 181, 1, publisher: American Astronomical Society

Takahashi, K. & Langer, N. 2020, arXiv:2010.13909 [astro-ph], arXiv: 2010.13909

Tamborra, I., Huedepohl, L., Raffelt, G., & Janka, H.-T. 2017, ApJ, 839, 132, arXiv: 1702.00060

Thielemann, F.-K. 2018

Thielemann, F.-K., Eichler, M., Panov, I. V., & Wehmeyer, B. 2017, Annu. Rev. Nucl. Part. Sci., 67, 253, arXiv: 1710.02142

Thorne, K. S. 1981, Monthly Notices of the Royal Astronomical Society, 194, 439

Ugliano, M., Janka, H.-T., Marek, A., & Arcones, A. 2012, The Astrophysical Journal, 757, 69

Umeda, H. & Nomoto, K. 2002, The Astrophysical Journal, 565, 385

Vartanyan, D., Burrows, A., & Radice, D. 2019, arXiv:1906.08787 [astro-ph], arXiv: 1906.08787

Vartanyan, D., Burrows, A., Radice, D., Skinner, A., & Dolence, J. 2018, arXiv:1809.05106 [astro-ph], arXiv: 1809.05106

Walk, L., Tamborra, I., Janka, H.-T., & Summa, A. 2018, Phys. Rev. D, 98, 123001, arXiv: 1807.02366

Walk, L., Tamborra, I., Janka, H.-T., & Summa, A. 2019, arXiv e-prints, 1901, arXiv:1901.06235

Wolfenstein, L. 1978, Physical Review D, 17, 2369

Woosley, S. E. 2017, ApJ, 836, 244, publisher: American Astronomical Society

Woosley, S. E., Heger, A., & Weaver, T. A. 2002, Rev. Mod. Phys., 74, 1015, publisher: American Physical Society

Woosley, S. E. & Weaver, T. A. 1986, Annual Review of Astronomy and Astrophysics, 24, 205

Yakunin, K., Marronetti, P., Mezzacappa, A., et al. 2010, arXiv:1011.3752 [astro-ph], arXiv: 1011.3752

Yamada, S. 1997, ApJ, 475, 720, publisher: American Astronomical Society

Yasin, H., Schäfer, S., Arcones, A., & Schwenk, A. 2018, arXiv e-prints, 1812, arXiv:1812.02002

Zaizen, M., Cherry, J. F., Takiwaki, T., et al. 2019, arXiv:1908.10594 [astro-ph, physics:hep-ph], arXiv: 1908.10594

Zhang, W., Howell, L., Almgren, A., et al. 2013, The Astrophysical Journal Supplement Series, 204, 7

Impact of neutrino pair-production rates in core-collapse supernovae

Aurore Betranhandy and Evan O'Connor

The Oskar Klein Centre, Department of Astronomy, Stockholm University,
AlbaNova, SE-106 91 Stockholm, Sweden

In this paper, we present a careful study on the impact of neutrino pair-production on core-collapse supernovae via spherically-symmetric, general-relativistic simulations of two different massive star progenitors with energy-dependent neutrino transport. We explore the impact and consequences of both the underlying microphysics and the implementation in the radiation transport algorithms on the supernova evolution, neutrino signal properties, and the explosion dynamics. We consider the two dominant neutrino pair-production processes found in supernovae, electron-positron annihilation as well as nucleon-nucleon bremsstrahlung in combination with both a simplified and a complete treatment of the processes in the radiation transport algorithms. We find that the use of the simplified prescription quantitatively impacts the neutrino signal at the 10% level and potentially the supernova dynamics, as we show for the case of a zero-metallicity, $9.6 M_\odot$ progenitor. We also show that the choice of nucleon-nucleon bremsstrahlung interaction can also have a quantitative impact on the neutrino signal. A self-consistent treatment with state-of-the-art microphysics is suggested for precision simulations of core collapse, however the simplified treatment explored here is both computationally less demanding and results in a qualitatively similar evolution.

I. INTRODUCTION

Core-collapse supernovae (CCSNe) represent the last stage of massive star evolution for stars more massive than $8 M_\odot$ and, along with neutron star-neutron star mergers and Type-Ia supernovae, are one of the main channels of galactic nucleosynthesis [1,2]. Not only do CCSNe contribute to the production of heavy elements but they are also the main birth site of neutron stars and stellar mass black holes.

Supernovae are also true multimessenger events, producing neutrinos, gravitational waves, as well as photons. The most readily available observable is the electromagnetic signal, for example, the Zwicky Transient Facility observed over 800 CCSNe in 2018 [3]. In the fortunate case of a galactic supernova, the two other channels, gravitational waves and neutrinos, become possible [4,5]. At the onset of the explosion, the outside layers of the progenitor star shroud the core and prevent photons from carrying direct information from the core. Neutrinos and gravitational waves are the only direct channels helping us deciphering the physics of the early explosion. The supernova mechanism is thus still largely observationally unconstrained. Regardless,

numerical simulations performed by different groups allow us to test and refine the theories we have [6–12].

The main theory is the neutrino-driven supernova mechanism. Once the fusion reactions in the core stop and gravity overcomes the electron degeneracy pressure, the collapse begins. At nuclear density the core stiffens and the collapse stops and rebounds outwards. The information about this bounce propagates through the in-falling mater, reaching supersonic velocities and creating a shock. This shock propagates out flowing against the ram pressure of the infalling layers and dissociating the nuclei accreting through. In doing so, the shock loses energy and ends up stalling. The neutrino-driven mechanism is the idea [13] that the neutrinos can reenergize the shock by transferring energy from the cooling protoneutron star (PNS) to the material behind the shock through absorption in the so-called gain layer. Studies have shown that this heating is very sensitive to the neutrino spectrum, which in turn is sensitive to the emission and absorption processes [12,14–17]. While much progress has been made in 3D [9,18–29], the theory is not yet completed. Progress on all fronts is needed to further constrain CCSN theories and the underlying physics.

Neutrino transport is one of the most difficult aspects of modeling supernova simulations. A completely self-consistent treatment of neutrinos would involve solving the 6D Boltzmann equation over the course of the simulation, along with capturing all of the important interactions with the medium. This is too computationally expensive,

especially with the required resolution, though see [30]. Therefore, we often resort to approximate schemes such as flux limited diffusion or truncated moment schemes. In this study, we use a moment scheme [31,32]. We essentially treat the neutrinos like a fluid, evolving the energy density and momentum density. Neutrinos are produced inside of the PNS, where it is optically thick to neutrinos, and diffuse out into semitransparent, optically-thin matter in the gain region behind the shock. This change in the qualitative nature of the environment makes the neutrino transport complex as neutrinos transition from being strongly coupled to the matter to a free-flowing behavior, and therefore neither assumption can be used globally to simplify the problem. The main type of neutrinos interacting in the gain region are the electron type neutrinos and antineutrinos through charged-current interactions. However, heavy lepton neutrinos (ν_μ, $\bar{\nu}_\mu$, ν_τ, and $\bar{\nu}_\tau$), which mainly cool the PNS, also play a major role. Hence, their interactions with matter need to be treated as accurately as possible. The main production channel for heavy-lepton neutrinos is via pair-production, where a pair consisting of a neutrino and an antineutrino is formed. The dominant production processes for these pairs in CCSNe include electron-positron annihilation and nucleon-nucleon bremsstrahlung. Charged-current interactions (either emission or absorption) of single heavy-lepton neutrinos with muons or taus are suppressed due to those charged lepton's large mass, although see [33–35].

In this paper, different treatments for the thermal pair-production processes are tested. These interactions are challenging to treat as they involve not just one neutrino, but two, which necessitates the coupling of the species and of the energy bins. This had often lead to approximations for their inclusion in neutrino transport algorithms [36]. As part of this paper, we assess one such approximation with the goal of reducing computational expense while maintaining the fidelity of the solution. Not only are the neutrino pair-production processes computationally complex, another problem inherent in the nucleon-nucleon bremsstrahlung interaction is its uncertain nuclear physics. For this reason, we consider two different ways of treating the interaction. First we consider the commonly used one pion exchange (OPE) formalism by Hannestad and Raffelt [37]. We also consider a recent T-matrix formalism formulated by Guo *et al.* [38] based on chiral effective field theory fitted to experimental phase shifts. We test these two different formalisms as well as a simplified version for the nucleon-nucleon bremsstrahlung based on [39]. For electron-positron annihilation we follow the formalism described in Bruenn *et al.* [40] as well as a simplified version [36]. We perform 1D simulations for each of the six combinations of different treatments for two different progenitors. We use a 20M$_\odot$ progenitor, a model studied across many CCSN codes in [6] and a zero-metallicity, 9.6-M$_\odot$ progenitor, which has the property of exploding in

1D simulations. We explore the impact of all the different treatments on the early supernova evolution, the explosion parameters, and the neutrino luminosities and mean energies. Furthermore, we scrutinize the validity of our simplified approximation used in order to inform future multidimensional simulations on the impact of heavy-lepton neutrino pair-production treatments.

The outline of this paper is as follows. In Sec. II, we overview the simulation code we use, GR1D, and we describe the different interactions involved in our study and their implementation in GR1D and NuLib. We also present the two progenitors and their history of use in CCSN simulations. In Sec. III A, we describe the results on the 20M$_\odot$ progenitor and Sec. III B the ones of the 9.6M$_\odot$ progenitor. We finally conclude in Sec. IV.

II. METHODS

A. GR1D

For all the simulations presented in this paper we use the general-relativistic radiation-hydrodynamic code GR1D [36,41]. For the neutrino transport, GR1D uses a moment scheme [32,42]. It evolves the 0th and 1st moment of the neutrino distribution function for multiple neutrino species and multiple neutrino energies. The neutrino-matter interaction terms (completely local) are solved implicitly while the nonlocal spatial fluxes are solved explicitly. The evolution is done in the coordinate (or laboratory) frame but full velocity dependence is included in the neutrino-matter interactions and to order v/c in the spatial transport terms. We present the model moment evolution equations here, highlighting the neutrino-matter interaction source terms and refer the reader to [36] for full details,

$$\partial_t[E] + \frac{1}{r^2}\partial_r\left[\frac{\alpha r^2}{X^2}F_r\right] + \partial_\epsilon[\ldots] = G_t + C_t \qquad (1)$$

and

$$\partial_t[F_r] + \frac{1}{r^2}\partial_r\left[\frac{\alpha r^2}{X^2}P_{rr}\right] + \partial_\epsilon[\ldots] = G_r + C_r \qquad (2)$$

where E and F_r are the zeroth and first moments of the species and energy-dependent neutrino distribution functions, P_{rr} is the 2nd moment, and in the M1 approximation is taken as an analytic expression involving the first two moments, specifically, we use the Minerbo closure [43]. Here, and in the following, we suppress the energy and species dependence of these moments and source terms, unless needed. α and X are metric functions, $\partial_\epsilon[\ldots]$ refers to the energy-space fluxes, and $G_{t/r}$ and $C_{t/r}$ are the geometric and neutrino-matter source terms, respectively. For the full expression for $\partial_\epsilon[\ldots]$ and $G_{t/r}$ we refer the reader to [36], since in this paper we focus on the neutrino-matter

interactions, we explicitly write $C_{t/r}$ here and describe each term below,

$$C_t = \alpha^2 [S_{e/a}^t + S_{iso}^t + S_{scatter}^t + S_{pair}^t] \qquad (3)$$

$$C_r = \alpha X^2 [S_{e/a}^r + S_{iso}^r + S_{scatter}^r + S_{pair}^r] \qquad (4)$$

In GR1D, neutrino-matter interactions fall into four categories. (i) $[S_{e/a}^\alpha]$ Charged-current neutrino-matter interactions, where electron type neutrinos and antineutrinos are absorbed or emitted from the matter. (ii) $[S_{iso}^\alpha]$ Elastic scattering interactions, where neutrinos of all types scatter on nucleons and nuclei. These scatters change the neutrino direction but maintain their energy. For the emission, absorption and the elastic scattering interactions, we treat the source terms in the following way:

$$S_{e/a}^\alpha = [\eta - \kappa_a J]u^\alpha - \kappa_a H^\alpha \qquad (5)$$

$$S_{iso}^\alpha = -\kappa_s H^\alpha \qquad (6)$$

where η is the emissivity, κ_a and κ_s are the absorption and scattering opacities respectively, u^α is the fluid four-velocity, and J and H^α are the zeroth and first neutrino moments in the fluid frame (see [36] for detailed expressions of J and H^α in terms of E and F_r and the closure relation).

(iii) $[S_{scatter}^\alpha]$ Inelastic scattering interactions, where neutrinos scatter on electrons and appreciably change their energy and direction. This interaction necessitates a coupling of neutrino energy bins within a neutrino species. For inelastic neutrino-electron scattering, we use the source terms described in Shibata *et al.* [32]. In this study, we ignore inelastic scattering on nucleons.

Finally, (iv) $[S_{pair}^\alpha]$, pair-production interactions where a neutrino-antineutrino pair is emitted. In GR1D, we only consider pair-production interactions involving heavy-lepton neutrinos (ν_μ, $\bar\nu_\mu$, ν_τ, and $\bar\nu_\tau$) since the interactions involving electron type neutrino-antineutrino pairs are dwarfed by the charged-current rates for these neutrinos. With GR1D, there are two ways of including S_{pair}^α into the evolution equations. The first is a simplified method where we generate simplified emissivities ($\eta_{eff}^{\nu\bar\nu}$) and absorption coefficients ($\kappa_{a,eff}^{\nu\bar\nu}$) for each neutrino energy group and treat these terms like the emission and absorption interactions in (i) above. The precise form of these coefficients depends on the particular pair-production process and are described in the following section. This method is computational efficient as it does not require coupling neutrinos of different energies together when performing the implicit solution of the evolution equations and the interaction rates depend only on the temperature, electron fraction, density and neutrino energy. However, in general, these neutrino pair-production processes do depend on the occupation

density of more than one neutrino and therefore this method is an approximation. The second method is more complete, but also more computationally expensive. It uses kernels to describe the interaction between two neutrinos of different energies (and species) and takes into account the final state neutrino occupation (for emission) and initial state neutrino occupation (for annihilation) hence, coupling different energy groups. The source term for this method is based on [32] and follows from taking the appropriate angular moments of the full Boltzmann collision integral for neutrino-antineutrino annihilation,

$$S_{pair}^\alpha = \nu^3 \int d\Omega B(\nu, \Omega)(u^\alpha + \ell^\alpha), \qquad (7)$$

where ν is the neutrino energy, u^α is the fluid four-velocity, ℓ^α is a unit vector perpendicular to u^α, and $B(\nu, \Omega)$ is,

$$B(\nu, \Omega) = \int \nu'^2 d\nu' d\Omega' [(1 - f')(1 - f)R^{pro}(\nu, \nu', \mu)$$
$$- ff'R^{ann}(\nu, \nu', \mu)], \qquad (8)$$

where for clarity we have suppressed the ν, and ν' as well as Ω and Ω' dependence in each of the occupation probabilities, f and f', respectively. μ, which is a function of both the prime and unprimed angular variables, is the cosine of the angle between the neutrino and antineutrino. As is typically done, we assume an angular expansion form of the production and annihilation kernels, $R^{pro/ann} \sim R_0^{pro/ann} + \mu R_1^{pro/ann}$, where $R_{0/1}^{pro/ann}$ only depends on the energies of the two neutrinos involved and the underlying interaction (see the following section). Following [32], Eqs. (7) and (8) are reduce to a single integral over ν' where the integrand depends only on the primed and unprimed, zeroth, first, and second neutrino moments and the $R_{0/1}^{pro/ann}$ kernels,

$$S_{pair}^\alpha = \int \frac{d\nu'}{\nu'} \left[-\{(J - 4\pi\nu^3)u^\alpha + H^\alpha\}(4\pi\nu'^3 - J')R_0^{pro} \right.$$
$$- \frac{H'^\alpha}{3}\{(4\pi\nu^3 - J)R_1^{pro} + JR_1^{ann}\}$$
$$+ (h_{\gamma\sigma}H^\gamma H'^\sigma u^\alpha + \tilde L_\beta^\alpha H'^\beta)[R_1^{pro} - R_1^{ann}]$$
$$\left. - (Ju^\alpha + H^\alpha)J'R_0^{ann} \right], \qquad (9)$$

where $h_{\alpha\beta} = g_{\alpha\beta} + u_\alpha u_\beta$ is the projection operator and $\tilde L^{\alpha\beta}$ is the traceless $L^{\alpha\beta}$, the second-moment tensor in the fluid frame (analogous to $P^{\alpha\beta}$ above, which is the coordinate frame second moment).

B. Implementation in NuLib

NuLib (http://www.nulib.org) is an open-source neutrino interaction library [36] that we use to produce tables of the neutrino-matter interaction coefficients for interpolation during our simulations. For this work, we utilized the interactions described in Table I, which are divided into the four main interaction types described above. In this work, we focused on the heavy-lepton pair-production processes and the accuracy of the prescriptions used in the transport for these interactions. For this reason, we describe these in detail below.

The two main neutrino pair-production processes in a CCSN environment are electron-positron pair annihilation and nucleon-nucleon bremsstrahlung. As discussed in Sec. II A, we consider both an simplified prescription for these interactions and a kernel treatment. For the electron-positron pair annihilation the underlying interaction is the same in these two methods, described in [39,40]. We used NuLib to compute $R_0^{\mathrm{ann/pro}}$ and $R_1^{\mathrm{ann/pro}}$ for use in Eq. (9), which gives the neutrino pair annihilation and production rates as a function of the two neutrino energies, ν and ν', for a given value of the matter temperature and electron chemical potential. For the simplified version of neutrino emission from electron-positron annihilation (see [36] for more details), we compute $\eta_{\mathrm{eff}}^{e^-e^+}(\nu)$ by assuming

TABLE I. List of neutrino interactions from NuLib used in this work.

Interaction	Reference
Emission & Absorption	
$\nu_e + n \rightleftarrows p + e^-$	Bruenn (1985) [40]; Horowitz (2002) [44]
$\bar{\nu}_e + p \rightleftarrows n + e^+$	Bruenn (1985) [40]; Horowitz (2002) [44]
$e^- + A(Z,N) \rightleftarrows A(Z-1,N) + \nu_e$	Bruenn (1985) [40]
Isoenergetic Scattering	
$\nu_i + n \rightleftarrows \nu_i + n$	Bruenn (1985) [40]; Horowitz (2002) [44]
$\nu_i + p \rightleftarrows \nu_i + p$	Bruenn (1985) [40]; Horowitz (2002) [44]
$\nu_i + A \rightleftarrows \nu_i + A$	Bruenn (1985) [40]; Horowitz (1997) [45]
Inelastic Scattering	
$\nu_i + e^- \rightleftarrows \nu_i' + e^{-\prime}$	Bruenn (1985) [40]
Pair Processes	
$e^+ + e^- \rightleftarrows \nu + \bar{\nu}$	Bruenn (1985) [40], Burrows et al. (2006) [39], O'Connor (2015) [36]
$N + N \rightleftarrows N + N + \nu + \bar{\nu}$	Burrows et al. (2006) [39], Hannestad and Raffelt (1998) [37], & Guo and Martinez-Pinedo (2019) [38]

$R_1^{\mathrm{pro/ann}} = 0$ (i.e., isotropic emission), no final state neutrino blocking, and integrating over all possible ν'. We construct an simplified absorption by invoking Kirchhoff's law, $\kappa_{\mathrm{eff}}^{e^-e^+}(\nu) = \eta_{\mathrm{eff}}^{e^-e^+}(\nu)/BB(\nu, T)$, where BB is the black body intensity for heavy-lepton neutrinos with energy ν in a medium with temperature T. This ensures there is no net emission in regions where the neutrino field is the same as the equilibrium neutrino field and no absorption in regions where the neutrino field is negligible. This is an approximation.

The other main neutrino pair-production process of importance in CCNSe is nucleon-nucleon bremsstrahlung. Before this work, this interaction was included in NuLib only via an simplified way taken from Burrows et al. (2006) [39]. The simplified single neutrino emissivity (with units of erg cm^{-3} s^{-1} srad^{-1} MeV^{-1}) is taken as,

$$\eta_{\mathrm{eff}}^{\mathrm{NN}}(\nu) = 0.234 \frac{Q_{nb}}{4\pi T} \left(\frac{\nu}{T}\right)^{2.4} e^{\frac{-1.1\nu}{T}}, \qquad (10)$$

where

$$Q_{nb} = 2.0778 \times 10^{30} \text{ erg cm}^{-3} \text{ s}^{-1}$$
$$\times \zeta \left(x_n^2 + x_p^2 + \frac{28}{3} x_n x_p\right) \rho_{14}^2 T^{5.5}, \qquad (11)$$

is the total energy emission rate for a pair of neutrinos, ζ is a correction factor (taken to be 0.5 [39]), $x_{n/p}$ is the mass fraction of neutron and protons, ρ_{14} is the density scaled to 10^{14} g cm^{-3}, and T is the matter temperature. As is the case for electron-positron annihilation, we construct a simplified absorption by invoking Kirchhoff's law, $\kappa_{\mathrm{eff}}^{NN}(\nu) = \eta_{\mathrm{eff}}^{NN}(\nu)/BB(\nu, T)$. This simplified emissivity was made in the nondegenerate-medium limit assuming an OPE potential. It is only dependant on the nucleon number densities and the temperature of the medium. This simplified emissivity stemmed from earlier work in [46] where they explicitly showed for CCSN conditions the difference in the emissivity when derived from the non-degenerate limit compared to the arbitrary degeneracy calculation. They show that the nondegenerate limit provides good results up to $\eta = \mu_n/T \sim 0$ (roughly several 10^{13} g cm^{-3}) where the difference compared to the arbitrary degeneracy is $\sim 12\%$, this rises to $\sim 30\%$ at the degeneracies typically found in the core. This is consistent with our findings, which are discussed below. In the early phases of a CCSN explosion, the nucleons at the densities of interest are rarely degenerate, however at latter stages, during the cooling of the PNS for example, the densities where the nucleon-nucleon bremsstrahlung rates can impact the evolution and emission may be in the degenerate regime, therefore this method may need to be reconsidered.

In this work, we extend NuLib to include kernels for the nucleon-nucleon bremsstrahlung process in addition to the

electron-positron annihilation process. The nucleon-nucleon bremsstrahlung kernels follow the form of,

$$R^{\text{pro}}(\omega, \mu) = G_F^2 C_a^2 n_B (\hbar c^3)(3 - \mu) S_\sigma(\omega), \quad (12)$$

where n_B is the baryon density, $G_F \sim 1.166 \times 10^{-11} \text{ MeV}^{-2}$ is the weak coupling constant, $C_a = g_A/2$ with $g_A \sim -1.26$ is the axial vector coupling constant, $\omega = \nu + \nu'$ is the sum of the two neutrino energies, and $S_\sigma(\omega)$ is the structure function. As for the electron-positron annihilation kernel, we decompose R^{pro} into Legendre moments, $R_{0/1}^{\text{pro}}$. Given the dependence on μ in Eq. (12), this is a trivial decomposition and $R_1^{\text{pro}} = -R_0^{\text{pro}}/3$. In order to obtain $R_{0/1}^{\text{ann}}$ in accordance with detailed balance, we use $R_{0/1}^{\text{pro}} = e^{-\omega/T} R_{0/1}^{\text{ann}}$.

The exact definition of $S_\sigma(\omega)$ depends on the underlying interaction and in this work we consider two different models. First, we include the classic nucleon-nucleon bremsstrahlung rates described in Hannestad and Raffelt (1998) [37]. Similar to the parametrization above, this interaction is derived from the OPE potential, but also includes in the structure function effects such as a non-vanishing pion mass, effects from multiple-scatterings, and is valid for both the degenerate and nondegenerate limits with an interpolation for semidegenerate regions. The structure function is [37],

$$S_\sigma(\omega) = \frac{\Gamma}{\omega^2 + (\Gamma g(y,\eta)/2)^2} s(\omega/T, y). \quad (13)$$

This structure function is for an arbitrary nucleon interacting with a like nucleon with a nucleon density (n_N), temperature (T), and the degeneracy factor, $\eta = p_F^2/(2m_N T)$ (where $p_F^2 = \hbar(3\pi^2 n_N)^{1/3}$ is the Fermi momentum of the nucleons with mass m_N). The spin-fluctuation rate (Γ), gives the strength of the bremsstrahlung. This structure function is a Lorentzian used as an ansatz, it does not describe realistically the physics underlying the interaction but has the correct behavior for the limiting cases [37]. Also present in the structure function are dimensionless functions $g(y,\eta)$ and $s(\omega/T, y)$ that are a function representing the multiscattering effect and the interpolation of the nucleon structure function between degenerate and nondegenerate medium, respectively. For completeness,

$$\Gamma = \frac{8\sqrt{2\pi}\alpha_\pi}{3\pi^2}\eta^{3/2}\frac{T^2}{m_N c^2},$$

$$y = \frac{m_\pi^2}{m_N T}, \quad (14)$$

where α_π and m_π are the pion fine-structure constant and the pion mass, respectively. For detailed expressions for $g(y,\eta)$ and $s(\omega/T, y)$, see [37] or the bremsstrahlung

routines in NuLib (http://www.nulib.org). In NuLib, we compute a table of $R_{0/1}^{\text{pro/ann}}$ as a function of an arbitrary nucleon density n_N, the temperature T, for the pair of neutrino energies ν and ν'. During our simulation we interpolate this table for three values of the nucleon density, $n_n, n_p, \sqrt{n_n n_p}$, and combine the rates with weights of 1, 1, and 28/3, respectively [39].

The second nucleon-nucleon bremsstrahlung interaction we consider is the recent formalism from Guo and Martinez-Pinedo [38]. They calculate the structure function $(S_\sigma(\omega))$ used in Eq. (12) by using the T-matrix element based on the χEFT potential presented in Entem *et al.* [47]. A similar method was previously explored in [48]. A followup in [49] where the T-matrix formalism was shown to give modestly different results in supernova simulations from the OPE prescription above. The T-matrix formalism used in [38] is an improvement over [48] with the inclusion of off-shell T-matrix elements in addition to on-shell elements. In NuLib, we utilize the table of $S_\sigma(\omega)$ values provided by the authors. We interpolate this four dimensional table (ρ, T, Y_e, and $\nu + \nu'$) for use in Eq. (12) in order to construct our tables.

We conclude this section by comparing each of the pair-production processes and prescriptions utilized in this work at different CCSN-like conditions. The results are shown in Fig. 1, where we compare the single neutrino number isotropic emissivities, ignoring any final state neutrino blocking, as a function of energy at four densities. Following [48], we use the following relationship between density and temperature typically found in CCSN environments,

$$T_{\text{SN}}(\rho) = 3 \text{ MeV}\left(\frac{\rho}{10^{11} \text{ g cm}^{-3}}\right)^{\frac{1}{3}}, \quad (15)$$

and adopt an electron fraction of $Y_e = 0.2$.

The emissivities themselves, as well as the difference between the emissivities, are strongly dependent on the density and temperature. The increase in the bremsstrahlung rates with increasing density is due to both the ρ^2 dependence and the roughly $T^{4.5}$ dependence of the number emission rate where the electron-positron annihilation number emission rates increase only to due to the increase in the temperature, scaling roughly as T^8. Therefore we expect the importance of bremsstrahlung over electron-positron pair annihilation to scale with the density. Indeed, when the density reaches the typical values of the PNS interior the nucleon-nucleon bremsstrahlung emission dominates. In practice, the core temperatures at densities larger then a few times 10^{13} g cm^{-3} do not reach the values predicted from Eq. (15), and therefore bremsstrahlung rates dominate over the electron-positron annihilation even more at the highest densities. For the electron-positron pair annihilation, the emissivity derived from
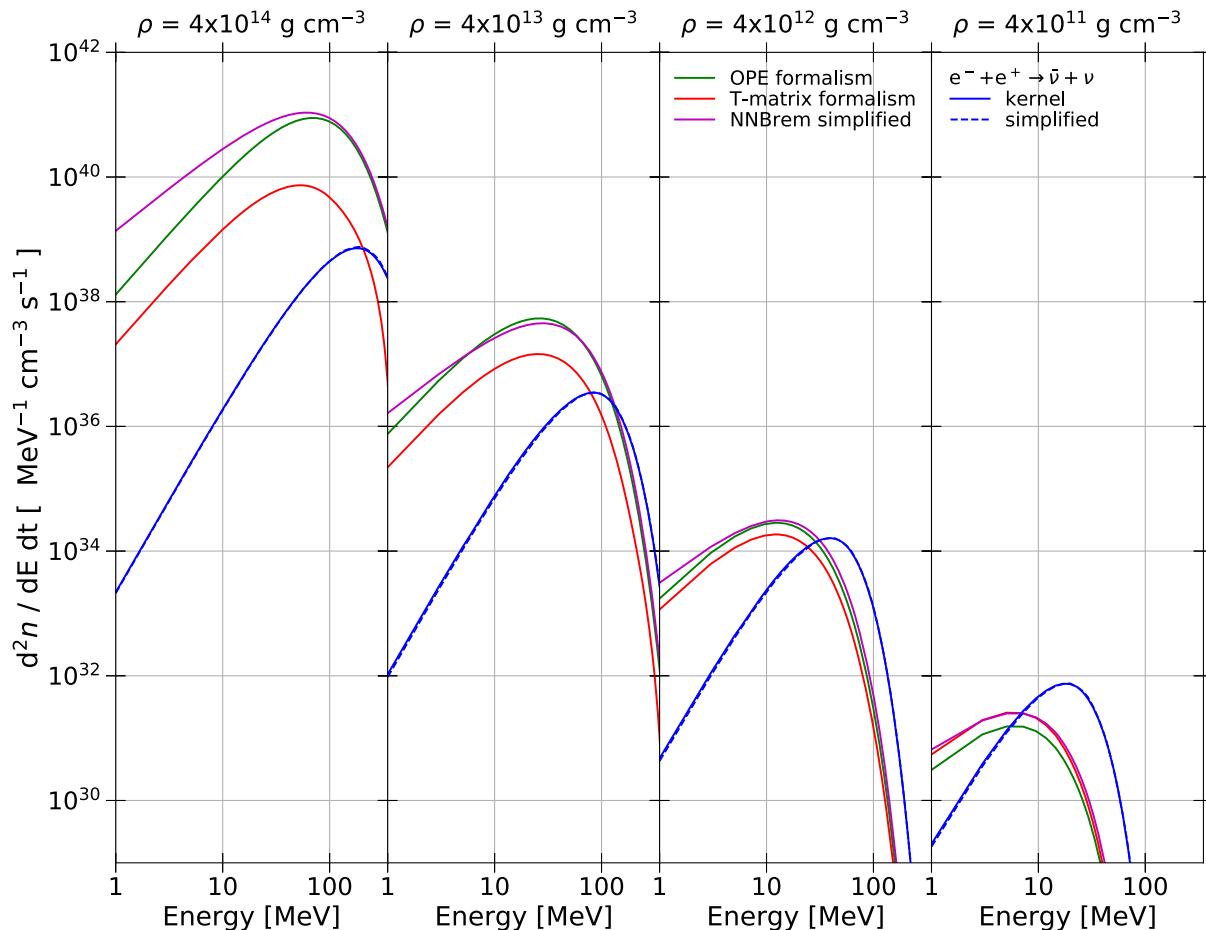
FIG. 1.   Number emissivities for the different pair-production processes for heavy-lepton neutrinos. For the bremsstrahlung we show the emissivity from the Hannestad and Raffelt (1998) [37] OPE potential kernel (green), the Guo *et al.* (2019) [38] T-matrix kernel (red), and the parametrization from Burrows *et al.* (2006) [39] (purple). For the electron-positron annihilation we show the emissivity based on the kernels (solid blue) and our parametrization of them (dashed blue), both from Bruenn (1985) [40]. We note that for the two electron-positron interactions we expect the same emissivities as the underlying interaction is the same.

the parametrization and the one from the kernel treatment are the same, as expected since the underlying interaction is the same.

We briefly comment on the differences between the bremsstrahlung treatments. The difference between the T-matrix and OPE treatment is very obvious for densities over 10^{14} g cm^{-3}. There, the prescriptions derived from the OPE potential give emissivities more than 10 times greater than the T-matrix prescription. This suppression of the rates at high densities, and also the more modest enhancement of the rates at low density when compared to the OPE interaction is a consequence of the T-matrix treatment [38,48,50]. The parametrization, which is based on the nondegenerate limit of the OPE generally produces comparable rates for the conditions used here. However, we note that the high temperature at nuclear densities resulting from Eq. (15) are higher then expected during the cooling phase and therefore under those conditions we would expect a larger deviation of the simplified rate from the OPE results. The rates that are expected to be important

during the CCSN evolution are the ones near and around the neutrinospheres where the neutrinos are decoupling from the matter. At high densities, the neutrinos are in equilibrium and the precise rate does not matter, and at low densities the rate is so low that it does not contribute appreciable to the overall neutrino emission. As pointed out in [49], the key densities are around $\rho \gtrsim 10^{12}$ g cm^{-3} during the early core-collapse phase and upward of $\rho \sim 10^{14}$ g cm^{-3} for the cooling phase. Over and above this, it is important to note that the many competing neutrino rates, and their strong temperature dependence, like electron-positron annihilation, often reduce the impact of changes in any one rate.

In addition to the differences that arise from the different interactions (in the case of bremsstrahlung), differences in the actual dynamical evolution can stem from the differences in the transport treatment. As discussed above in Sec. II A, for the simplified methods, the final state neutrino blocking is not taken in account properly for the emission, nor is the precise form of the annihilation

interaction used, rather simplified emission and absorption coefficients are used. With our systematic exploration of these interactions we aim to decipher these differences.

C. Setup

We performed a set of six simulations with two different progenitors for a total of 12 simulations. A $20M_\odot$, solar-metallicity, iron-core progenitor [51] and a $9.6M_\odot$ zero-metallicity iron-core progenitor [52] are used. We utilize the $20M_\odot$ progenitor as it is the same as the one studied in [6] where the evolution was computed using a variety of state-of-the-art evolution codes. The variation done in our study is on the transport treatment of the neutrino pair processes, the remaining physics is held constant. This is an interesting first step to gauge the influence of the different treatments and allows us to quantify the variations against the variations seen between different codes. For this progenitor, we used a grid containing 600 zones with the inner grid spacing being fixed at 300 m for the inner 20 km and increasing logarithmically outwards until $\sim 1.3 \times 10^{10}$ cm. This progenitor has been explored in many studies, but in particular, [53] also consider variations on the neutrino pair-production processes. The other progenitor we consider has a ZAMS mass of $9.6M_\odot$. Unlike most iron-core progenitors, this one has the peculiarity to explode in 1D. Although multidimensional effects can and do impact the development of the explosion in this model [54], these spherically symmetric simulations give us general insight on the behavior of the explosion energy development over time and on the neutrino-interaction dependence of the early cooling phase. For this progenitor, we used a spherically symmetric grid of 800 zones with a constant grid spacing of 300 m in the inner 20 km and then a logarithmically increasing zone size until $\sim 1.3 \times 10^9$ cm. This progenitor has been used in multidimensional studies [54–56]. For all of the simulations, we used the SFHo equation of state from Steiner *et al.* [57] with the same neutrino physics (other than the pair-production treatments) as [6]. The simulation time step is set by the radiation and is equal to the light crossing time of the smallest zone and a CFL condition of 0.4 before bounce, 0.1 near bounce and 0.5 from 20 ms after bounce for all the simulations. The reduction in the CFL condition near bounce is to ensure stability at the very dynamic time surrounding bounce when the shock first forms and the radiation quickly builds up for the first time. In our particular case, this is further necessitated by the first-order explicit treatment of the spatial flux calculation. We used a logarithmically spaced energy grid for the neutrinos from 1 MeV to 250 MeV with 18 energy groups.

III. RESULTS

In this section, we explore the impact of the different treatments of heavy-lepton neutrino pair-production

TABLE II. Enumeration of the different neutrino treatment combinations.

Model	Electron-positron Annihilation	Nucleon-Nucleon Bremsstrahlung
1	Simplified	Simplified
2	Simplified	OPE potential formalism
3	Simplified	T-matrix formalism
4	Kernel formalism	Simplified
5	Kernel formalism	OPE potential formalism
6	Kernel formalism	T-matrix formalism

described in Secs. II A and II B on the supernova evolution. For this, we apply the six different combinations of the pair processes treatments described in Table II. We will first explore the impact on the $20M_\odot$ progenitor evolution and follow with the exploding $9.6M_\odot$ progenitor evolution.

A. s20 progenitor

The $20M_\odot$ progenitor does not lead to an explosion. The shock radius evolutions are plotted in the top panel of Fig. 2. The different colors correspond to the different models in Table II. The blue, green, and red solid lines refer to the three simulations using the electron-positron anni-hilation kernels with the bremsstrahlung fit, OPE kernel, and T-matrix kernel, respectively, while the three dashed lines refer to the electron-positron annihilation simplified emissivity for the three different bremsstrahlung treatments. All of the models give qualitatively similar results. Bounce occurs at ~ 298 ms after the onset of collapse. The shock then expands for ~ 90 ms after bounce and reaches a radius of ~ 150 km where it stalls for ~ 10 ms and starts to recede. The shock radius shows a short expansion phase again at ~ 230 ms after bounce, which is due to the silicon-oxygen shell interface accreting through the shock front. The shock radius then continues to recede to attain ~ 50 km at 500 ms after bounce. For reference, we show with grey lines the shock radius evolution from simulations with various codes for the same progenitor and setup taken from the comparison study of [6]. The shock evolution of all our models generally agree with these simulations and the level of variation between our simulations is slightly less than that observed between the simulation codes.

The different neutrino-pair production treatments only modestly impact the shock radius evolution. For the simulations using the full kernel treatment for the electron-positron-annihilation to neutrino-pair process (models 4, 5, and 6) there is a consistently lower shock radius (~ 5 km) compared to the models with the simplified emissivity for this process (models 1, 2, and 3). This hierarchy is correlated with the properties of the heavy-lepton neutrino emission (bottom panels of Fig. 2). As we discuss below, during the first ~ 150 ms after bounce, the
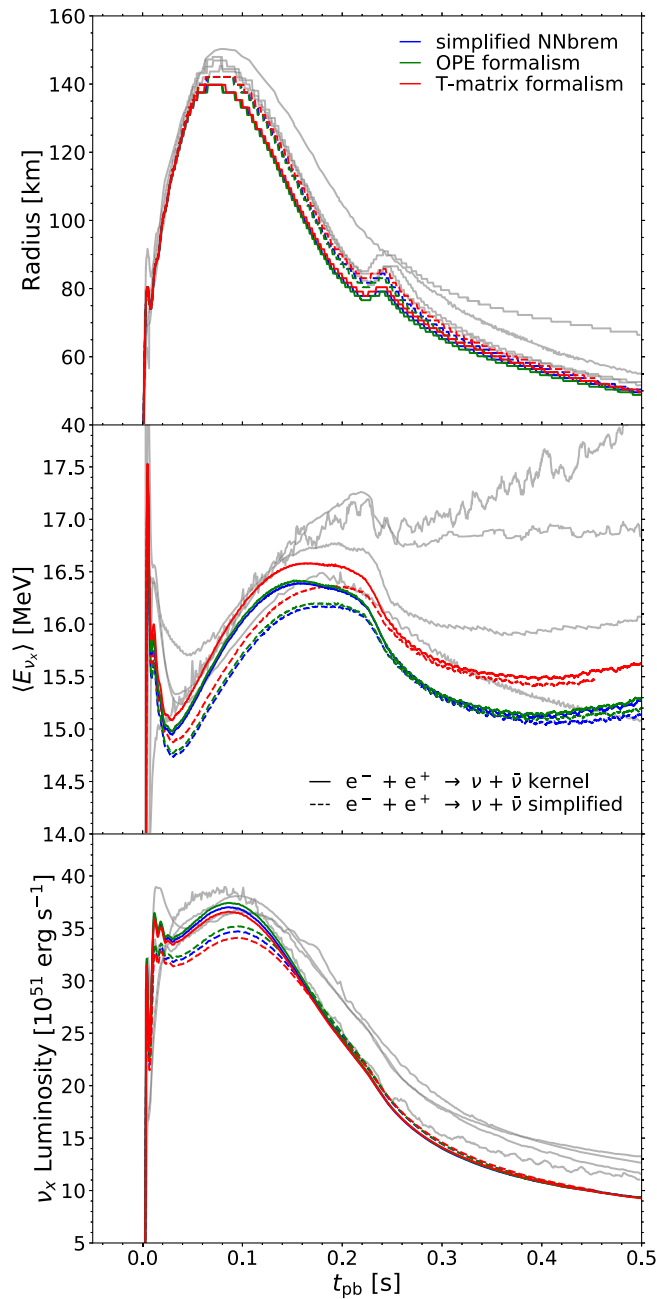
FIG. 2. Evolution quantities for the 6 models using the 20M$_\odot$ progenitor. In the top panel we show the shock radius evolution, the middle panel shows the ν_x mean energy, and the bottom panel shows the evolution of the ν_x luminosity.

largest heavy-lepton neutrino luminosities and mean energies arise from the simulations using the full kernel treatment of the electron-positron annihilation pair-production process. These simulations give enhanced cooling, smaller PNS radii, and smaller shock radii. This cause-and-effect is commonly seen in this model (and for which the explosion properties in multidimensional simulations of this model are particularly sensitive too), for example with modifications on the neutral-current scattering opacities [58,59].

In the bottom two panels of Fig. 2, we show the heavy-lepton neutrino mean energy (middle panel) and the heavy-lepton neutrino luminosity (bottom panel) as measured in the coordinate frame at 500 km. For the luminosities, after a small peak at bounce, there is a short rise to a plateau around $\sim 35 \times 10^{51}$ erg s^{-1} at the time of the peak shock radius. The heavy-lepton luminosities then decrease as the PNS contracts reaching values $\sim 10^{52}$ erg s^{-1} at 500 ms after bounce. For the heavy-lepton neutrino mean energies, after a short peak at bounce, the mean neutrino energy rises from ~ 30 ms after bounce from ~ 14.5–15 MeV to a peak of ~ 16–16.5 MeV. With the accretion of the silicon/oxygen interface the heavy-lepton neutrino mean energy drops ~ 1 MeV and generally plateaus at ~ 15–15.5 MeV until the end of the simulation at 500 ms. As we have shown for the shock radius, we show the neutrino luminosities and mean energies from [6] in grey. We can see that the different neutrino pair-production formalisms create differences which are comparable to the variability seen across different transport methods and hydrodynamics. It is worth noting that in [6], the prescriptions of the treatment of heavy-lepton neutrinos also varied among the codes.

During all stages of the evolution the quantities in Fig. 2 are within $\sim 10\%$ of each other for the luminosities and within $\sim 3\%$ for mean energies. However, the differences seen do correlate with the different pair-production treatments. Models 4, 5, and 6, where we use the full kernel-based treatment for the electron-positron annihilation process, have the largest neutrino luminosities and mean energies during the first ~ 150 ms after bounce, while the simplified electron-positron annihilation treatment (models 1, 2, and 3) shows consistently lower luminosities and energies during this time. As we mentioned above, this causes increased PNS contraction and lower shock radii for the former models. However, also as a consequence of the increased contraction, there is increased electron neutrino mean energies (see below), and an increased specific neutrino heating (although less overall heating due to the smaller gain region). For all models, the luminosity differences mostly disappear starting at ~ 200 ms after bounce, although some differences in the mean energy remain as we will discuss below.

For completeness, we show the impact of the different pair-production treatments on the electron-type neutrino luminosities and mean energies in Fig. 3, although the impact is small. For the ν_e luminosities, after the neutronization burst at bounce, the luminosities gradually increase and peak around ~ 120 ms after bounce at $\sim 72 \times 10^{51}$ erg s^{-1}. The $\bar{\nu}_e$ peak at the same time, but at a slightly higher value, $\sim 74 \times 10^{51}$ erg s^{-1}. The luminosities for both species then decrease due to the falling accretion rate, particularly at ~ 230 ms when the shell interface reaches the shock and the accretion rate drops dramatically. The differences created by the different pair-production treatments are of the order of $\sim 1\%$. We also
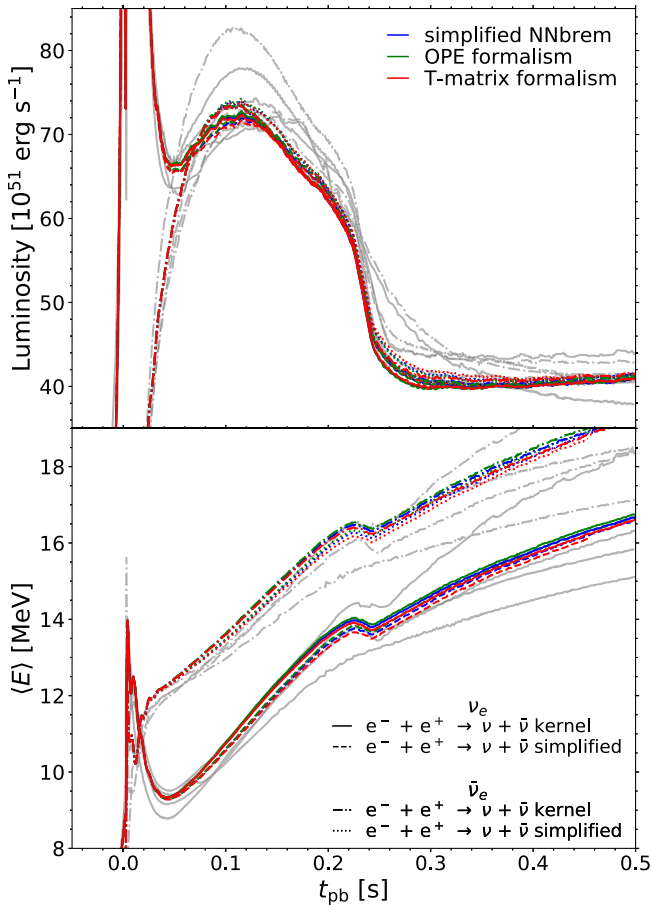
FIG. 3. Electron neutrino and antineutrino luminosities and mean energies evolutions for the 20-$M_\odot$ progenitor simulations. The color code is the same as previously used.

show, in the same way as for the ν_x quantities, the results from [6] in grey. Relative to the differences arising from different neutrino treatments and hydrodynamic schemes, the impact of the change in pair-production treatment on the emergent electron type neutrino properties is significantly less than we have seen for the heavy-lepton neutrinos. For the mean energies, after the peak at bounce, the mean energies continuously rise up to 19 MeV for the $\bar{\nu}_e$ and 16.5 MeV for the ν_e after 500 ms. The kink noticeable at ~230 ms is associated with the drop in the accretion rate from the accretion of the Si-O shell interface. Here, the variations between the models begin to show starting at ~70 ms after bounce and increase up to ~1% by the end of the simulated time, a similar level as the impact on the electron-type neutrino luminosities. As discussed above, the simplified electron-positron annihilation treatment for the heavy-lepton neutrinos under-predicts the PNS cooling and prevents contraction. Here we see the feedback of this on the electron neutrinos that, while very small, show slightly lower energies.

The impact of the nucleon-nucleon bremsstrahlung treatment on the evolution is less obvious. We do observe

that among the different bremsstrahlung treatment, the use of T-matrix formalism (models 3 and 6) systematically creates a higher neutrino mean energy throughout the entire simulation, but especially after ~250 ms after bounce. This is due to the lower emissivity of this interaction at higher densities (see Fig. 1) which gives an earlier decoupling radius and therefore a harder spectrum, since the matter temperatures are higher. The luminosities also tend to be the lower soon after bounce when using this formalism. The differences between the use of the OPE potential kernel-based formalism and the simplified emissivity based on this same potential only appear in the luminosities, and even there it is minimal. It has the effect of reducing the luminosity for ~160 ms following bounce, analogous to the use of the simplified emissivity for the electron-positron annihilation, but smaller in magnitude.

From these observations we conclude that the differences created by the use of the simplified emissivities mainly lie in simplistic treatment of the neutrino transport (i.e., ignoring the functional form of the neutrino and antineutrino distributions and their angular dependence as well as any final state blocking, as explained in Sec. II A) rather than differences in the underlying neutrino interaction model. A previous study, [53], explored the impact of a simplified heavy-lepton neutrino pair-production treatments as well. They find similar changes on the luminosity, mean energy and shock radius evolution as the ones we find comparing models 1 and 5. They suggest that the differences seen are a result of the implicit assumption of the angular dependence (i.e., that it is isotropic) of the neutrino annihilation partner, rather than the *in situ* distribution, which is forward peaked (we note we from Eq. (12) that the annihilation strength is minimal for cotraveling neutrinos). This overpredicts neutrino-antineutrino annihilations within the simplified emissivity assumption. While this is certainly true, we note that since the neutrino annihilations are occurring well below the scattering surface, the distribution function is very isotropic. We therefore suggest it is rather the overall magnitude of the occupation density of the annihilation partner (which is implicitly assumed to be the black body distribution) that causes the simplified emissivity to over-predict annihilation and thus lead to smaller emergent heavy-lepton neutrino luminosities. We show this in the following using Fig. 4.

For the 20$M_\odot$ progenitor at both 90 ms (left) and 350 ms (right), we show several key heavy-lepton neutrino properties from both model 3 (simplified electron-positron treatment; dashed line) and model 6 (kernel electron-positron treatment; solid line). In red, we show the growing outward going heavy-lepton neutrino luminosity, i.e., $4\pi r^2 F_r$, normalized so that the luminosity from the full kernel treatment is 100% at 500 km. In blue, again for model 3 and 6 with dashed and solid line, respectively, we show the difference between the equilibrium heavy-lepton neutrino distribution and the actual heavy-lepton neutrino
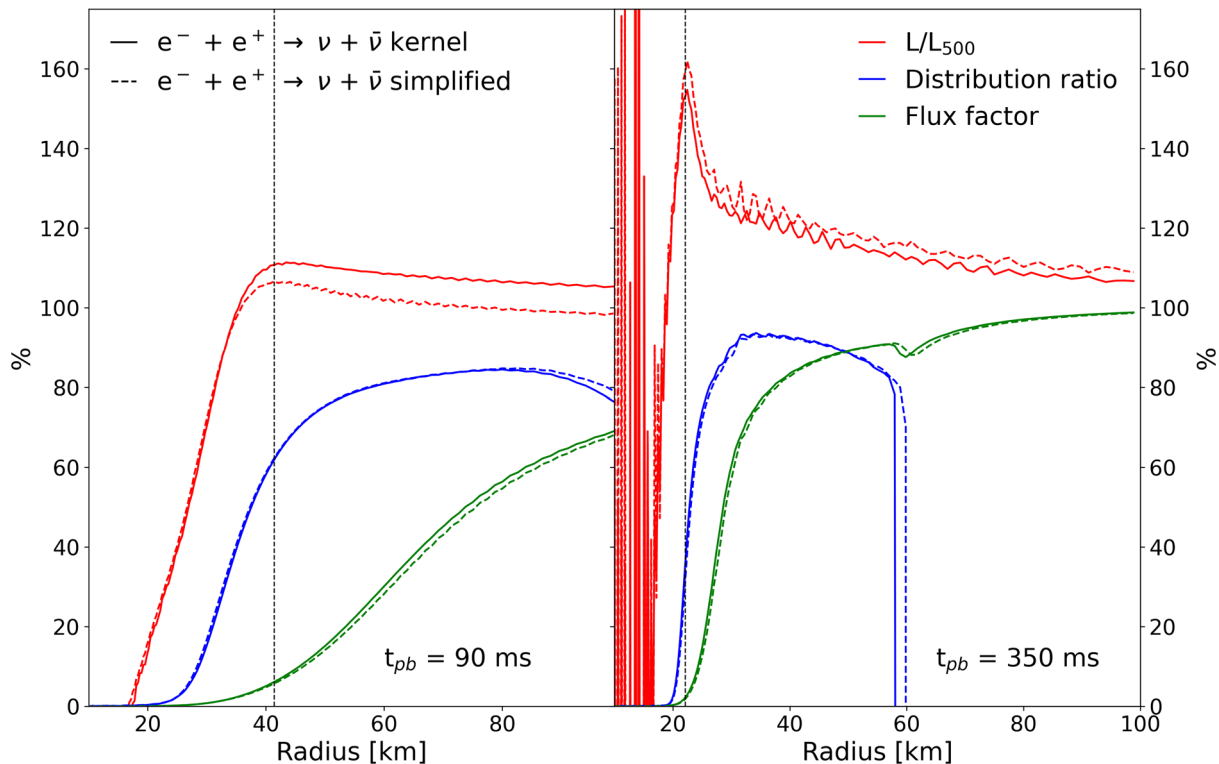
FIG. 4.   Radial neutrino properties at early (left) and late (right) times for the $20M_\odot$ progenitor. We show results for the kernel treatment of electron-positron annihilation with solid lines and the simplified electron-positron annihilation treatment with dashed lines. In both cases, we use the T-matrix kernel treatment for the bremsstrahlung interaction. In red we show the radial evolution of the total outgoing neutrino luminosity, normalized to the value to the kernel treatment at 500 km. In blue we show the relative difference between the actual and equilibrium neutrino distribution function, while in green we show the flux factor. For the former radial profile we select an energy bin with ~15 MeV. Vertical lines denote the peak of the neutrino luminosity for the simplified treatment.

distribution relative to the heavy-lepton equilibrium distribution, i.e., $(f_{eq} - f)/f_{eq} = 1 - f/f_{eq}$ for an energy bin corresponding to ~15 MeV. Here we take $f = J/(4\pi\nu^3)$ and $f_{eq} = 1/(\exp(\nu/T) + 1)$. In green, we show the energy averaged heavy-lepton flux factor ($= F_r/E$). This allows us to highlight the proportional importance of the anisotropy of the neutrino field (the green lines) and the deviation of the actual neutrino distribution from equilibrium (blue lines). At the early time (left panel), at the radii where the neutrinos luminosity is rising (~20 − 40 km) the distributions are almost isotropic ($F_r/E \sim 15\%$). However at these same radii, the occupation density of the neutrinos significantly deviates from the black body, falling short of the equilibrium occupation density by ~60% at ~40 km. Since the simplified treatment implicitly assume a black body distribution for the annihilation partners, this leads to an over prediction of the annihilation rate in this regime. The result is a further out decoupling radius, and ultimately a lower heavy-lepton neutrino luminosity and mean energy. This implies that a significant factor in the difference between a full and simplified treatment is linked to the assumed distribution of the pair neutrino rather than the intrinsic anisotropy of the radiation field.

For late times (right panel), at the radii where the luminosity is rising (~16 − 22 km), the distribution is almost completely isotropic (rising to $F_r/E \sim 5\%$ at 22 km) and the deviation of the distribution function from the equilibrium distribution is negligible at all radii except for the last 20% of the emission, even there, the deviation is at most ~30%. As a result we do not see any excess annihilation at these late times. It is worth noting that the simplified treatment does actually predict a larger luminosity at these late times, by a few percent. We suspect this is due to lack of final state blocking in the emission of the neutrinos within the simplified treatment. At late times the value of the heavy-lepton neutrino distribution function near the peak of the emission is several times the value seen at earlier times, raising the impact of the final state blocking. Some oscillations appear in the luminosity for late times. This is a consequence of the explicit-in-time, first-order, forward-Euler scheme used for the evaluation of the spatial fluxes. It tends to occur for energy groups that are close to free streaming (with the characteristic speeds entering the Riemann problem approaching c) in zones with a CFL condition $c\Delta t/\Delta x \sim 0.5$. It causes the small oscillations seen near ~30 km and the instabilities in the

outward going neutrino flux under 15 km, which at this point is constrained to the lowest energy groups as the rest are fully trapped.

B. z9.6 progenitor

In order to show the impact of the different heavy-lepton pair process neutrino treatments on an exploding model, we evolved one of the few progenitors known to explode in 1D [54,56], a $9.6M_\odot$, zero-metallicity star evolved with the KEPLER stellar evolution code [52]. We simulate, using GR1D, the six combinations of thermal-interaction models listed in Table II. All models successfully explode. For all models, the shock expansion does not stall as in traditional iron-core collapse progenitors like it does in Fig. 2 for the $20M_\odot$ progenitor. The shock radius evolution can be seen in the top panel of Fig. 5. Here we plot the location of the maximum velocity gradient which flags accurately the position of the, sometimes multiple, different shocks. The explosion times vary across the models, showing the sensitivity of the explosion to these neutrino inter-actions. The earliest explosion time, here arbitrarily defined as when the shock passes 1000 km for the last time, is ∼310 ms after bounce while the latest explosion is ∼470 ms after bounce, ∼50% longer. It is also notable
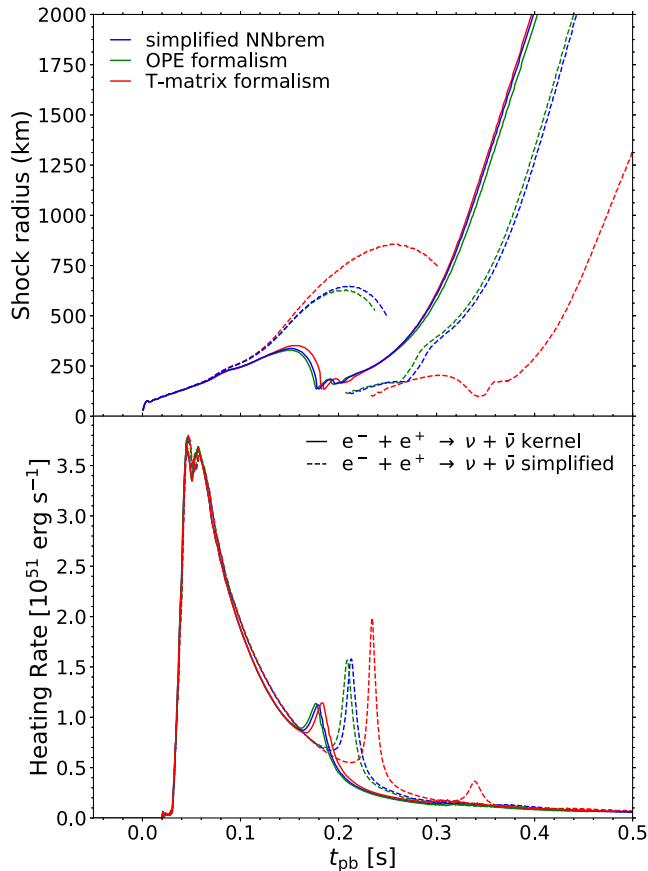

FIG. 5. The evolution of the shock radius (top panel) and neutrino heating (bottom panel) for the $9.6M_\odot$ progenitor vs time.

that the initial shock formed at bounce is not the one that ultimately leads to the final explosion. In all cases, the first shock expands but is not energetic enough to runaway. The accretion of this material onto the PNS creates a burst of neutrino heating (bottom panel of Fig. 5) and a secondary shock which will ultimately lead to an explosion. The formation time of this second shock corresponds to the heating peaks in the lower panel as the in-falling matter is compressed and the neutrino heating in the gain region increases enough to initiate the explosion. In general, the models using the simplified treatment for electron-positron annihilation show a strong initial shock expansion phase, but a later ultimate explosion time, while the models with the full kernel treatment of electron-positron annihilation show a lower initial shock expansion and an earlier explosion. While the appearance of the secondary shock could be thought as being linked to neutrino winds [60,61], the secondary is indeed a shock in its jump in density, entropy and velocity. Moreover, we search for the trigger of neutrino winds by using the local adiabatic sound speed and comparing it to the fluid velocity. While neutrino-driven winds indeed appear, this happens at the end of our simulation when the secondary (or tertiary) shock has already undergone a runaway expansion. As our simulation time postexplosion is relatively short, we do not extensively explore the neutrino winds and the impact of the neutrino treatments on them. We discuss the difference seen between the different interaction models in more detail below.

In Fig. 6, we show the heavy-lepton neutrino quantities for this progenitor model. In the top and bottom panel we show the mean energy and luminosity, respectively for each of the six neutrino pair-production treatments shown in Table II. After a sharp and short peak at bounce, the mean energies plateau for the first ∼100 ms after bounce around 15 MeV with a spread ∼0.5 MeV. The mean energies decrease over the remaining 400 ms of the simulations by ∼1–1.5 MeV, depending on the treatment used, with the T-matrix treatment maintaining the highest mean energy, as was the case in the $20M_\odot$ progenitor above. As for the $20M_\odot$, the impact on the $\nu_e/\bar\nu_e$ average energies is almost negligible. The luminosities present a peak just after bounce and then slowly decrease until the end of the simulation. The heavy-lepton neutrino luminosities and energies present a similar dependence on the explored interactions as observed for the $20M_\odot$ progenitor with the models using the full kernel treatment of the electron-positron pair annihilation having higher luminosities soon after bounce and then reaching similar, but slightly lower, values to the simplified formalism at later times. As for the case of the $20M_\odot$ progenitor, we attribute these differences to the treatment of the transport in the simplified models. Particularly, the differences at early times are attributed to the form of the effective absorption coefficient which incorrectly treats the distribution of the annihilation partner and the smaller difference at late times due to the
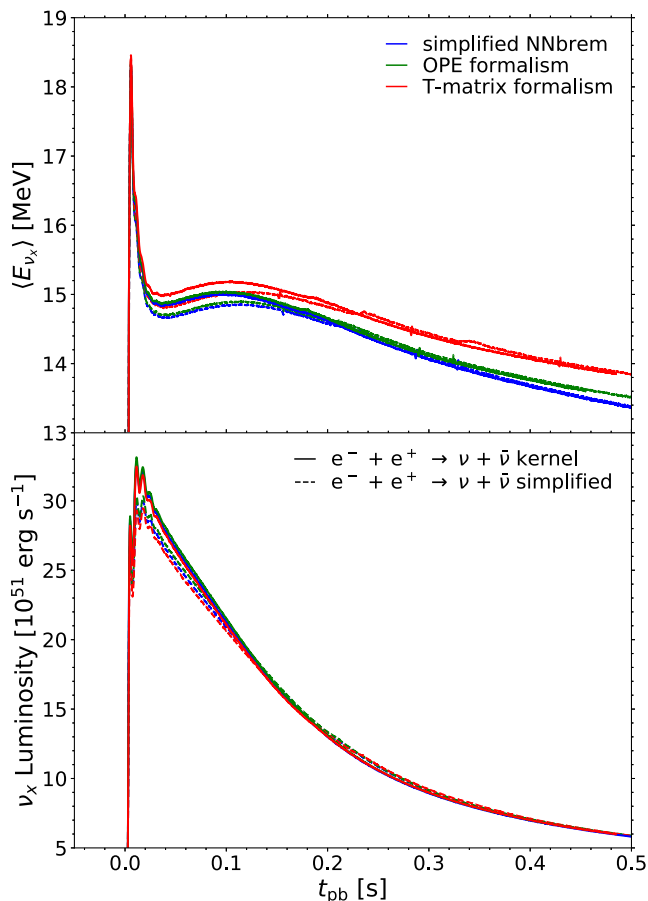
FIG. 6. Heavy-lepton neutrino quantities for the six models of the 9.6M$_\odot$ progenitor with varying neutrino interactions. We show the mean energy and luminosity evolution in the top and bottom panels, respectively.

assumption of no final state blocking for the neutrinos during the emission process. At late times, the largest difference in the neutrino quantities arises from the use of the T-matrix bremsstrahlung kernels where the lower opacity at higher densities gives rise to higher neutrino energies, by ~3%, this is seen in both the simplified and the full kernel treatment. In the same way as for the 20M$_\odot$ progenitor, the $\nu_e/\bar{\nu}_e$ luminosities show a small if not negligible impact from the different treatments.

We conclude our discussion of the 9.6M$_\odot$ progenitor by examining the impact of the different neutrino interaction models in Table II on the development of the explosion and the shock propagation. The largest systematic difference we observe between the models using different interactions is the shock evolution for the three simulations that use the simplified treatment of electron-positron annihilation to neutrino pairs versus the three models that use the kernel-based treatment. This is seen in Fig. 5, but we show further evidence for this in Fig. 7. In the six panels of Fig. 7, we show the accretion history for each simulation. Blue colors denote negative mass flow (accreting material) while red colors show positive mass flow (expanding material).

The three models for which we use the simplified treatment of electron-positron annihilation (models 1, 2, 3) are shown on the top row while the three models using the full kernel treatment (models 4, 5, 6) are shown on the bottom row. The left, middle, and right columns include the simplified bremsstrahlung treatment, the OPE kernel treatment, and the T-matrix kernel treatment, respectively. The three models with the simplified electron-positron annihilation pair production treatment have a slightly faster initial shock expansion from higher neutrino heating (see Fig. 5), with the T-matrix bremsstrahlung treatment having the largest such expansion. This causes these three models to undergo a strong initial shock acceleration phase starting around ~130 ms after bounce. Although, except for a small region directly behind the shock during this expansion phase, matter is mainly accreting in the postshock region. These shocks eventually fail. It is worth noting that in multidimensional simulations of this progenitor [54,56] the explosions typically set in during this period as the added role that multidimensional effects like convection and turbulence play is enough to initiate the explosion. However, in our spherically symmetric simulations this is not the case. Eventually, secondary shocks form at the surface of the PNS between ~200 − 240 ms after bounce concomitant with the increased accretion rate from the failing shock (see the dark blue regions around ~100 − 150 km at this time) which eventually give the ultimate explosion and the beginnings of a neutrino driven wind. The three models with the full kernel treatment for electron-positron annihilation do not undergo this accelerated expansion and continue to mildly expand until ~160 ms at which point the shock fails and the secondary shock forms at ~180 ms after bounce. These models are the first to ultimately explode.

We compute the diagnostic explosion energy for each of the six models simulated,

$$E_{\mathrm{dia}} = \int_{v>0} \left[\phi + \frac{v^2}{2} + (\epsilon - \epsilon_0) \right]_{>0} dm, \qquad (16)$$

where ϕ is the gravitational potential, v is the fluid velocity, ϵ is the specific internal energy, and ϵ_0 is a reference zero-point taken for simplicity to be the value of the internal energy of the EOS for the same density and Y_e but for $T = 0$. We only consider contributions to the diagnostic energy from outflowing matter and where the integrand of Eq. (16) is positive, this is a proxy for unbound material. The results are shown Fig. 8. In general, for the 9.6M$_\odot$ progenitor the explosion energy depends on the time of the explosion. For early explosions in multiple dimensions, for example see [54,56], the explosion energies can reach several to 10 times 10^{49} erg. In our relatively late spherically symmetric explosions, we see explosion energies ~10^{49} erg for the five models that explode first. The last model to explode achieves only 0.4 × 10^{49} erg owing to the
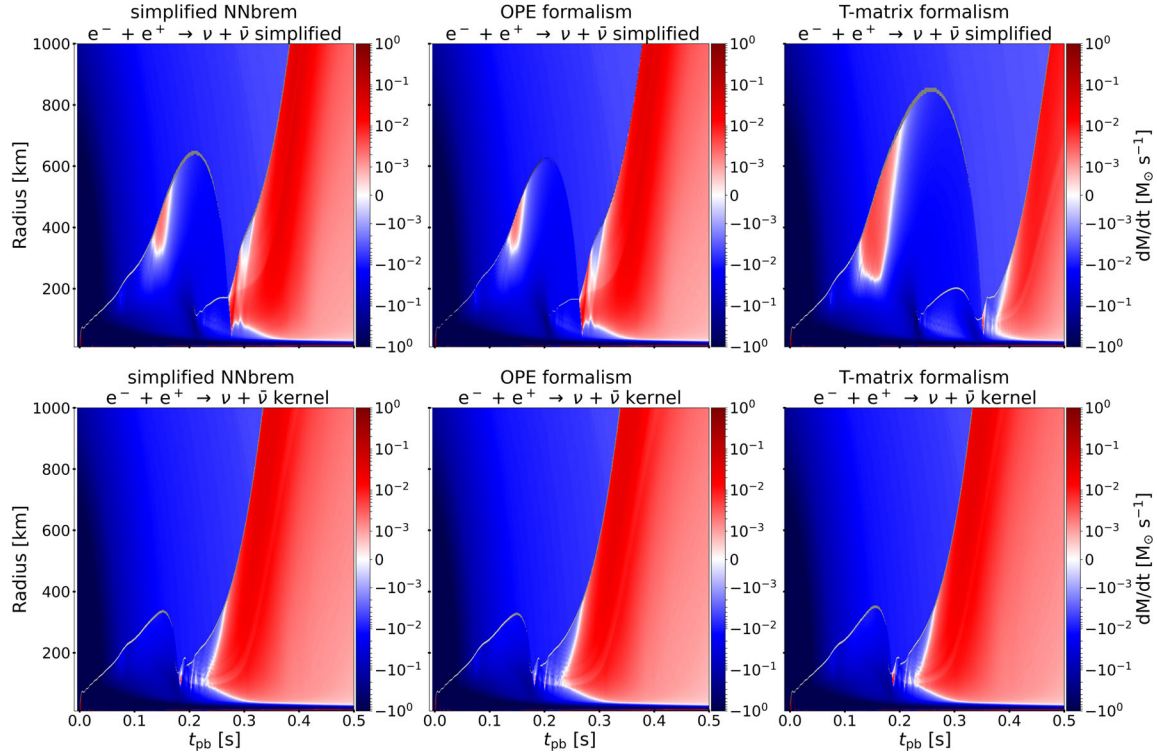
FIG. 7.   Mass flow for the six different interaction sets explored vs time. Blue colors denote accreting material, red denotes expanding material. Overlaid in grey are the location of the (sometimes multiple) shock fronts.
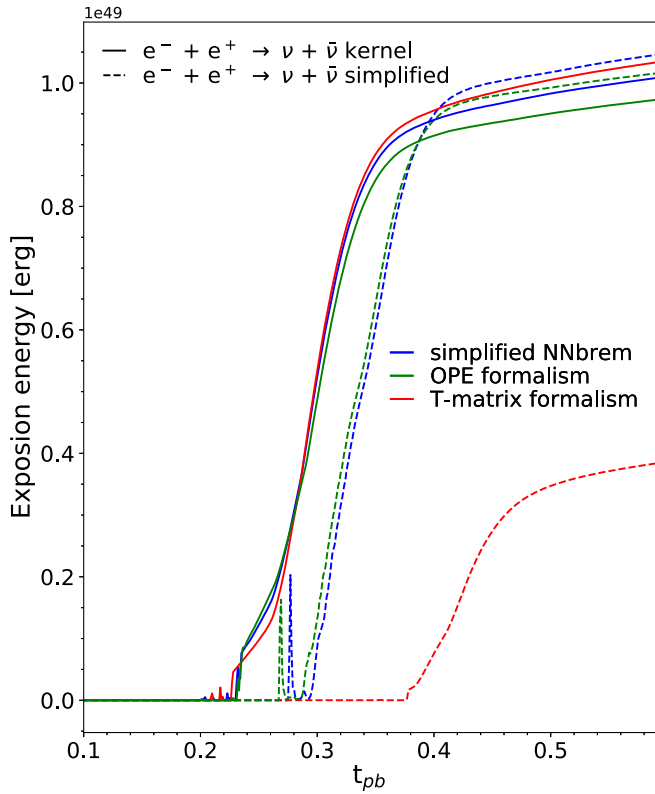

FIG. 8.   Diagnostic explosion energy for the $M_\odot$ progenitor model for each of the neutrino interaction sets explored. Early explosions generally give higher diagnostic explosion energies.

much lower neutrino heating rates present at the later times. We see that while the rise of the explosion energy is strongly correlated with the onset of the explosion, the ultimate explosion energy is not strictly dependent on the explosion time. We see that differences can arise due to the complex interplay of the neutrino heating of the fallback material from the initial failed shock (see Fig. 7).

Finally, we note that $\epsilon - \epsilon_0$ in Eq. (16) is an estimate of the sum of the thermal energies and the recombination energy that will be converted to thermal energy as the matter recombines. We tested this against an explicit calculation similar to that of [54]. If we assume that all the free nucleons and alpha particles present in the matter would recombine to iron this sets the specific recombination energy. We use this, along with the specific internal energy from the Helmholtz EOS [62] at a matter temperature of T to replace $\epsilon - \epsilon_0$ in Eq. (16). We find comparable, to within 5%, diagnostic explosion energies as shown in Fig. 8.

IV. CONCLUSION

In this paper, we highlighted and explored the importance of heavy-lepton (ν_μ, ν_τ, and their antiparticles) neutrinos and the interactions that produce them in the scope of spherically-symmetry, fully general-relativistic neutrino-driven CCSNe simulations. We performed systematic simulations on two different progenitors, a solar metallicity progenitor star with a ZAMS mass of $20M_\odot$

which has been extensively used in the literature for CCSN simulations, including a recent comparison study and a zero metallicity progenitor star with a ZAMS mass of $9.6M_\odot$ that has the peculiarity to explode even in spherically symmetric simulations. We simulate the core collapse and the early post-bounce phase using the open-source software GR1D and Nulib, which we update accordingly with the work presented in this paper. In particular, we test the importance of the two main heavy-lepton neutrino pair-production processes in CCSNe, electron-positron annihilation to a neutrino-antineutrino pair and nucleon-nucleon scattering that radiates a neutrino-antineutrino pair (i.e., nucleon-nucleon bremsstrahlung). We explore two main effects. First, we study the neutrino transport implementation of both of these interactions by utilizing a simplified approached with effective emission and absorption coefficients and a complete treatment utilizing complete scattering kernels and *in situ* neutrino distribution functions. The aim for this part of the study is to assess the impact and quantify systematic effects of the simplified treatment on CCSN simulations with the goal of providing a robust prescription for use in multidimensional simulations. Second, we explored two independent nuclear-physics based prescriptions for the nucleon-nucleon bremsstrahlung interaction (in addition to a simplified approach as mentioned above). One of these interactions is commonly used throughout the literature for CCSNe simulations and is based on the one-pion exchange formalism [37]. The other interaction [38], formulates the nucleon-nucleon bremsstrahlung scattering kernel based on a T-matrix formalism where the underlying interaction is constrained by experimental phase shifts, see also [48]. From these variations we arrive at six combinations of interactions to explore with our CCSN simulations.

We find that overall the simplified neutrino interactions do a fair job at reproducing the neutrino quantities (within ∼10%) and the dynamics of the core collapse event, although potentially important differences are present that need to be considered when employing the simplified treatment for precision simulations. We find the simplified method under predicts the heavy-lepton neutrino luminosity in the early stages, by ∼10%. We show that this is the result of the simplistic treatment of the distribution of the annihilation partner, i.e., the assumption that it follows the blackbody distribution. This leads to an overestimate of the annihilation rate as the neutrinos begin to free stream away from the CCSN core. In the region where this excess annihilation is occurring the distribution function is quite isotropic and therefore, as opposed to that suggested in previous works, this difference is unlikely due to the

assumption of isotropy in the simplified treatment. While the largest impact is seen with different treatments for the electron-positron annihilation interaction, we see the same (but much smaller in impact) trend with the simplified treatment of nucleon-nucleon bremsstrahlung. At later times the simplified treatment agrees much better with the full kernel treatment, owing to the fact that the distribution of the annihilation partner is much closer to the blackbody distribution in the regions where the neutrinos are decoupling. We do see a slight overestimate of the luminosity for the simplified treatment, which we attribute to the assumption of no final-state neutrino blocking in the simplified emission treatment. Finally, we comment on the impact of using a different microphysical interaction for the nucleon-nucleon bremsstrahlung. The use of the T-matrix formalism over the standard one-pion exchange treatment systematically increases the heavy-lepton neutrino energy by ∼5% which we infer is due to the reduced interaction strength of the T-matrix kernel at larger densities compared the one-pion exchange kernel. This causes the heavy-lepton neutrinos to begin to decouple deeper into the PNS core, where the temperature is higher.

For cases where the dynamics can sensitively depend on the neutrino physics, for example with the $9.6M_\odot$ progenitor studied here, we find that the different interactions explored can impact the heating enough at the earlier stages to quantitatively effect the development of the explosion, including the ultimate explosion time and the explosion energy. To what extent this carries over to multidimensional simulations remains to be seen, although it is important to note that even in multidimensional simulations we know there is sensitivity to the neutrino physics at the ∼10% level demonstrated here [58,59].

[1] S. Woosley, A. Heger, and T. A. Weaver, Rev. Mod. Phys. **74**, 1015 (2002).

[2] F.-K. Thielemann, M. Eichler, I. V. Panov, and B. Wehmeyer, Annu. Rev. Nucl. Part. Sci. **67**, 253 (2017).

[3] R. J. Bruch *et al.*, arXiv:2008.09986.

[4] H.-T. Janka, in *Handbook of Supernovae*, edited by A. W. Alsabti and P. Murdin (Springer International Publishing, Cham, 2017), pp. 1575–1604.

[5] K. Kotake and T. Kuroda, in *Handbook of Supernovae*, edited by A. W. Alsabti and P. Murdin (Springer International Publishing, Cham, 2017), pp. 1671–1698.

[6] E. O'Connor, R. Bollig, A. Burrows, S. Couch, T. Fischer, H.-T. Janka, K. Kotake, E. J. Lentz, M. Liebendrfer, O. E. B. Messer, A. Mezzacappa, T. Takiwaki, and D. Vartanyan, J. Phys. G **45**, 104001 (2018).

[7] P. Msta, S. Richers, C. D. Ott, R. Haas, A. L. Piro, K. Boydstun, E. Abdikamalov, C. Reisswig, and E. Schnetter, Astrophys. J. **785**, L29 (2014).

[8] R. Glas, H.-T. Janka, F. Capozzi, M. Sen, B. Dasgupta, A. Mirizzi, and G. Sigl, Phys. Rev. D **101**, 063001 (2020).

[9] A. Burrows, D. Radice, and D. Vartanyan, Mon. Not. R. Astron. Soc. **485**, 3153 (2019).

[10] D. Vartanyan, A. Burrows, D. Radice, M. A. Skinner, and J. Dolence, Mon. Not. R. Astron. Soc. **477**, 3091 (2018).

[11] K.-C. Pan, C. Mattes, E. P. O'Connor, S. M. Couch, A. Perego, and A. Arcones, J. Phys. G **46**, 014001 (2019).

[12] H.-T. Janka, in *Handbook of Supernovae*, edited by A. W. Alsabti and P. Murdin (Springer International Publishing, Cham, 2017), pp. 1095–1150.

[13] H. A. Bethe and J. R. Wilson, Astrophys. J. **295**, 14 (1985).

[14] H. A. Bethe, Rev. Mod. Phys. **62**, 801 (1990).

[15] H.-T. Janka, F. Hanke, L. Huedepohl, A. Marek, B. Mueller, and M. Obergaulinger, Prog. Theor. Exp. Phys. **2012**, 01A309 (2012).

[16] A. Burrows, Rev. Mod. Phys. **85**, 245 (2013).

[17] T. Foglizzo, R. Kazeroni, J. Guilet, F. Masset, M. Gonzlez, B. K. Krueger, J. Novak, M. Oertel, J. Margueron, J. Faure, N. Martin, P. Blottiau, B. Peres, and G. Durand, Pub. Astron. Soc. Aust. **32**, e009 (2015).

[18] D. Vartanyan, A. Burrows, D. Radice, A. Skinner, and J. Dolence, Mon. Not. R. Astron. Soc. **482**, 351 (2019).

[19] D. Vartanyan, A. Burrows, and D. Radice, Mon. Not. R. Astron. Soc. **489**, 2227 (2019).

[20] H. Nagakura, A. Burrows, D. Radice, and D. Vartanyan, Mon. Not. R. Astron. Soc. **490**, 4622 (2019).

[21] J. W. Murphy, Q. Mabanta, and J. C. Dolence, Mon. Not. R. Astron. Soc. **489**, 641 (2019).

[22] B. Mller, Pub. Astron. Soc. Aust. **33**, e048 (2016).

[23] B. Mller, D. Gay, A. Heger, T. Tauris, and S. A. Sim, Mon. Not. R. Astron. Soc. **479**, 3675 (2018).

[24] B. Mller, T. M. Tauris, A. Heger, P. Banerjee, Y.-Z. Qian, J. Powell, C. Chan, D. W. Gay, and N. Langer, Mon. Not. R. Astron. Soc. **484**, 3307 (2019).

[25] R. Glas, O. Just, H.-T. Janka, and M. Obergaulinger, Astrophys. J. **873**, 45 (2019).

[26] D. Radice, V. Morozova, A. Burrows, D. Vartanyan, and H. Nagakura, Astrophys. J. Lett. **876**, L9 (2019).

[27] J. Powell and B. Mller, Mon. Not. R. Astron. Soc. **487**, 1178 (2019).

[28] E. O'Connor and S. Couch, Astrophys. J. **865**, 81 (2018).

[29] R. M. Cabezn, K.-C. Pan, M. Liebendrfer, T. Kuroda, K. Ebinger, O. Heinimann, F.-K. Thielemann, and A. Perego, Astron. Astrophys. **619**, A118 (2018).

[30] H. Nagakura, K. Sumiyoshi, and S. Yamada, Astrophys. J. **878**, 160 (2019).

[31] K. S. Thorne, Mon. Not. R. Astron. Soc. **194**, 439 (1981).

[32] M. Shibata, K. Kiuchi, Y.-I. Sekiguchi, and Y. Suwa, Prog. Theor. Phys. **125**, 1255 (2011).

[33] R. Bollig, H.-T. Janka, A. Lohs, G. Martinez-Pinedo, C. Horowitz, and T. Melson, Phys. Rev. Lett. **119**, 242702 (2017).

[34] G. Guo, G. Martinez-Pinedo, A. Lohs, and T. Fischer, Phys. Rev. D **102**, 023037 (2020).

[35] T. Fischer, S. Typel, G. Rpke, N.-U. F. Bastian, and G. Martinez-Pinedo, arXiv:2008.13608 [Phys. Rev. C (to be published)].

[36] E. O'Connor, Astrophys. J. Suppl. Ser. **219**, 24 (2015).

[37] S. Hannestad and G. Raffelt, Astrophys. J. **507**, 339 (1998).

[38] G. Guo and G. Martinez-Pinedo, Astrophys. J. **887**, 58 (2019).

[39] A. Burrows, S. Reddy, and T. A. Thompson, Nucl. Phys. **A777**, 356 (2006).

[40] S. W. Bruenn, Astrophys. J. Suppl. Ser. **58**, 771 (1985).

[41] E. O'Connor and C. D. Ott, Classical Quantum Gravity **27**, 114103 (2010).

[42] C. Y. Cardall, E. Endeve, and A. Mezzacappa, Phys. Rev. D **87**, 103004 (2013).

[43] G. N. Minerbo, J. Quant. Spectrosc. Radiat. Transfer **20**, 541 (1978).

[44] C. J. Horowitz, Phys. Rev. D **65**, 043001 (2002).

[45] C. J. Horowitz, Phys. Rev. D **55**, 4577 (1997).

[46] T. A. Thompson, A. Burrows, and J. E. Horvath, Phys. Rev. C **62**, 035802 (2000).

[47] D. R. Entem, R. Machleidt, and Y. Nosyk, Phys. Rev. C **96**, 024004 (2017).

[48] A. Bartl, C. J. Pethick, and A. Schwenk, Phys. Rev. Lett. **113**, 081101 (2014).

[49] A. Bartl, R. Bollig, H.-T. Janka, and A. Schwenk, Phys. Rev. D **94**, 083009 (2016).

[50] T. Fischer, Astron. Astrophys. **593**, A103 (2016).

[51] S. E. Woosley and A. Heger, Phys. Rep. **442**, 269 (2007).

[52] A. Heger (private communication).

[53] O. Just, R. Bollig, H.-T. Janka, M. Obergaulinger, R. Glas, and S. Nagataki, Mon. Not. R. Astron. Soc. **481**, 4786 (2018).

[54] T. Melson, H.-T. Janka, and A. Marek, Astrophys. J. **801**, L24 (2015).

[55] B. Mueller, H.-T. Janka, and A. Marek, Astrophys. J. **766**, 43 (2013).

[56] D. Radice, A. Burrows, D. Vartanyan, M. A. Skinner, and J. C. Dolence, Astrophys. J. **850**, 43 (2017).

[57] A. W. Steiner, M. Hempel, and T. Fischer, Astrophys. J. **774,** 17 (2013).

[58] T. Melson, H.-T. Janka, R. Bollig, F. Hanke, A. Marek, and B. Mller, Astrophys. J. Lett. **808,** L42 (2015).

[59] E. O'Connor, in *Handbook of Supernovae*, edited by A. W. Alsabti and P. Murdin (Springer International Publishing, Cham, 2017), pp. 1555–1572.

[60] A. Arcones, H.-T. Janka, and L. Scheck, Astron. Astrophys. **467,** 1227 (2007).

[61] T. A. Thompson, A. Burrows, and B. S. Meyer, Astrophys. J. **562,** 887 (2001).

[62] F. X. Timmes and F. D. Swesty, Astrophys. J. Suppl. Ser. **126,** 501 (2000).